Changes in marine-terminating outlet glaciers in northwestern Greenland from remote sensing

リモートセンシングを用いた

グリーンランド北西部における溢流氷河の変動に関する研究

Yefan Wang

Ph.D. Dissertation

Division of Earth System Science

Graduate School of Environmental Science

Hokkaido University

July 2022

ABSTRACT

Mass loss from the Greenland ice sheet has accelerated over the past two decades. This change is due to melt increase in the ablation area and accelerated ice discharge from marine-terminating outlet glaciers, which are linked to the warming climate. Understanding the glacier changes under the rapidly changing Arctic climate is crucial for constraining the contribution of the Greenland ice sheet to sea-level rise. To study glacier changes over a broad area on a decadal scale, satellite remote sensing is a suitable and commonly employed approach. The goal of this study is to use multi-source remote sensing datasets to improve our knowledge of glacier changes in the Prudhoe Land region in northwestern Greenland over the last four decades. To achieve these goals, I therefore monitored elevation changes and supraglacial lake changes in this study.

I use digital elevation models derived from satellite images and aerial photographs to quantify the mass loss of 16 outlet glaciers in the study area from surface elevation change from 1985 to 2018. The mean rate of the surface elevation change over the studied glaciers was -0.55 ± 0.24 m a^{-1} for 1985–2018. Detailed analysis of the data revealed a clear shift from slight thickening (0.14 ± 0.17 m a^{-1}) in 1985–2001 to rapid thinning (-1.31 ± 0.20 m a^{-1}) in 2001–2018. Glaciers terminating in shallower fjords directly connected to Baffin Bay showed a thinning rate 40% lower than those in the Inglefield Bredning region. Among the glaciers studied, Tracy and Farquhar Glaciers located in Inglefield Bredning thinned most rapidly, at a rate exceeding -9 m a^{-1} in the period 2001–2018.

Since the late 1990s, warming trends were observed in both atmospheric (0.09°C a^{-1} in 1996–2009) and ocean temperatures (0.18°C a^{-1} in 1996–2012), which are the most likely triggers of the regime shift at around 2000. In addition to the climatic influence, ice speed acceleration might have enhanced the observed surface lowering as a result of dynamic thinning. The glacier change showed a substantially large spatial

heterogeneity, which is attributed to the glacier geometry and fjord bathymetry. Glaciers terminating in deep fjords have lost greater mass because they are subjected to greater acceleration and are more affected by ocean warming.

To monitor the supraglacial lake evolution, I implemented a supervised machine learning methodology for SGL identification in Google Earth Engine, creating an automatic method for mapping SGLs over two major marine-terminating glaciers (Tracy and Heilprin Glaciers) in deep Inglefield Bredning, northwestern Greenland between 2014 and 2021. The machine learning classification is achieved by using a random forest classifier, which is trained using spectral data from manual-selected areas over the studied glaciers. The classifier performs well across the studied glaciers throughout multiple melt seasons, achieving overall accuracy of 98.48% and 98.56% for Landsat-8 and Sentinel-2 imagery dataset, respectively.

For the lake distribution, although the basin areas of Heilprin and Tracy glaciers are similar (654 km^2 and 540 km^2), the maximum lake surface area on Heilprin glacier (22.84 km^2) was three times greater than that on Tracy glacier (7.60 km^2). On both glaciers, the lake areas are relatively small and have a low occurrence frequency in the low elevations (0–400 m), however, the lakes tend to form larger at middle elevations (400–800 m) and recur at the same location annually, the average lake area is largest in the high elevations (800–1200 m) but the occurrence frequency is not as high as that in the middle elevations.

For the temporal evolution, lakes began formation in early June, which was followed by substantial expansion from middle of June. After reaching a maximum thereafter, the lake area decreases obviously in August. The area peaked in different timing every year, depending on meteorological conditions. In 2016, 2019, and 2020, lake area reached peak values between late June and beginning of July. In 2017 and 2018, however, the peaks were observed later in late July because of cold summer temperature. Regard to the inter-annual variation, peak lake coverage reached 12.41 km^2 for Heilprin Glacier and 4.05 km^2 for Tracy Glacier. However, in 2017 and 2018, the lake extents

are anomalously low for both glaciers, and the anomaly low extents are mainly attributed to the lake undeveloped above 800 m a.s.l.

To find the controlling factors for the lake evolution, I compared the lake area dataset with glacier surface topography, ice speed, air temperature, modelled surface mass balance and snowmelt. The result revealed that most of the lakes developed within the surface depressions and preferentially located away from steep slopes and fast-flow areas. Supraglacial lakes spread from lower to higher elevations as the temperature reaches above-freezing. Air temperature and melt rate do not necessarily correlate with lake coverage particularly below the elevation of 800 m, because lakewater drains through moulins or fractures as the melt season progressed. The maximum inland expansion of supraglacial lakes depends on the equilibrium line altitude, above which, no lake develops because snow absorbs meltwater.

This study clearly showed a rapid increase in the glacier mass loss in the 21st century and provided high spatial and temporal resolution records of supraglacial lake evolution in northwestern Greenland. Together with the drivers for the elevation change and lake evolution identified by the analysis, the study results help our understanding of ongoing glacier changes as well as the future evolution of the Greenland ice sheet.

Contents

List of figures

List of tables

Chapter 1
General introduction

1.1 Greenland ice sheet mass balance

The Greenland ice sheet (GrIS) is the second largest ice mass in the world, following the Antarctic ice sheet. It extends almost 2500 km from north to south and up to 1000 km from east to west, with a total area of 1.74×10^6 km^2 (ice caps, ice fields and glaciers are not included, Benn and Evans, 2014). The GrIS contains ice volume of 2.9×10^6 km^3 in total (Morlighem et al., 2017), accounts for 10% of the Earth's freshwater resources (Benn and Evans, 2014) and has a potential to raise global sea level by 7.4 m (Morlighem et al., 2017). Recent observations suggest that ice mass loss from the GrIS has accelerated over the last two decades at an average rate of -200 ± 12 Gt a^{-1} (Smith et al., 2020). Although ice mass within the interior areas of the GrIS has increased slightly in recent years, significant mass loss concentrated around the entire periphery of the GrIS (Fig. 1.1, Noël et al., 2018; Smith et al., 2020).

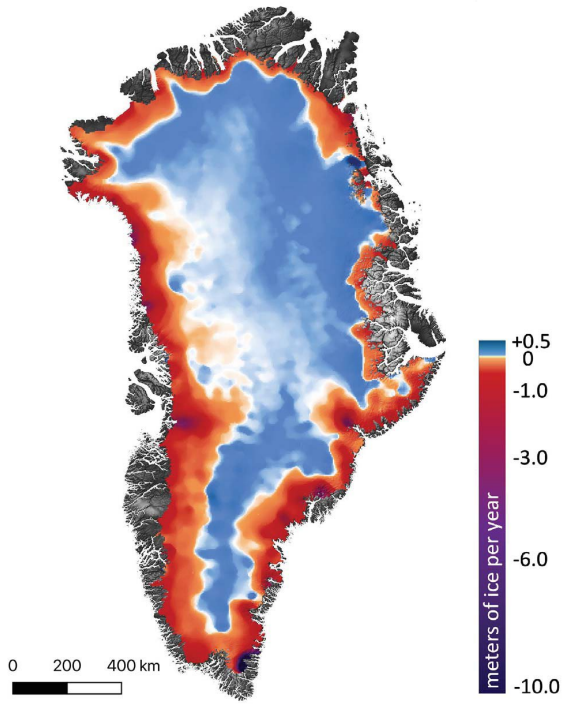

Figure 1.1 Mass loss from Greenland Ice Sheet between 2013 and 2019
(Calculated in meters of ice equivalent per year, Smith et al., 2020).

The total mass balance (MB) is an important indicator of the ice sheet, and the total mass balance is determined by two main class of process: (1) surface mass balance (SMB), which is a process mainly in response to the changing atmospheric conditions and (2) ice discharge (D) occurs at the interface between the ice sheet and the ocean, affected by the interaction between atmosphere, ocean, and other processes. Usually, the MB can be defined as the difference between SMB and D. Components of SMB and D and relevant processes are visualized in Fig. 1.2. SMB is the net difference between accumulation and ablation (Cogley et al., 2010). The dominant source of accumulation for ice sheet is precipitation, which include the liquid water (rain) and solid water (snowfall) from the atmosphere to the ice sheet surface. In addition, the refreezing may also contribute a small part to the mass accumulation (Lenaerts et al., 2019). Ablation removes ice from the ice sheet, which dominates by the melt of snow and ice, besides, ablation also occurs through wind drift and sublimation as a small part (Lenaerts et al., 2019). D is the mass loss along the margins of the GrIS where outlet glaciers terminate in fjords, through iceberg calving (Benn et al., 2017) from the glacier front and submarine melting (Straneo and Cenedese, 2015) of the calving front and underneath the floating ice tongues.

Ice mass loss from the GrIS has accelerated over the last recent decades, with the mass loss increased from 41 ± 27 Gt a^{-1} in 1990–2000 to 286 ± 20 Gt a^{-1} in 2010–2018 (Mouginot et al., 2019), contributed 10.8 ± 0.9 mm to global sea level rise since 1992 (Shepherd et al., 2020). Two thirds of the total mass loss attributed to D and the other one third is contributed by SMB. Among the total mass loss, 66% of which is attributed to an 18 % increase in D (2010–2018 relative to 1972–2000) and the other 34% is attributed to an increase in surface melting that reduced the SMB by 48 % (Mouginot et al., 2019). Understanding the mass balance of the GrIS is important for us to project the future sea-level rise and the potential effect on coastal communities.

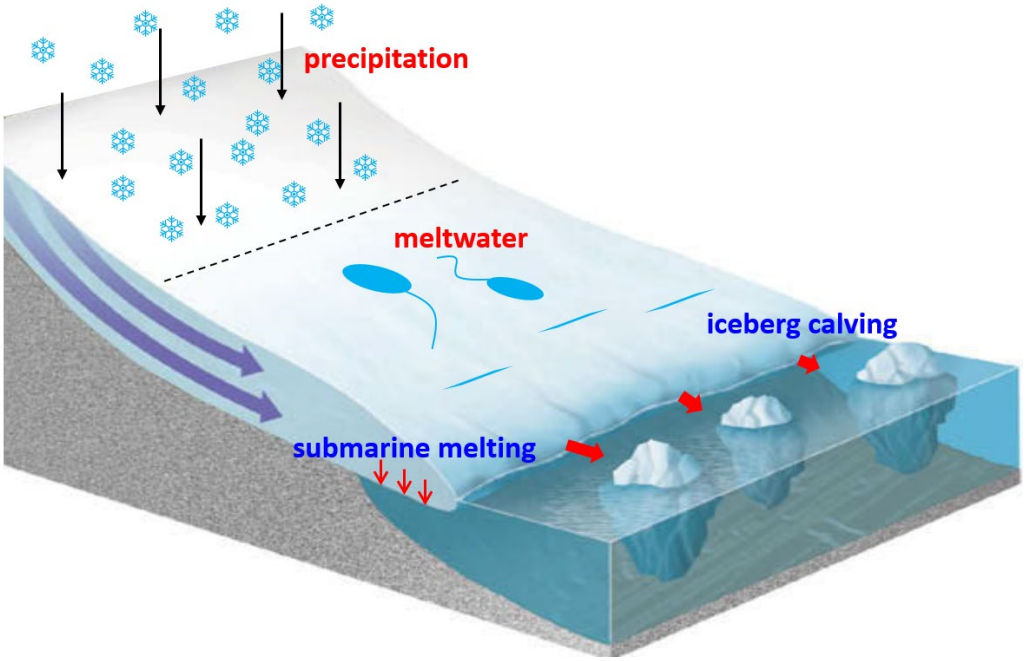

Figure 1.2 Illustration of relevant mass balance processes on the GrIS
(Modified from Grotzinger and Jordan, 2014).

1.2 Mass loss from marine-terminating outlet glaciers

Marine-terminating glaciers, also known as tidewater glaciers, are defined as ice masses that contact the ocean along a grounded terminus, floating terminus, or ice shelf (Cogley et al., 2010). Marine-terminating glaciers are widely distributed in Antarctica, Greenland, Alaska, Arctic, and Patagonia, many of which are undergoing thinning, acceleration, and retreat. Iceberg calving from marine-terminating glaciers is an important component of mass loss from the polar ice sheets and glaciers in many parts of the world, and the marine-terminating glaciers act as conveyor belts moving ice mass from the ice sheet interior to the ocean (Catania et al., 2020).

Mass loss from the GrIS is mainly concentrated in the coastal area (Fig. 1.1), as a result of increased negative SMB and increased ice discharge from marine-terminating outlet glaciers (Enderlin et al., 2014), There are over 280 fast-flowing (>100 m a^{-1}) marine-terminating glaciers (Fig. 1.3) with a high degree of heterogeneity across a range of parameters (Mankoff et al., 2019). Large variations among individual glacier in frontal width (1–30 km), ice thickness (~100–2000 m), terminus basal conditions (grounded,

partially floating, fully floating), glacier forefront conditions (open water, mélange, bergy bits, sea ice, ice shelf presence), basal substrate (bedrock, sediments, water), and other topographic controls (Catania et al., 2020).

Marine-terminating glaciers exist in an environment contact with ocean and atmosphere. They are therefore not only controlled by the internal factors like substrate composition, geometric properties, and ice dynamics, but also influenced by external climatic factors from both ocean and atmospheric properties (Carr et al., 2013). In general, marine-terminating glaciers retreat, accelerate and thin more rapidly than land-terminating glaciers as a result of frontal ablation from the calving front, which is largely controlled by ice dynamics (King et al., 2020). In the GrIS, the ice dynamics induced mass loss account for more than half of the total mass loss (Mouginot et al., 2019) and will remain a primary driver of the mass loss over the next century (Choi et al., 2021).

To understand the processes that control mass loss from marine-terminating glaciers, the relationship between calving and glacier dynamics is a major issue to be solved. One explanation is that caving losses trigger a cascade of dynamic changes up-glacier, including acceleration and dynamic thinning (Meier and Post, 1987, Howat et al., 2005). In this view, calving is the first order driving process, and the ice dynamic changes in response to that driving. Another explanation, in contrast, portrays that coupled dynamical and geometric changes to the glacier system drive increased caving rate. In this view, the flow acceleration and thinning control calving activity (Van der Veen, 1996, 2002). Both explanations are supported by empirical research, with some studies treated calving as the ‘master’ (Motyka et al., 2003, Joughin et al., 2004) and others pointed calving as the ‘slave’, that changes in terminus dynamics and glacier thinning may precede increased calving (Fischer and Powell, 1998, Kirkbride and Warren, 1999). Therefore, it is often difficult to attribute an observed dynamic change in the marine-terminating glacier to a particular process because changes in these processes can be superimposed interact with each other (Benn et al., 2007). Considering the importance and complexity of the process of marine-terminating glacier, it is important to

understand the change of marine-terminating glaciers under the warming climate to improve the future projection of sea level rise.

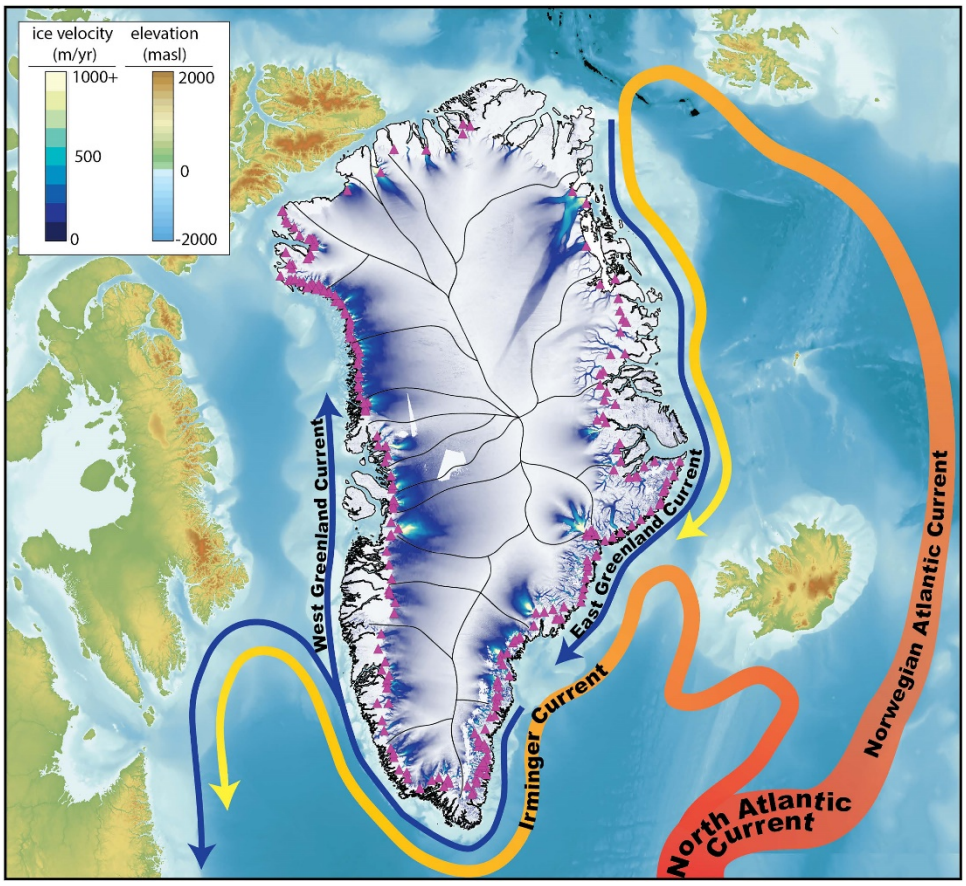

Figure 1.3 Illustration of GrIS and surround area
Arrows indicate the ocean current around GrIS. Purple triangles indicate marine-terminating glaciers with ice speed faster than 50 m a^{-1}(Catania et al., 2020).

1.3 Mass change for northwestern Greenland

Northwestern Greenland (defined as Mouginot et al., 2019) holds a 127 cm sea level equivalent over 2.8×105 km^2 drained by 64 marine-terminating glaciers (Mouginot et al., 2019). Ice discharge through the marine-terminating glaciers there increased by 45% from 1990–2000 (87 Gt a^{-1}) to 2010–2018 (112 Gt a−1) (Mouginot et al., 2019). The total ice mass from near balance in the 1970s to a small loss in the 1980s, then equilibrium between 1995 and 2000, before a rapid loss from 2000 to 2018 (Fig. 1.4, Mouginot et al., 2019). The cumulative loss is 1578±56 Gt a^{-1}, or 4.4±0.2 mm sea level equivalent between 1972 and 2018, which contributes the largest to the total mass loss

in Greenland (Mouginot et al., 2019).

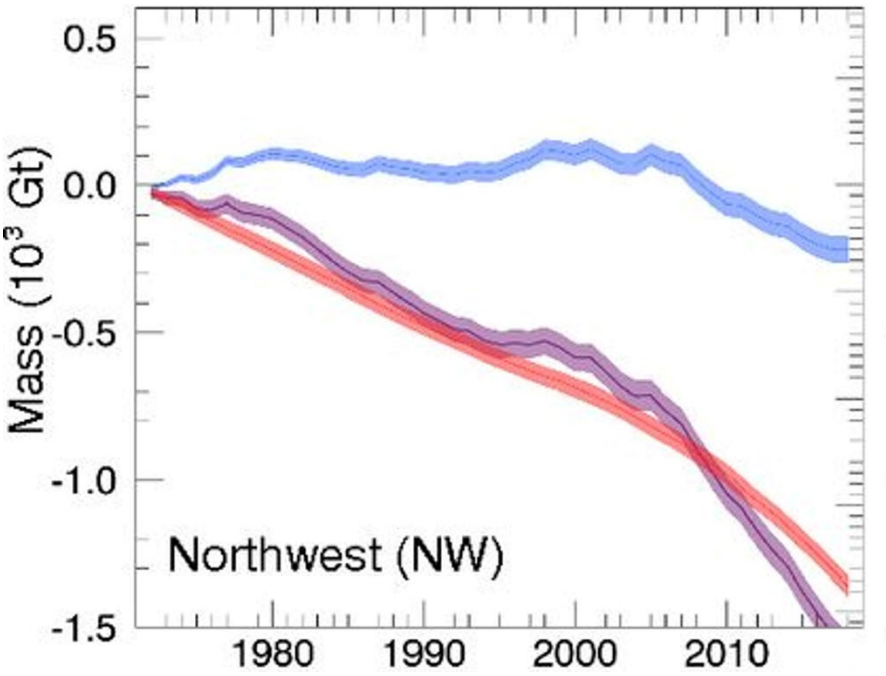

Figure 1.4 Cumulative anomalies in mass change for northwestern Greenland SMB (blue), D (red), and MB (purple) are calculated in gigatons for the time period 1972–2018 (Mouginot et al., 2019).

Northwestern Greenland, as the largest contributor to the mass loss of the GrIS (Khan et al., 2022; Mouginot et al., 2019), it is of great importance to monitor the glaciers there. Through the continuous satellite monitoring, most glaciers in Northwestern Greenland have retreated over the observation period and widespread regional retreat accelerated from around 1996 (Black and Joughin, 2022; Bunce et al., 2018). The acceleration of glacier retreat is most sensitive to increases in runoff and ocean temperatures (Black and Joughin, 2022), this trend is in consistent with the ocean and runoff-induced (Slater et al., 2021) glacier change for whole Greenland. In addition to the glacier retreat, acceleration, and relevant dynamic change of the marine-terminating glacier in Northwestern Greenland have been reported (Moon et al., 2012; Sakakibara and Sugiyama, 2018; Mcfadden et al., 2011). Surface elevation changes and surface mass balance are also have been studied along the coast of Melville Bay in Northwestern Greenland by Kjær et al. (2012), the result demonstrated a significantly glacier thinning (Fig. 1.5) in this region and the importance of glacier dynamics in the

recession of the ice sheet, the widespread dynamic thinning in Northwestern Greenland is also has been reported by Pritchard et al. (2009). However, these previous studies were usually carried out in sub-decadal temporal scale not fully covered the Northwestern Greenland, thus long timescale and large-spatial- covered observations are needed to investigate the mechanisms of the changes in marine-terminating outlet glaciers.

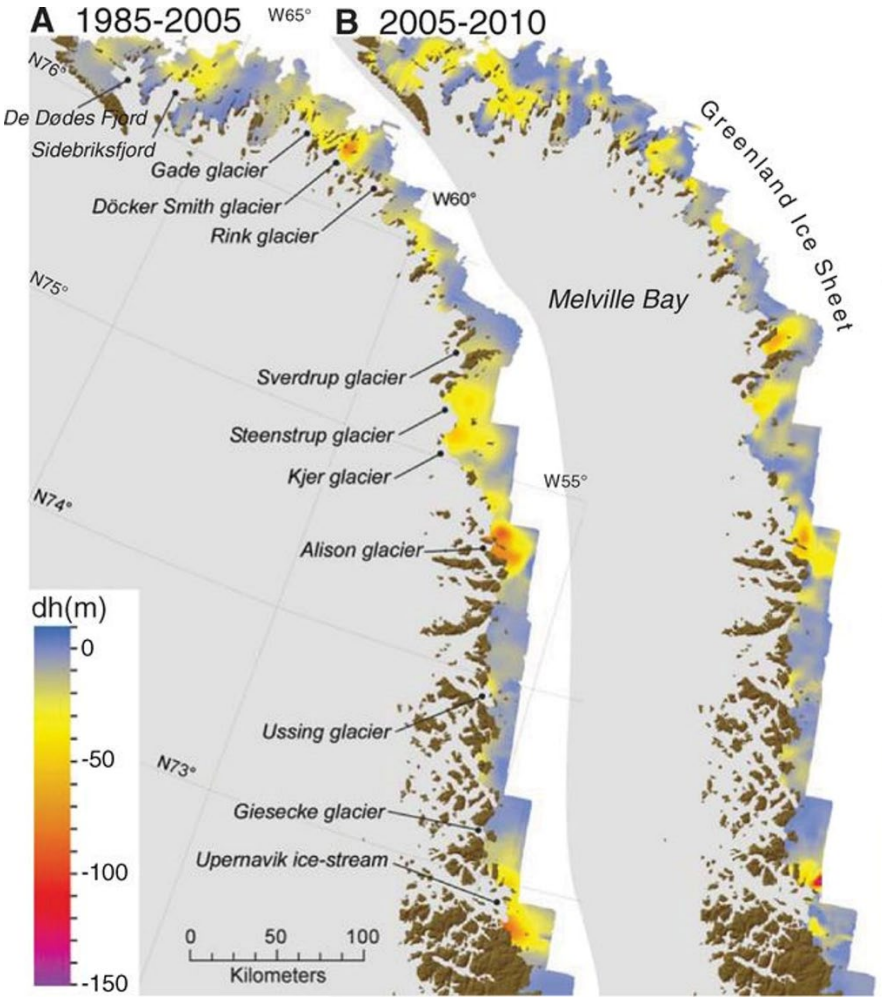

Figure 1.5 Total surface elevation changes (dh) in northwestern Greenland. Data derived from DEMs generated from aerial photographs recorded in 1985, ICESat data from 2005, and ATM data from 2005 and 2010. (A) dh for the 1985–2005 period. (B) dh for the 2005–2010 period (Kjær et al., 2012).

1.4 Supraglacial lakes

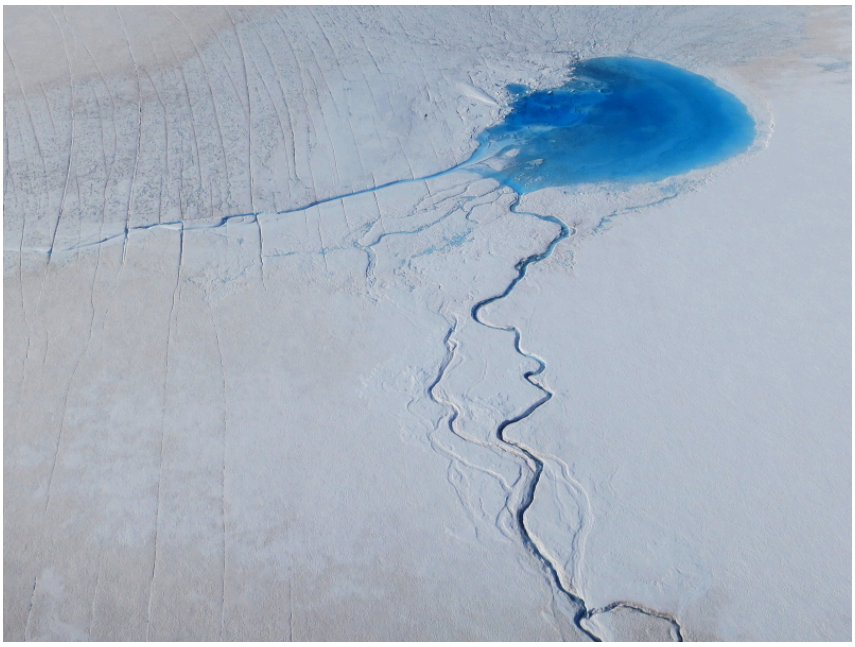

Figure 1.6 Supraglacial lake located in northwestern GrIS.
(Image credit: Shin Sugiyama).

Supraglacial lakes (Fig. 1.6) form annually when runoff (meltwater and rain) accumulates in topographic depressions on the surface of glaciers, ice sheets and ice shelves (Echelmeyer et al., 1991), and widely distributed in the ablation area of the GrIS primarily during the melt season. Generally, they may affect the mass balance of the GrIS in three ways. First, they reduce the albedo of the glacier surface and enhances shortwave radiation absorption. The melt beneath lakes is estimated to be 110–135% (Tedesco et al., 2012) greater than the nearby bare ice from in situ measurements and 110–170% from models (Lüthje et al., 2006). Second, the rapid drainage of supraglacial lakes through hydrofracture deliver a large amount of meltwater into the bed of glaciers within hours to days, reducing basal friction and subsequently causing short-term velocity changes and sustained uplift (Chudley et al., 2019; Das et al., 2008; Doyle et al., 2013; Stevens et al., 2015). Third, on the seasonal scale, the meltwater input into the subglacial system have the potential to affect or alter the glacier dynamics through the melt-induced acceleration (Bartholomew et al., 2010; Sundal et al., 2011; Moon et al., 2014).

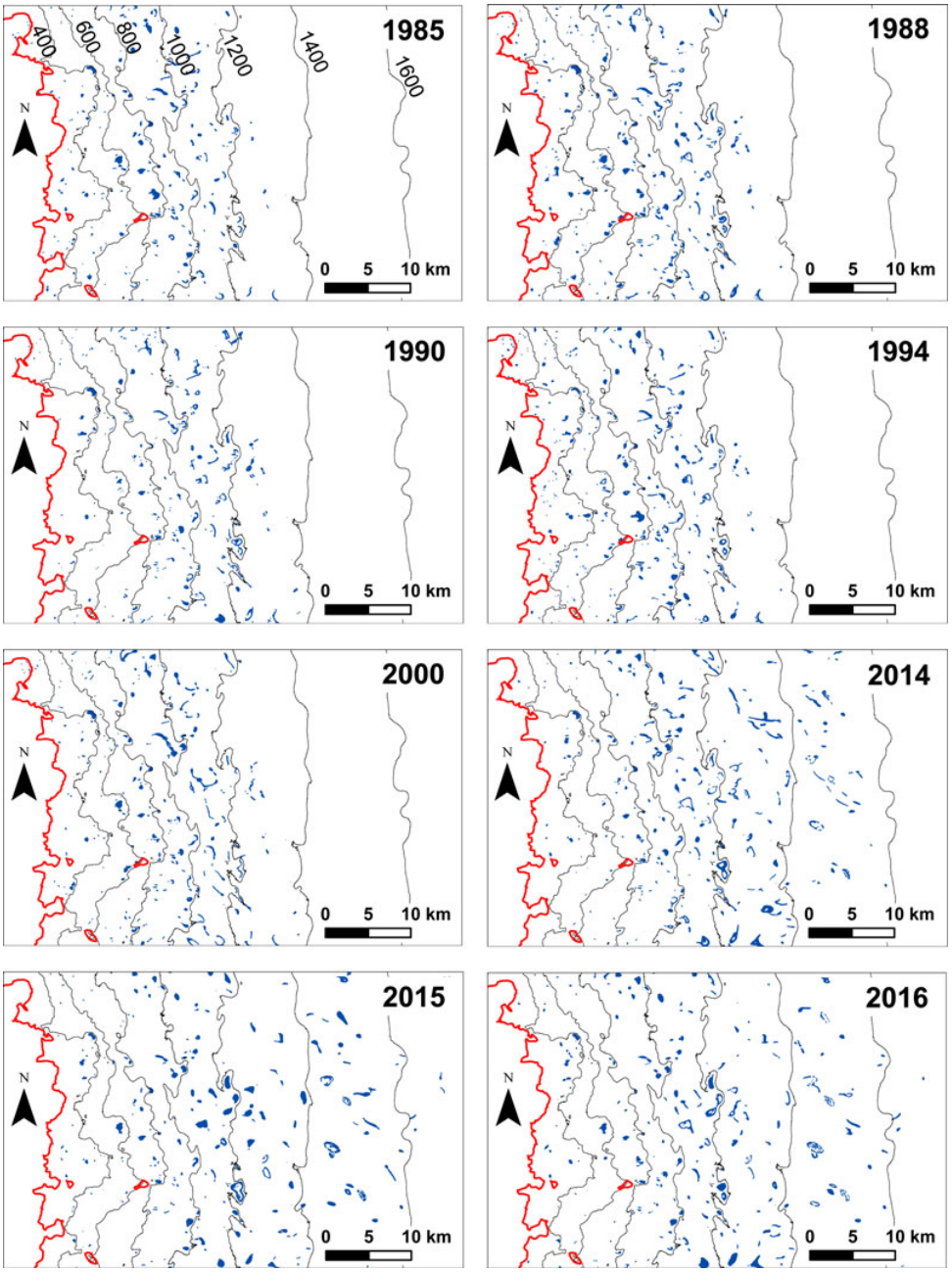

Figure 1.7 Inland advance of supraglacial lakes
Research conduct in north-western sector of the GrIS for the 8 years between 1985 and 2016, showing lakes forming at higher elevations and growing in total areal coverage over the study period (Gledhill and Williamson, 2018).

Over the long-time timescales (inter-annual to decadal), a substantial number of supraglacial lakes are observed inland sectors around the margin of the GrIS. These supraglacial lakes expanded their distribution inland after 2000 by hundreds of meters to tens of kilometers. Among which, supraglacial lakes extended most significantly in Jakobshavn Isbræ, reaching approximately 30 km further inland in 2012 than before

2000 (Howat et al., 2013). A more recent study conducted in Northwestern Greenland reported that distribution of supraglacial lakes has advanced to higher maximum (+418 m) and mean (+299 m) elevations between 1985 and 2016, as well as a near-doubling of total lake areas and volumes in the study site (Gledhill and Williamson, 2018). As reported in Howat et al. (2013), inland advance and area/volume increase are observed particularly after 2000. The increases in area/volume are primarily driven by increases in lake extent in the highest ($\geqslant$ 1200 m a.s.l.) elevation regions (Gledhill and Williamson, 2018). In addition to the direct satellite observations, a simulation study led by Leeson et al. (2015) showed that supraglacial lakes are likely to spread 103 and 110 km further inland by the year 2060 under moderate (RCP 4.5) and extreme (RCP 8.5) climate change scenarios, respectively in southwest Greenland. According to their empirical-evidence-based speculation, the area of supraglacial lakes would increase by 48–53% over the whole GrIS (Leeson et al., 2015). A subsequent study combined surface depressions from DEM and modelled future runoff from regional climate model to forecast the future supraglacial lake extent (Ignéczi et al., 2016). The result was similar that approximately 9.8±3.9 km^3 (+113% compared to 1980-2009) or 12.6±5 km^3 (+174% compared to 1980-2009) of meltwater could be stored in supraglacial lakes under moderate (RCP 4.5) and extreme (RCP 8.5) scenarios by the year of 2070–2099, respectively (Ignéczi et al., 2016). In a warming scenario, the amplification of supraglacial lake expansion may enhance the surface melting and lead positive feedback to the mass loss.

Therefore, either in the short timescale, or in the long timescale, supraglacial lakes have the impact on ice sheet mass balance. Long-term and more intensive observations can help us better understand the role of supraglacial lake in the GrIS.

1.5 Objective of this study

The objective of this study is to monitor glacier elevation and supraglacial lake changes in marine-terminating glaciers in northwestern Greenland from remote sensing. To

understand the glacier elevation and the lake evolution, I extract elevations from digital elevation model (DEMs) and digitalized lake extent from optical satellite imageries. These variables were then compared with other potential related factors to investigate mechanisms controlling these observed changes. To achieve these objectives, this thesis is broadly divided into two parts of research:

1. Surface elevation change of glaciers (15 marine-terminating glaciers and 1 land-terminating glacier) along the coast of Prudhoe Land, Northwestern Greenland from 1985 to 2018
2. Supraglacial lakes evolution on Tracy and Heilprin Glaciers (most two largest marine-terminating glaciers in the glaciers studied in part 1) from 2014 to 2021, Northwestern Greenland

In the first part, I used both satellite images and aerial photographs derived DEM data to quantify the mass loss of 16 glaciers (15 marine-terminating and 1 land-terminating glaciers) in the study area from surface elevation change from 1985 to 2018. To interpret accelerated glacier thinning revealed by the satellite data, the mechanisms of the glacier change was investigated based on air/ocean temperature, ice dynamics and fjord bathymetry.

In the second part, I applied a machine learning method to remote sensing data through Google Earth Engine platform. By utilizing the method, I derived a high-temporal resolution time serials of lake extent. To interpret the lake distribution pattern, DEM and other glacier relevant data were used to investigate the possible factors that controlling the lake distribution. To explain intra-annual and inter-annual lake extent variation patterns, relevant meteorological data and modelling SMB and runoff output were taken into consideration to discuss the potential factors that affect the formation of the lakes.

Chapter 2

Surface elevation change of glaciers along the coast of Prudhoe Land, northwestern Greenland, from 1985 to 2018

The content of this chapter was published as a journal article: Wang, Y., Sugiyama, S., & Bjørk, A. A. (2021). Surface elevation change of glaciers along the coast of Prudhoe Land, northwestern Greenland from 1985 to 2018. *Journal of Geophysical Research: Earth Surface*, 126, e2020JF006038. https://doi.org/10.1029/2020JF006038

2.1 Introduction

Ice mass loss from the Greenland Ice Sheet has been increasing over the past two decades (e.g. Mouginot et al., 2019; Shepherd et al., 2020; Smith et al., 2020). Ice loss between 1992 and 2018 is equivalent to 10.8±0.9 mm sea level, accounting for approximately 20% of the sea-level rise observed during the same period (Shepherd et al., 2020; Watson et al., 2015). Mass loss is observed primarily along the coast of Greenland, as a result of increasingly negative surface mass balance in the ablation area and accelerated ice discharge from marine-terminating outlet glaciers (Catania et al., 2020; Enderlin et al., 2014). Observations and mass balance modeling revealed that ~40% of the total mass loss of the ice sheet between 1991 and 2015 was caused by an increase in ice discharge from outlet glaciers (van den Broeke et al., 2016). The outlet glaciers are sensitive to climate change because mass balance and ice dynamics are strongly controlled by both atmospheric and oceanic conditions. Therefore, assessing the mass loss of the Greenlandic outlet glaciers under the rapidly changing Arctic climate is crucial for the prediction of sea level rise in the near future (Bjørk et al., 2012; Catania et al., 2020; Hanna et al., 2020).

To quantify glacier mass change over a large area on a decadal temporal scale, remote sensing is a suitable and commonly employed approach. Near the coast of Greenland, repeated laser altimetry by NASA's Airborne Topographic Mapper (ATM) indicated

thinning of the ice during the 1990s at a rate exceeding 1 m a^{-1} (Krabill et al., 2000, 2004). Based on the combination of ATM and subsequent ICESat altimetry datasets, Csatho et al. (2014) revealed that 48% of the ice sheet mass loss from 1993 to 2012 was due to dynamic thinning (vertical straining due to accelerated ice flow). The laser altimetry provides a precise measure, but the incomplete data between satellite tracks limits spatial resolution of elevation analysis over a relatively small area. As an alternative method for measuring glacier elevation change in Greenland, digital elevation models (DEMs) derived from satellite or aerial images have been applied in recent years. By means of DEM differencing, mass loss of outlet glaciers has been evaluated in northeastern Greenland (Khan et al., 2014), on Melville Bay in northwestern Greenland (Kjær et al., 2012) and along the entire margins of the Greenland Ice Sheet (Kjeldsen et al., 2015). The results indicate that glacier mass loss has increased over the Greenland Ice Sheet since the 2000s. More recently, surface elevation change of 1526 peripheral glaciers and ice caps in west-central Greenland has been quantified as 0.5 ± 0.2 m a^{-1} for the period from 1985 to 2012 (Huber et al., 2020). However, the timing of the mass loss and its magnitude are highly heterogeneous across Greenland and for each glacier (e.g. Khan et al., 2010; Moon et al., 2012). Thus, it is crucial to perform a detailed regional analysis by taking climatic and geometrical settings into consideration. Marine-terminating glaciers exhibit a particularly high degree of spatial variability, even within a relatively small region (Porter et al., 2018). For example, 37 marine-terminating glaciers in central east Greenland showed a significantly large variation in surface elevation change, ranging from −156 to +7 m between 2000 and 2010. The authors concluded that coastal ocean heat transport was primarily responsible for the glacier change (Walsh et al., 2012). Therefore, comparison of glacier changes under different settings in terms of fjord geometry, ocean temperature, circulation, and stratification, which control ice-ocean interactions (Straneo et al., 2010), may help us better understand the mechanisms controlling glacier change.

Tidewater glaciers in northwestern Greenland have shown rapid thinning (Pritchard et al., 2009; Kjær et al., 2012), significant acceleration (Moon et al., 2012) and persistent terminus retreat (Bunce et at., 2018) since the 2000s, and are important contributors to the mass loss of the Greenland Ice Sheet (Mouginot et al., 2019). However, the previous studies focused on Melville Bay, located in the southern part of northwestern Greenland. More recently, Sakakibara and Sugiyama (2018, 2020) reported variations in the ice front positions and flow speed of marine-terminating glaciers along the coast of Prudhoe Land, which is situated 300 km north of Melville Bay (Fig. 2.1). Synchronized glacier retreat and acceleration began around 2000 (Sakakibara and Sugiyama., 2018), approximately the same time as the rapid change of the glaciers in Melville Bay (Moon et al., 2012; Carr et al., 2013b; Bunce et at., 2018). Surface elevation change has been reported for some of the glaciers along the coast of Prudhoe Land, e.g. Bowdoin and Tugto Glaciers (Tsutaki et al., 2016), Tracy and Heilprin Glaciers (Porter et al., 2014; Willis et al., 2018), which highlights a significant heterogeneity in the magnitude and timing of the glacier change. Despite the effort of the previous studies, observations of surface elevation change in the region are limited to the individual glaciers. Moreover, elevation change over the 20th century has not previously been reported in the Prudhoe Land region.

In this study, I used the recently released AeroDEM (Korsgaard et al., 2016) and ASTER-VA DEM (Fujisada et al., 2005, Hirano et al., 2003) to assess the surface elevation changes of all the glaciers along the coast of Prudhoe Land. I analyzed spatial variations in the elevation change from 1985 to 2018, as well as the change in the trend between two subperiods (1985–2000 and 2000–2018). Each individual glacier was assessed, as well as the glacier groups subdivided into those terminating in Inglefield Bredning and those facing Baffin Bay (Fig. 2.1). Subsequently, I discuss possible drivers of recent rapid glacier change, as well as controls of spatial and temporal patterns of the glacier mass loss.

2.2 Study site

I studied 16 outlet glaciers of the Greenland Ice Sheet located along the coast of Prudhoe Land in northwestern Greenland (Fig. 2.1). The glaciers are distributed across the area of 77.45–78.03°N and 65.95–72.03°W. Of all the glaciers studied, only Tugto Glacier terminates on land; the other 15 are marine-terminating glaciers. Glaciers in the eastern part (Heilprin, Tracy, Farquhar, Melville, Sharp, Hart, Hubbard, and Bowdoin) feed into Inglefield Bredning, a fjord with a width of approximately 20 km and a length of 80 km. Glaciers located in the western part of the study site (Sun, Verhoeff, Meehan, Morris Jesup, Diebitsch, Clements, and Bamse) feed into relatively small fjords, which have short and direct connections to Baffin Bay.

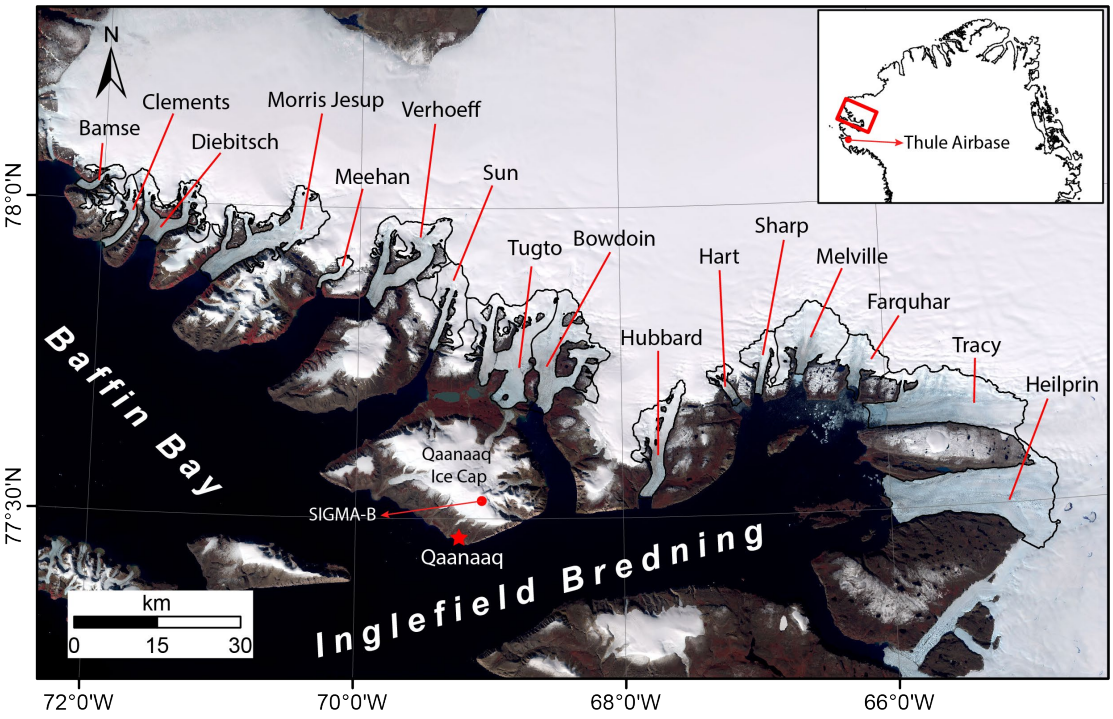

Figure 2.1 Overview of the study site
Glaciers are studied along the coast of Prudhoe Land in northwestern Greenland. The background is a mosaicked Sentinel-2 image taken in August 2020. The black lines are the glacier mask boundaries as I introduced in 2.1.4. The inset shows the location of the study site and Thule Airbase in Greenland.

The marine-terminating outlet glaciers along the coast of Prudhoe Land showed frontal retreat between the 1980s and 2014. Most of the glaciers began retreating after 2000, with substantial acceleration observed at those terminating in Inglefield Bredning.

From 2000 to 2014, Tracy, Heilprin, Farquhar, and Bowdoin Glaciers retreated at a rate greater than 80 m a^{-1}. Tracy, Melville, Farquhar, and Heilprin Glaciers accelerated at a rate in excess of 10 m a^{-2} (Sakakibara and Sugiyama, 2018). Glaciers in the region showed seasonal ice speed variations with an initial speedup between late May and early June, a peak speed between late June and early July, and subsequent decrease from July to September, while the timing and magnitude of the speedup varies among these glaciers (Sakakibara and Sugiyama, 2020).

The largest two glaciers in this area, Heilprin and Tracy Glaciers located in the easternmost part of Inglefield Bredning (Fig. 2.1), have a width of 5.7 and 5 km, respectively (Hill et al., 2017). They are separated by only 20 km in distance but have shown significantly different patterns of frontal variations. Tracy Glacier has retreated by ~15 km since the 19th century, whereas the retreat of Heilprin Glacier during the same period was only several kilometers (Dawes and van As, 2010). From 1980 to 2014, the frontal displacement rates of Tracy and Heilprin Glaciers were −200 m a^{-1} and −56 m a^{-1}, respectively (Sakakibara and Sugiyama, 2018). Although both glaciers have shown acceleration between 2000 and 2014, Tracy Glacier (51 m a^{-2}) accelerated almost four times faster than Heilprin Glacier (13 m a^{-2}) (Sakakibara and Sugiyama, 2018). Contrasting patterns were observed also in the change in glacier thickness between 2011 and 2012, i.e. Tracy Glacier showed a thinning rate double (−12 m a^{-1}) that of Heilprin Glacier (−6 m a^{-1}) (Porter et al., 2014). More recently, from 2016 to 2017, Tracy Glacier thinned by 9.9 m near the terminus while the thinning at Heilprin Glacier was only 1.9 m (Willis et al., 2018). Previous studies attribute the more rapid retreat of Tracy Glacier to the difference in the depth of the fjord. Tracy Glacier terminates in deeper water than Heilprin Glacier (> 600 m at Tracy Glacier and ~350 m at Heilprin Glacier), therefore the ice is plausibly more exposed to warmer deep water and subjected to rapid submarine melting (Porter et al., 2014, 2018; Willis et al., 2018). Bowdoin Glacier is a 3-km-wide glacier terminating in Bowdoin Fjord, a 20-km-long fjord connected to Inglefield Bredning (Fig. 2.1). This glacier thinned at a rate of −4.1

m a^{-1} between 2007 and 2010, which was roughly 50% faster than the adjacent land-terminating Tugto Glacier (−2.8 m a^{-1}) (Sugiyama et al., 2015; Tsutaki et al., 2016). This result highlights the importance of ice dynamics and ice-ocean interactions in the recent thinning of marine-terminating glaciers in this region.

2.3 Data and methods

2.3.1 AeroDEM

AeroDEM is a product derived from aerial photographs taken between 1978 and 1987 (Korsgaard et al., 2016). This DEM covers the entire margins and surrounding region of the Greenland Ice Sheet with a spatial resolution of 25 m. The accuracies in horizontal and verticaldirections are reported as < 10 and < 6 m, respectively, while the precision is greater than 4 m (Korsgaard et al., 2016). This product has been used in previous studies for evaluating mass loss along the margins of the Greenland Ice Sheet (Khan et al., 2014; Kjær et al., 2012; Kjeldsen et al., 2015; Mouginot et al., 2019; Felikson et al., 2017) and peripheral glaciers (Abermann et al., 2020; Huber et al., 2020; Marcer et al., 2017; von Albedyll et al., 2018). The part of AeroDEM used in this research was generated from aerial photographs taken in 1985.

2.3.2 ASTER-VA DEMs

The Advanced Spaceborne Thermal Emission and Reflection Radiometer (ASTER) is an imaging instrument, developed by Japan and the USA, onboard the Terra satellite launched in December 1999. Advanced Industrial Science and Technology in Japan distributes value-added ASTER data (ASTER-VA), which contain DEMs derived from stereo pair ASTER images (https://gbank.gsj.jp/madas/). Each ASTER-VA DEM covers an area of 60 × 60 km^2, with a horizontal resolution of 30 m (Fujisada et al., 2005, Hirano et al., 2003). Fujisada et al. (2005) reported that the vertical accuracy of ASTER-VA DEM is 20 m with 95% confidence. I used 13 ASTER-VA DEMs between 2001–2003 and 2016–2018. To select DEMs acquired late in the ablation season with

minimal influence of cloud and snow cover, corresponding ASTER visible and near-infrared nadir band (vnir3n) images were inspected. Dates and IDs of the utilized DEM are summarized in Table 2.1.

Table 2.1 Acquisition dates and IDs of the DEMs used in this study

Periods	Date	ID
T0	1985	AeroDEM
T1	05/26/2001	ASTB010526180527
	06/11/2001	ASTB010611180453
	06/11/2001	ASTB010611180502
	06/13/2001	ASTB010613175235
	09/03/2001	ASTB010903173817
	09/03/2001	ASTB010903173825
	06/12/2003	ASTB030612173751
T2	07/29/2016	ASTB160729180254
	08/17/2017	ASTB170817180231
	08/20/2017	ASTB170820183317
	08/13/2018	ASTB180813175727
	08/24/2018	ASTB180824173910
	08/31/2018	ASTB180831174510

2.3.3 GIMP DEM

GIMP (Greenland Ice Mapping Project) DEM was derived from high resolution panchromatic stereoscopic imagery collected between 2009 and 2015 by GeoEye-1 and WorldView 1–3 (Howat et al., 2014). This DEM, with a spatial resolution of 30 m, is available through the National Snow and Ice Data Center (https://nsidc.org/data/NSIDC-0715/versions/1). In this study, I used GIMP DEM as a reference for co-registration of other DEMs as described in the Method section (3.2.1).

2.3.4 Glacier mask

Surface elevation changes were evaluated over glacier areas defined by the GIMP Land Ice and Ocean Classification Mask (Howat et al., 2014). The glacier boundaries were revised in this study by inspecting ASTER vnir3n images taken in the late ablation season in 2010. DEM differencing was performed over areas below 850 m a.s.l., which are covered by the AeroDEM. Glacial basin boundaries were defined by a previous

study (Mouginot et al., 2019) and glacier areas were subdivided into elevation bands based on the GIMP DEM. The total glacier area analyzed in this study was 1624.54 km^2, as measured in 2010.

2.3.5 Meteorological and oceanic data

Atmospheric temperature recorded at a meteorological station in Qaanaaq (77.48°N, 69.38°W; 16 m a.s.l.), the nearest station to the studied glaciers, is available for the period from 1996 to the present. To extend the investigation into an earlier period, I also used daily mean air temperatures from 1985–2018 at Thule Airbase, (76.53°N, 68.75°W; 77 m a.s.l.) situated 108 km south of Qaanaaq. These temperature data are accessible via the website of the National Oceanic and Atmospheric Administration. The mean summer temperatures (June, July, and August) at Thule Airbase are well correlated with those at Qaanaaq (r^2 = 0.83, p < 0.001). Thus, I assumed that the atmospheric temperature at Thule Airbase and Qaanaaq had a similar variation pattern (Fig. 2.7a), which enabled us to investigate temperature change over the entire study period. In addition to this data obtained at low elevation areas, I analyzed the temperature measured at SIGMA-B, (77.54°N, 69.07°W; 944 m a.s.l.) located on Qaanaaq Ice Cap, where an automatic weather station has been operated since 2012 (Aoki et al., 2014).

I utilized monthly mean ocean temperatures during 1991–2019 from TOPAZ4 Arctic Ocean reanalysis data (Sakov et al., 2012) distributed by the Copernicus Marine Environment Monitoring Service. As a measure of thermal conditions of Polar Surface Water (Bevan et al., 2019), I extracted 5 m potential temperature from TOPAZ4 data and calculated summer mean values (June–August) within an area of 77–78° N and 66–72° W. To assess possible warming in subsurface Atlantic water, I adopted a reconstruction of ocean thermal forcing (depth-averaged temperature above freezing point) from 1992 to 2017 near Inglefield Bredning (76.8–77.3° N, 71–73° W) (Wood et al., 2021). The dataset of thermal forcing is widely used to study the warming of Atlantic water and its role in the recent glacier retreat in Greenland (Wood et al., 2018,

2021; Rignot et al., 2021).

2.3.6 Corrections of DEM biases

To derive surface elevation changes from multi-temporal DEMs, co-registration of the DEMs is necessary to remove potential offsets in horizontal and vertical directions (Nuth and Kääb, 2011). All DEMs were projected to WGS 1984 UTM zone 19N before co-registration. AeroDEM was resampled to a resolution of 30 m by cubic convolution to obtain the same cell size as ASTER and GIMP DEMs. Subsequently, I sampled all DEMs on to the same grid, based on the GIMP DEM.

I employed a three-dimensional co-registration method, as proposed by Nuth and Kääb (2011). The co-registration was performed on terrain with slopes smaller than 45° (Berthier et al., 2016) because performance of DEMs derived from optical stereo-pair images on steep terrain is poor (Toutin, 2002). Horizontal and vertical offsets of AeroDEM were corrected using GIMP DEM as a reference, excluding ice, snow, water surfaces, steep terrain (> 45°), and pixels where elevation differs from the reference DEM by more than 50 m (Berthier et al., 2016). As for the ASTER DEMs, along/cross track biases introduced by satellite acquisition geometry were corrected, based on the method proposed by Nuth and Kääb (2011), which was followed by horizontal and elevation dependent corrections (Gardelle et al., 2013; Nuth and Kääb, 2011). Vertical offsets of the DEMs over the ice-free areas before and after the corrections are shown in Supporting Information (Fig. 2.10). Outliers in the data were excluded, based on previously published elevation change records within the research region. The greatest glacier elevation change reported in my study area was −9.9 m a^{-1} in Tracy Glacier between 2016 and 2017 (Willis et al., 2018). I used these previous estimates as a guide, but set a more conservative threshold because the study area and period are not fully consistent with my research. I also expect surges and other short-term rapid glacier changes, which may not be captured if the tolerance is small. Thus, I excluded pixel values as outliers when the difference relative to the GIMP DEM fell outside the range −20 (twice the previously reported largest thinning rate) to +10 m a^{-1} (set arbitrarily to

capture possible surges). Over the glacier mask analyzed in this study, only 1.5% of the pixels were excluded. The outliers were carefully inspected so that large elevation changes outside of this range due to glacier dynamics such as surging were also included in the analysis.

2.3.7 DEM differencing

I separated the DEMs into three timeframes: (1) the 1985 Aerial DEM, (2) ASTER DEMs acquired from 2001–2003 and (3) 2016–2018, hereafter referred to as T0, T1, and T2, respectively. Elevation change (Δh) and its mean rate ($\Delta h/\Delta t$) were obtained by differencing DEMs for three periods (T0–T2, T0–T1 and T1–T2). All available $\Delta h/\Delta t$ values were mosaicked to produce a $\Delta h/\Delta t$ map for each period, covering all 16 glacier surfaces below 850 m a.s.l. As a measure of the uncertainty in the elevation change, $\Delta h/\Delta t$ on ice-free areas near the glaciers were analyzed in each period and presented as histograms in the supporting information (Fig. 2.11).

Elevation changes were analyzed for every 50 m altitude bin, based on the GIMP DEM. Within each elevation band, I calculated a mean $\Delta h/\Delta t$ after excluding values deviating from the average by more than twice the standard deviation (Berthier et al., 2004; Gardelle et al., 2013), with 5% of pixels excluded in this process. Because elevation change was unavailable near the fronts of rapidly retreating glaciers, I analyzed the lowest elevation bin (0–50 m) only if available data covered more than 10% of the area. Banded structures were observed in the elevation change on Heilprin and Tracy Glaciers (Fig. 2.2), which I attribute to satellite jitter (Girod et al., 2017) and the signals being within the range of uncertainty.

2.3.8 Uncertainty analysis

To estimate the uncertainty in the elevation change, I considered the spatial correlation of the Δh (Gardelle et al., 2013). The estimator was the standard error of the mean (e) defined as

$$e = \frac{E_{\Delta h/\Delta t}}{\sqrt{N_{eff}}}, \qquad (2.1)$$

where $E_{\Delta h/\Delta t}$ represents the standard deviation of the elevation change rate and N_{eff} represents the effective number of the observations on the ice-free area. Considering the spatial correlation (Rolstad et al., 2009), the N_{eff} is given by the total number of observations (N_{tot})

$$N_{\text{tot}} = \frac{N_{eff} \times R}{2d}, \qquad (2.2)$$

where R is the pixel size (30 m) and d (713 m) is the spatial autocorrelation distance, determined by the mean of Moran's I autocorrelation index on elevation differences in the ice-free area (Gardelle et al., 2013). Uncertainties within Inglefield, Baffin Bay and for all of the studied glaciers (e_{region}) were computed by weighting uncertainties obtained in individual glaciers included in each region (e_i) for corresponding glacier areas (A_i).

$$e_{\text{region}} = \frac{\sum_{i=1}^{n} A_i \times e_i}{\sum_{i=1}^{n} A_i} \qquad (2.3)$$

2.4 Results

2.4.1 Elevation changes over the study area

Across most of the glacier areas, surface elevation showed a significant decrease during the entire study period from T0 to T2 (Fig. 2.2a). The mean rate of surface elevation changes over the glaciers studied during T0–T2 was −0.55 ± 0.24 m a^{-1}. All the elevation bands (0–850 m) experienced surface lowering, and the magnitude of the rate decreased in higher elevation (Fig. 2.3a). The most rapid change (−3.08 m a^{-1}) was observed near the glacier termini (elevation band 0–50 m), and the smallest change (−0.14 m a^{-1}) was found in the highest elevation band 800–850 m.

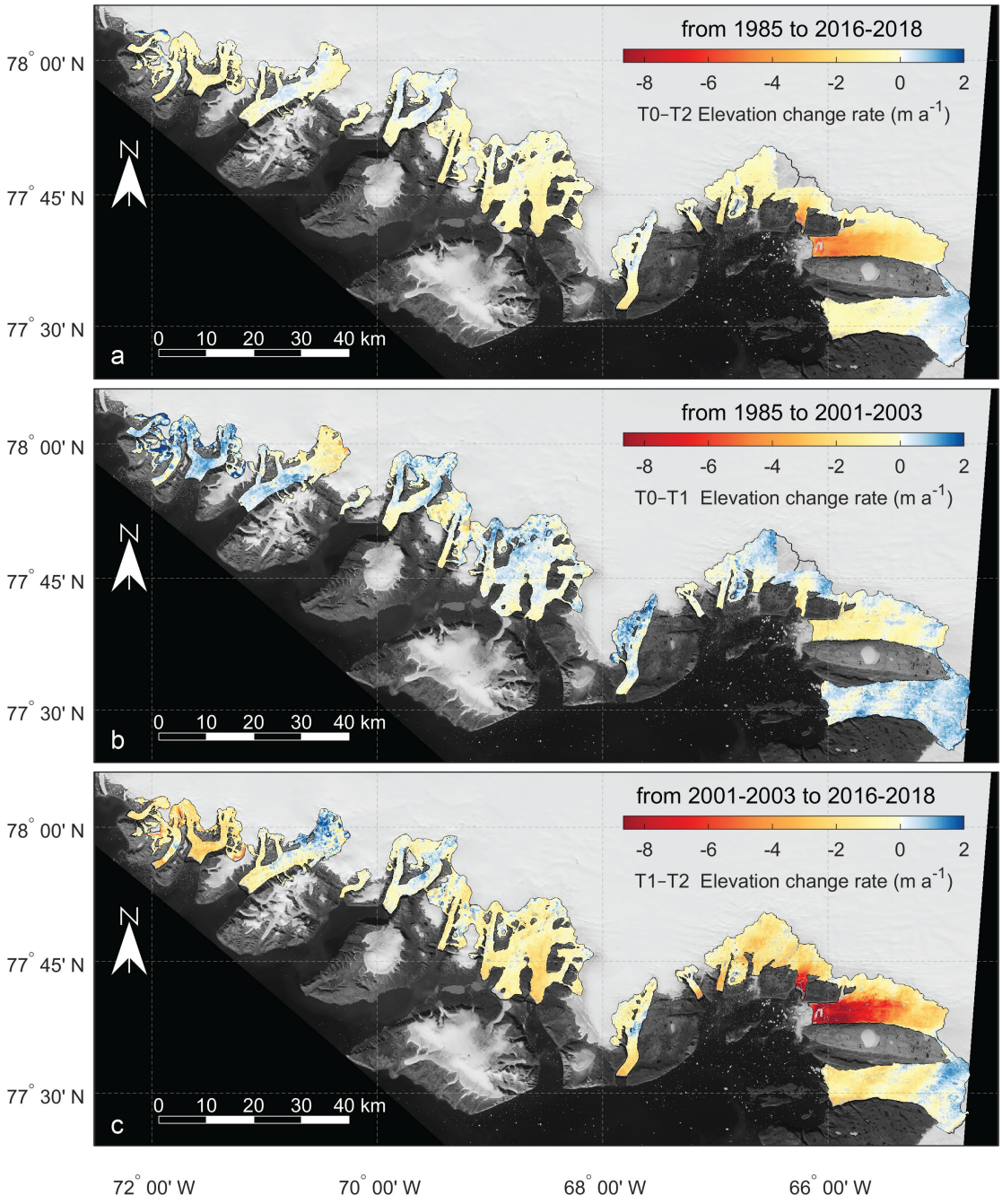

Figure 2.2 Glacier elevation changes during different periods

(a) T0–T2, (b) T0–T1, and (c) T1–T2. The background is a Landsat-8 panchromatic image taken in August 2016. The color scale is given for areas below < 850 m a.s.l., where elevation change was analyzed.

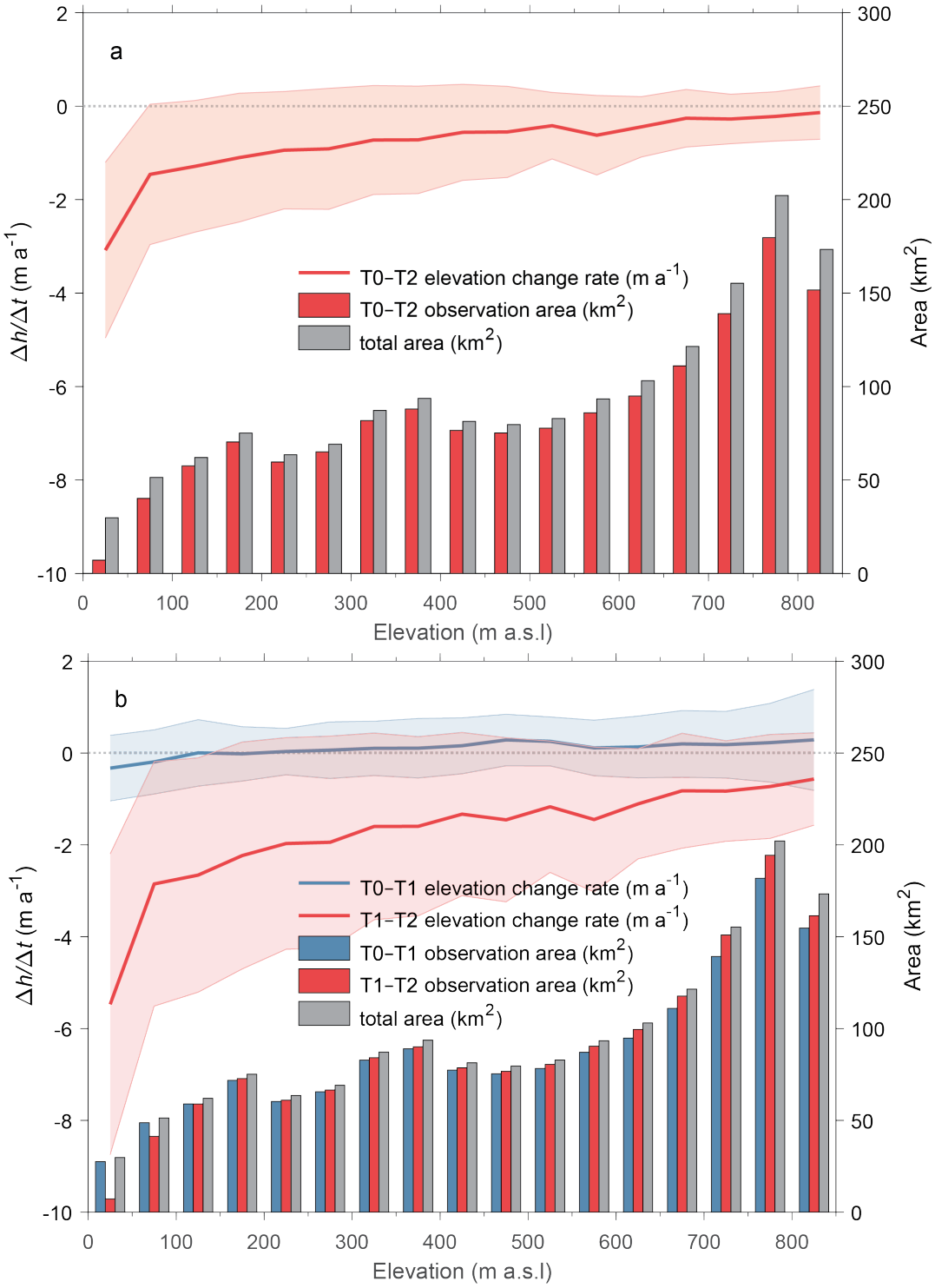

Figure 2.3 Rates of elevation change in different periods

Line plots are the rates of elevation changes averaged over the studied glaciers in the 50 m elevation bands in the periods of (a) T0–T2, (b) T0–T1, and T1–T2. Shaded areas represent standard deviations. Histograms show the glacier area hypsometry as it was in 2010 (grey) and the glacier areas covered by the analysis (blue and red).

Contrasting elevation change patterns were observed for the two subperiods, i.e. surface lowering accelerated from T0–T1 to T1–T2 over the entire elevation range (Fig. 2.3b). Elevation change was nearly zero or slightly positive from T0 to T1 (Fig. 2.2b), while strongly negative elevation change was observed from T1 to T2 (Fig. 2.2c). The mean elevation change rate for T0–T1 was 0.14 ± 0.17 m a^{-1} with an upglacier increasing trend (Fig. 2.3b). In contrast to the first period, clearly negative elevation change was detected during the second subperiod (T1–T2). The mean rate over the study area was −1.31 ± 0.20 m a^{-1} and the most rapid change was observed near the frontal areas (−5.47 m a^{-1} at 0–50 m) (Fig. 2.3b). Even in the elevation band 800–850 m, the glaciers experienced surface lowering at a rate of −0.57 m a^{-1}.

Surface lowering was slightly enhanced at the elevation band 550–600 m (Fig. 2.3). This trend is due to the altitudinal distribution of Tracy Glacier, the most rapidly thinning and the second largest among the studied glaciers. The surface area of this glacier accounts for 8.4% of the study area at 550–600 m, while it only accounts for 3.5 and 7.9% in the adjacent 500–550 and 600–650 m bands, respectively. Therefore, rapid elevation change of Tracy Glacier (−3.77 m a^{-1} at 550–600 m in T1–T2) affected the total mean thinning rate in the corresponding elevation range (−1.45m a^{-1}).

2.4.2 Individual glaciers

The elevation change showed significant variations among the glaciers (Table 2.2). Most of the glaciers exhibited no obvious change, or only a slight thickening during the period T0–T1. Obvious surface lowering was observed only in the frontal areas of Tracy, Farquhar, Sharp, and Sun Glaciers (Fig. 2.2b). The most significant surface lowering during this period was found below 600 m a.s.l. in Tracy and Farquhar Glaciers (Fig. 2.4b and 2.4c), which formed a common glacier tongue until it disintegrated in 2002 (Sakakibara and Sugiyama, 2018). Nevertheless, even in these regions, the magnitude of thinning in the period T0–T1 was less than 2 m a^{-1}.

Table 2.2 Mean elevation change for different glaciers

Mean elevation changes (m a^{-1}) are calculated during the three periods (T0–T2, T0–T1, T1–T2) on each glacier, as well as glacier groups in Inglefield Bredning (numbers in brackets indicate the results calculated without Tracy Glacier), Baffin Bay region, and all glaciers studied. The area of each glacier and glacier group is also shown in the table.

Glaciers/regions	Area (km^2)	Periods		
		T0–T1	T1–T2	T0–T2
Heilprin	287.10	0.50±0.16	−0.51±0.13	0.00±0.14
Tracy	222.93	−0.46±0.16	−3.91±0.13	−2.14±0.14
Farquhar	53.74	0.03±0.15	−2.91±0.18	−1.28±0.14
Melville	118.52	0.39±0.15	−1.73±0.38	−0.54±0.33
Sharp	41.28	−0.02±0.15	−1.22±0.38	−0.55±0.33
Hart	16.85	−0.12±0.15	−0.83±0.51	−0.38±0.27
Hubbard	80.69	0.46±0.14	−0.81±0.20	−0.18±0.27
Bowdoin	135.75	0.04±0.16	−1.11±0.14	−0.55±0.21
Sun	66.79	−0.26±0.16	−0.68±0.14	−0.46±0.21
Verhoeff	128.20	0.12±0.16	−0.14±0.14	−0.01±0.21
Meehan	12.53	−0.06±0.16	−0.54±0.11	−0.29±0.13
Morris Jesup	139.94	−0.24±0.25	−0.08±0.35	−0.15±0.43
Diebitsch	81.26	0.69±0.25	−1.83±0.35	−0.51±0.43
Bamse	28.66	0.71±0.25	−1.06±0.35	−0.14±0.43
Clements	39.93	0.64±0.25	−1.52±0.35	−0.40±0.43
Tugto	170.37	0.23±0.16	−0.83±0.14	−0.31±0.21
Inglefield	956.86	0.13±0.16	−1.74±0.19	−0.77±0.19
Bredning	(733.93)	(0.31±0.16)	(−1.07±0.21)	(−0.32±0.21)
Baffin Bay	497.31	0.13±0.21	−0.64±0.26	−0.23±0.34
Total	1624.54	0.14±0.17	−1.31±0.20	−0.55±0.24

The elevation change showed significant variations among the glaciers (Table 2.2). Most of the glaciers exhibited no obvious change, or only a slight thickening during the period T0–T1. Obvious surface lowering was observed only in the frontal areas of Tracy, Farquhar, Sharp, and Sun Glaciers (Fig. 2.2b). The most significant surface lowering during this period was found below 600 m a.s.l. in Tracy and Farquhar Glaciers (Fig. 2.4b and 2.4c), which formed a common glacier tongue until it disintegrated in 2002 (Sakakibara and Sugiyama, 2018). Nevertheless, even in these regions, the magnitude of thinning in the period T0–T1 was less than 2 m a^{-1}.

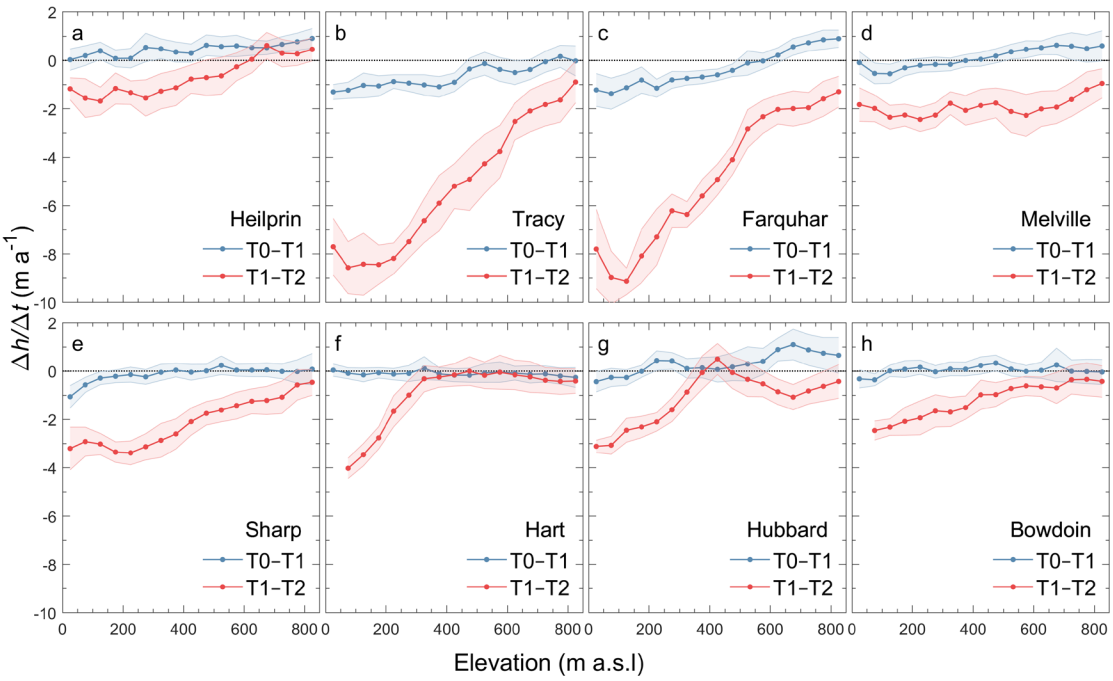

Figure 2.4 Elevation change rates on glaciers terminating in Inglefield Bredning Blue: periods T0–T; Red: periods T1–T2.

Spatial patterns of the elevation change in T1–T2 are significantly different from those in the previous period. All the glaciers experienced surface lowering at a rate substantially different for each glacier (Fig. 2.2c and Table 2.2). The thinning was particularly rapid at Tracy and Farquhar Glaciers, where the mean rates of the elevation change were −3.91 ± 0.13 and −2.91 ± 0.18 m a^{-1}, respectively. The rates near the calving front of these two glaciers reached −9 m a^{-1} (Fig. 2.4b and 2.4c). Heilprin Glacier thinned at a rate of −0.51 ± 0.13 m a^{-1}, which was ~60% slower than the mean of the glaciers studied. The magnitude increased towards the calving front, but did not exceed −1.5 m a^{-1} (Fig. 2.4a). Thinning rates of Morris Jesup and Verhoeff Glaciers (−0.08 ± 0.35 and −0.14 ± 0.14 m a^{-1}) were the two lowest among the glaciers studied during T1–T2 (Table 2.2). Interestingly, Morris Jesup Glacier showed contrasting altitudinal distribution patterns between the two subperiods (Fig. 2.5d). During T0–T1, the glacier thickened over the area below 550 m a.s.l., whereas thinning was observed above 550 m a.s.l. The thinning was more significant at the higher elevation, being enhanced from −0.27 m a^{-1} at 500–550 m a.s.l. to −1.12 m a^{-1} at 800–850 m a.s.l. During T1–T2, the glacier thinned and thickened below and above 600 m a.s.l.,

respectively. No clear altitudinal variation was found at Verhoeff Glacier during T0–T1 and T1–T2 (Fig. 2.5b), where elevation change over the last three decades was the smallest among the glaciers studied. The only land-terminating glacier, Tugto Glacier, showed a relatively small elevation change at rates of 0.23 ± 0.14m a^{-1} for T0–T1 and −0.83 ± 0.14 m a^{-1} for T1–T2. The latter corresponds to approximately 60% of the mean of the glaciers studied. No apparent dependence on altitude was observed in either subperiod for this glacier (Fig. 2.5h).

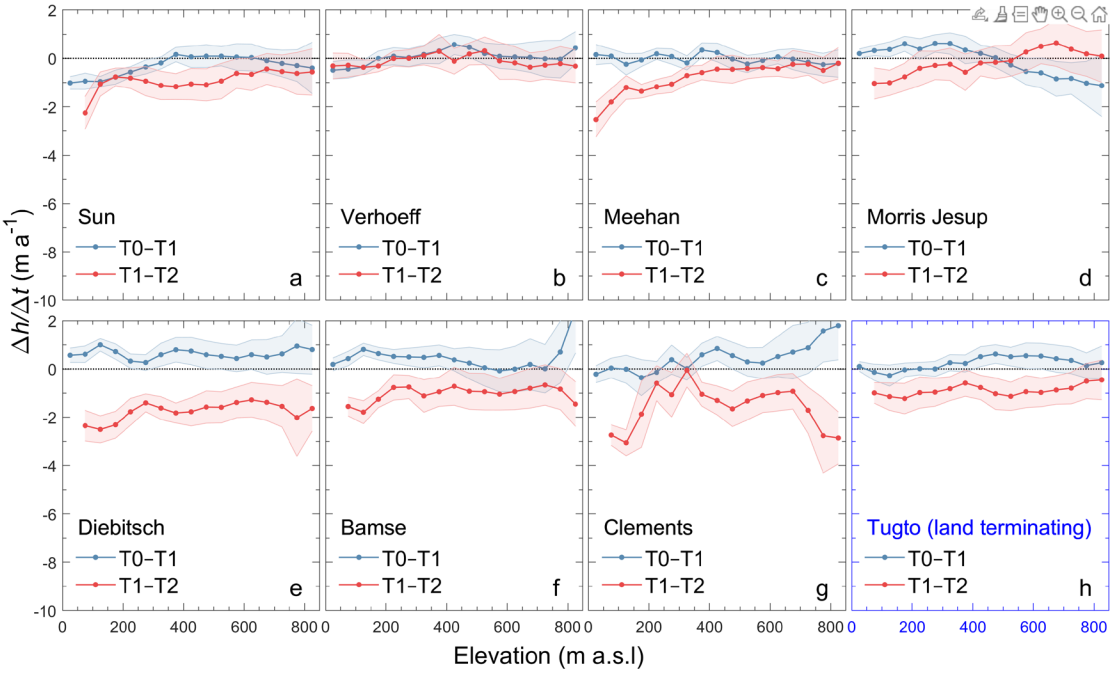

Figure 2.5 Same as Figure 2.4 but for glaciers terminating in Baffin Bay (Including the land-terminating Tugto Glacier highlighted in blue).

2.4.3 Regional variation

The magnitude of the thinning and its temporal patterns vary between the Baffin Bay and Inglefield Bredning regions (Fig. 2.2). To investigate regional patterns, thinning rates of glaciers terminating in Inglefield Bredning (Heilprin, Farquhar, Melville, Sharp, Hart, Hubbard, and Bowdoin) are compared with those terminating in Baffin Bay (Sun, Verhoeff, Meehan, Morris Jesup, Diebitsch, Clements, and Bamse) (Fig. 2.6). Tracy Glacier was excluded from this analysis, to avoid the influence of its much higher thinning rate.

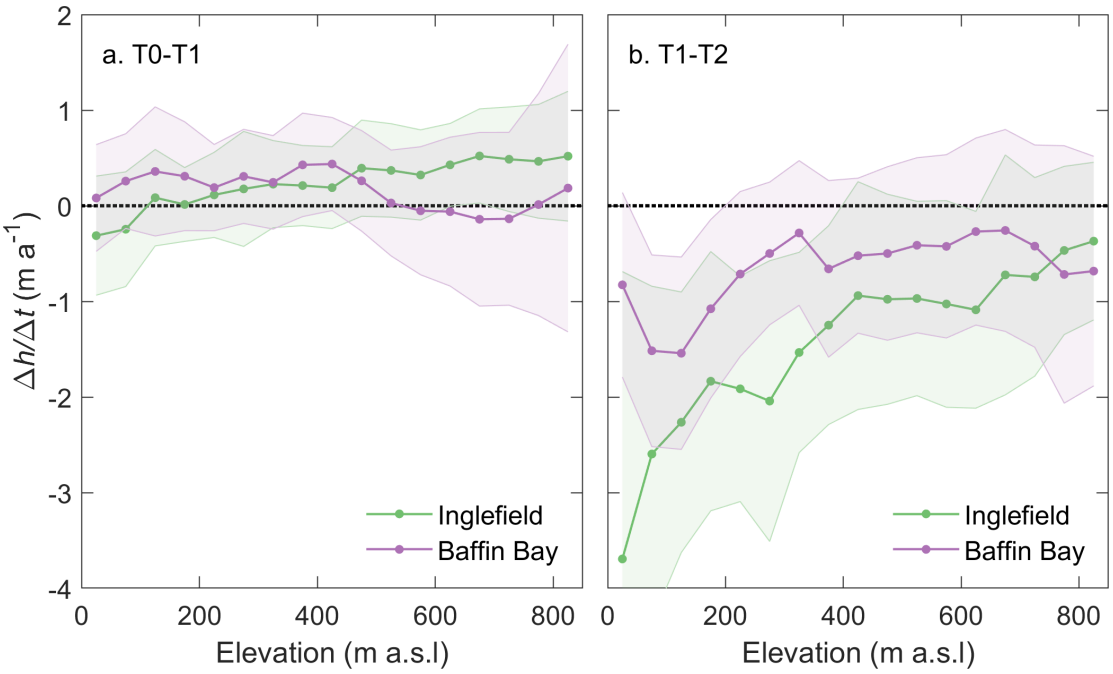

Figure 2.6 Rates of surface elevation change in different region
(a) T0–T1 and (b) T1–T2, averaged over the glaciers terminating in Baffin Bay (red) and in Inglefield Bredning (blue). Shaded areas represent the standard deviation.

During the period T0–T1, elevation changes averaged over the two regions were similar and measured approximately zero or slightly positive (Fig. 2.6a). Elevation changes in the Inglefield Bredning region gradually increased upglacier, showing thickening above 200 m a.s.l. The mean thickening rates below and above 500 m a.s.l. were 0.17 and 0.46 m a^{-1}, respectively. In the Baffin Bay region, glaciers slightly thickened below 500 m a.s.l. (0.28 m a^{-1}), whereas only minor changes occurred above 500 m a.s.l. (0.00 m a^{-1}) (Fig. 2.6a). In the period T1–T2, elevation changes were negative over the entire elevation range in the two regions (Fig. 2.6b). The magnitude of the thinning was ~70% greater in the Inglefield Bredning region (−1.07±0.21 m a^{-1}) than in the Baffin Bay region (−0.64±0.26 m a^{-1}), however, considering the relatively large uncertainty, the difference may not that significant, here I only want to show the stronger thinning were observed in Inglefield Bredning. The thinning was most accelerated near the front of the glaciers in the Inglefield Bredning region, which is represented by the change in the 0–50 m a.s.l. band from −0.31 m a^{-1} (T0–T1) to −3.69 m a^{-1} (T1–T2) (Fig. 2.6). In the Baffin Bay region, the most significant change from 0.36 m a^{-1} (T0–T1) to −1.54 m a^{-1}

(T1–T2) occurred at 100–150 m a.s.l.

2.4.4 Atmosphere and ocean temperature

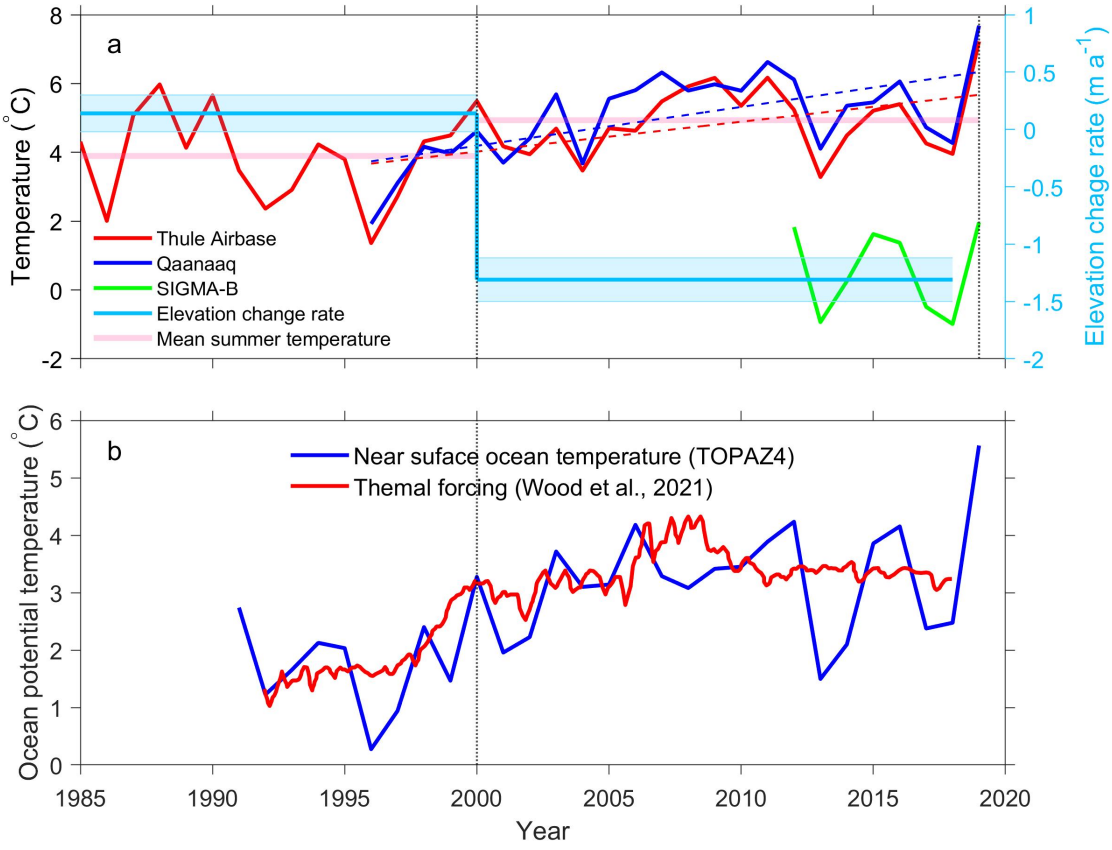

Figure 2.7 Atmospheric and oceanic temperature
(a) Summer mean temperature (June–August) at Thule Airbase (red), Qaanaaq (blue) and SIGMA-B (green). The magenta lines represent the mean summer temperature at Thule Airbase from 1985 to 2000 and from 2001 to 2019. The dashed lines are linear regression of temperature between 1996 and 2019 at Thule Airbase (red) and Qaanaaq (blue). The light blue line represents the mean glacier elevation change rate with the standard deviation shown by the shaded area. (b) Summer mean ocean temperature (blue) at a depth of 5 m, derived from TOPAZ4 Arctic Ocean reanalysis data in the area of 77–78° N and 66–72° W and ocean thermal forcing (average subsurface temperatures over the lower 60% of the water column, in red) near Inglefield Bredning (76.8–77.3° N, 71–73° W) (Wood et al., 2021).

Summer (June–August) mean temperatures at Qaanaaq, Thule Airbase and SIGMA-B are shown in Figure 2.7a. Recent warming trends are clear, as evidenced by the change in the mean summer temperature between the periods 1985–2000 and 2001–2018, from 3.9 to 4.8°C at Thule Airbase and from 3.6 to 5.4°C at Qaanaaq. Linear warming trends for the period 1996–2019 were 0.09°C a^{-1} ($p < 0.05$) at Thule Airbase and 0.11°C a^{-1}

($p < 0.005$) at Qaanaaq. The summer mean temperature at Qaanaaq was consistently above 5°C during the periods 2005–2012 and 2014–2016, which was rarely observed before 2000 (Fig. 7a). An unprecedented high temperature (7.7°C) was recorded in 2019. Even at 944 m a.s.l. (SIGMA-B on Qaanaaq Ice Cap), summer mean temperatures were above freezing in the years 2012, 2014–2016, and 2019.

Consistent with the atmospheric warming trend, near-surface ocean temperatures increased during the period of 1996–2012 at a rate of 0.18°C a^{-1} ($p < 0.001$) (Fig. 2.7b). The mean temperature for 2001–2018 (3.1°C) was 1.3°C warmer than the mean for 1991–2000. Moreover, the reconstruction of ocean thermal forcing near Inglefield Bredning demonstrated relatively stable temperatures during the period 1992–1997, rapid warming at a rate of 0.18°C a^{-1} from 1998 to 2007, although with a drop in temperature by 0.6°C from 2008 to 2017 (Fig. 2.7b) (Wood et al., 2021).

2.5 Discussion

2.5.1 Comparison with previous studies

Here, I compare my results with previously published estimates for glacier mass loss and elevation change in Greenland and adjacent areas. I converted the observed volume change to mass change using the ice density of 910 kg m^{-3}. The mass loss over the studied areas from T0–T2 was −0.81 ± 0.44 Gt a^{-1}, which corresponds to 0.5% of the total mass loss of the Greenland Ice Sheet (−150 Gt a^{-1}) from 1992 to 2018 (Shepherd et al., 2020). After 2000, the mass loss increased to −1.94 ± 0.15 Gt a^{-1} during T1–T2, accounting for 0.8% of the Greenland Ice Sheet mass change for 2005–2015 (Shepherd et al., 2020). On the western side of Baffin Bay, thinning rates of glaciers and ice caps on the Queen Elizabeth Islands during 2005/06–2012/14 were more than three times greater than those during 1995–2000. In this region, marine-terminating glaciers showed greater acceleration than those terminating on land, suggesting that an increase in ocean heat flux plays an important role in addition to atmospheric warming (Mortimer et al., 2018).

Elevation changes of Tracy Glacier from 2003 to 2007 was reported as −5.46 m a^{-1} at 600 m a.s.l. (Pritchard et al., 2009), which is higher than the rate I obtained for T1–T2 (−3.77 m a^{-1} at 550–600 m a.s.l.). The difference is potentially due to the shorter sampling period or the limited number of ICESat sampling sites analyzed in the previous study. More recent research showed thinning within 6 km from the front (approximately 0–400 m a.s.l.) at a rate of −9.9 m a^{-1} from 2016–2017, which is ~30% greater than my result in T1–T2 (−7.40 m a^{-1}) (Willis et al., 2018). Porter et al. (2014) reported that the thinning rate in the ablation zone doubled from −6 m a^{-1} in 2002–2010 to −12 m a^{-1} in 2011–2012 (Porter et al., 2014). Therefore, mass loss of Tracy Glacier appears to have increased in the 21st century.

2.5.2 Driving mechanism of the elevation change

In general, thinning of the glaciers accelerated from T0–T1 to T1–T2. However, the timing and magnitude of the acceleration showed substantial variation from glacier to glacier. Here, I discuss air temperature, ocean temperature, ice dynamics and fjord bathymetry as possible drivers of the spatiotemporal variability in the thinning rate.

(1) Atmospheric warming

A substantial rise in air temperature has been observed in Greenland since the mid-1990s (Box et al., 2009; Carr et al., 2013a; Mernild et al., 2011). The warming atmospheric conditions have enhanced surface melting (van den Broeke et al., 2009), resulting in a mass loss of −76 Gt a^{-1} over the Greenland ice sheet from 1992 to 2008 (Shepherd et al., 2020). Glacier thinning in my study area increased from 0.14 ± 0.16 m a^{-1} in T0–T1 to −1.31 ± 0.19 m a^{-1} in T1–T2. Temperatures at Thule Airbase and in Qaanaaq showed warming trends during these periods (Fig. 2.7a), suggesting the influence of atmospheric warming on the observed glacier changes. Temperature sensitivity of the mass loss is calculated as 0.61 m a^{-1} K^{-1} from the elevation change rate from T0–T2 and temperature increase during the same period. This number is slightly greater than 0.48 m a^{-1} K^{-1}, as reported in the Canadian Arctic Archipelago (Gardner et al., 2011). The sensitivity is more than double those estimated for Arctic

glaciers and ice caps, based only on surface mass balance (Woul and Hock, 2005), indicating that the observed mass loss was not entirely due to atmospheric warming.

In addition to the long-term warming trend, unprecedented melt events due to exceptional atmospheric circulation patterns have been reported in Greenland (e.g., Nghiem et al., 2012; Hanna et al., 2014; Tedesco and Fettweis, 2020). The large amount of meltwater generated during melt events either forms supraglacial lakes and streams, or is delivered into the ice-bed interface through moulins and crevasses (Chu, 2014). The supraglacial lakes and streams enhance ablation because of their lower albedo relative to the surrounding ice (Tedesco et al., 2012). Moreover, the increased input of meltwater into an inefficient subglacial hydrological system elevates basal water pressure and enhances basal sliding, resulting in glacier acceleration and dynamic thinning (Zwally et al., 2002; Bartholomew et al., 2010). Furthermore, the increased volume of subglacial discharge potentially enhances submarine melting because the discharge activates fjord circulations and facilitates more efficient oceanic heat transport to the glacier (Motyka et al., 2013; Straneo et al., 2013b).

(2) Oceanic forcing

Oceanic forcing is recognized as a key control on Greenlandic outlet glaciers. Ocean warming drives not only glacier retreat (Straneo and Heimbach, 2013a; Wood et al., 2021; Fahrner et al., 2021), but also glacier acceleration (Holland et al., 2008; Howat et al., 2008) and thinning (Thomas et al., 2009; Felikson et al., 2017) through ice-ocean interaction at the glacier front. Intrusion of warming Atlantic waters is considered to be the driver of recently enhanced submarine melting of Greenland's outlet glaciers along the western coast (Straneo et al., 2013b). More rapid retreat, acceleration, and thinning were observed at glaciers located in deep fjords, which are more exposed to deep water warming (Rignot et al., 2010; Wood et al., 2018, 2021).

Wood et al. (2021) investigated the influence of recent ocean warming on submarine melting at some of the glaciers in my study site. During the ~2°C increase in the ocean thermal forcing from 1998 to 2007 (Fig. 2.7b), an approximately fourfold increase was

estimated for the upper bound of the melt rates at Tracy, Heilprin, and Bowdoin Glaciers (see Table S1 in Wood et al., 2021). These glaciers terminate in deep fjords in Inglefield Bredning (150–400 m deep), whereas no significant change was reported for those terminating in shallower fjords in the Baffin Bay region (e.g. Diebitsch, Verhoeff, and Morris Jesup glaciers) (Wood et al., 2021). Greater influence of ocean warming is a possible interpretation for the regional variations in the glacier thinning rate, since enhanced submarine melting causes persistent glacier retreat, acceleration and dynamic thinning, as observed at the glaciers in Inglefield Bredning (Sakakibara and Sugiyama., 2020).

In addition to the warming in the deep layer, the TOPAZ4 data showed an increase in near-surface water temperatures during the period 1996–2012 (Fig. 2.7b), suggesting its influence on ice front melting and calving. Near-surface ocean warming enhances melting at or below the waterline, resulting in an unstable ice front and an increase in calving rates (Benn et al., 2007). In some cases, enhanced calving can trigger initial retreat of a glacier from a bedrock bump, which leads to the destabilization of the glacier terminus, ice-flow acceleration, and dynamic thinning (Felikson et al., 2017, Porter et al., 2018).

(3) Ice dynamics

Recently observed rapid thinning of Greenlandic marine-terminating glaciers cannot be attributed to increasing surface melt alone. Rather, a significant portion of the thinning is due to ice dynamics driven by atmospheric and oceanic forcing. Dynamic thinning associated with ice acceleration has been observed extensively in the coastal areas of Greenland (e.g., Abdalati et al., 2001; Krabill et al., 2004; Thomas et al., 2009), and most prominently in the southeastern and northwestern regions (Csatho et al., 2014; Pritchard et al., 2009).

The magnitude of the glacier thinning obtained in this study is substantially greater than those reported from peripheral glaciers and ice caps in the region, most of which are terminating on land. Elevation changes of glaciers and ice caps in northwestern

Greenland were reported to be −0.54 m a^{-1} in the period 2003–2009 (Gardner et al., 2013) and −0.60 m a^{-1} in the period 2003–2008 (Bolch et al., 2013). The thinning rate of six ice caps in the Qaanaaq region was −1.1 ± 0.1 m a^{-1} for the period 2006–2010 (Saito et al., 2016). These thinning rates are less than the mean rate obtained in this study for the period 2001–2018 (−1.31 ± 0.19 m a^{-1}), indicating the significance of dynamic thinning at marine-terminating glaciers in northwestern Greenland.

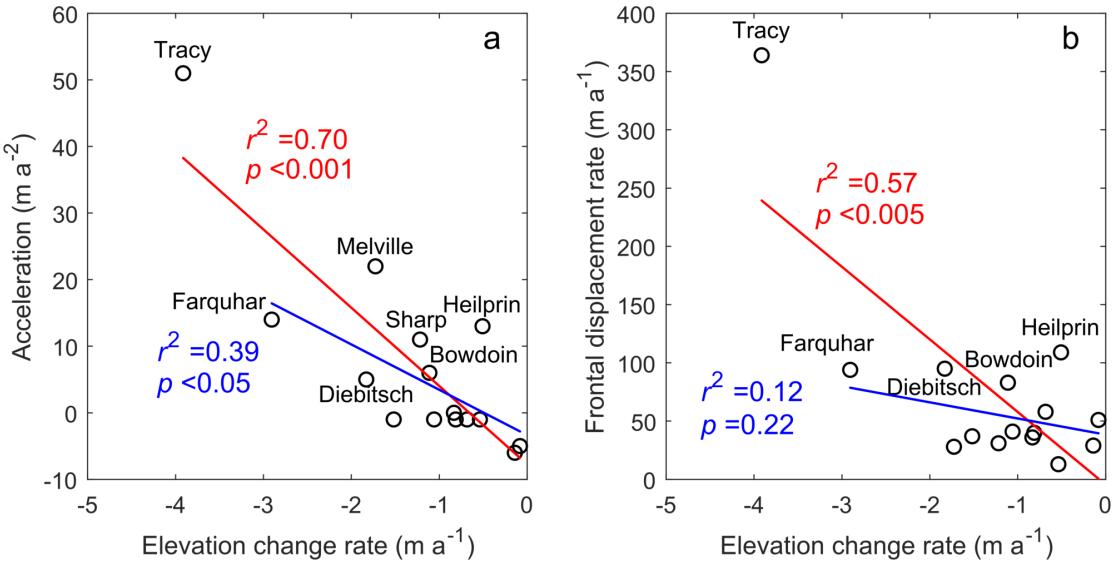

Figure 2.8 Relationship between elevation change and acceleration/retreat
Scatter plots of (a) flow acceleration and (b) frontal displacement rate vs surface elevation change rate obtained at each studied glacier from 2000 to 2018. Red and blue lines are linear regressions of the data including or excluding Tracy Glacier, respectively. Frontal displacement rate and flow acceleration between 2000 and 2014 are taken from Sakakibara and Sugiyama (2018).

To investigate a link between the thinning, acceleration and retreat in the Prudhoe Land region, I used ice speeds and frontal displacement rates of the studied glaciers reported for the period between 2000 and 2014 (Sakakibara and Sugiyama, 2018). As represented by Tracy Glacier, rapidly thinning glaciers are characterized by greater retreat and acceleration (Fig. 2.8). The correlation between the elevation change and acceleration is significant ($r^2 = 0.70, p < 0.001$) (Fig. 2.8a). A relationship is still evident even if Tracy Glacier is excluded from the analysis, although the correlation coefficient decreases ($r^2 = 0.37$, $p < 0.05$). Correlation is also observed between the elevation change and retreat rate ($r^2 = 0.57, p < 0.005$), but it is insignificant when Tracy Glacier

is excluded ($r^2 = 0.12$, $p = 0.22$) (Fig. 2.8b).

Observations at Bowdoin Glacier suggested such a link between glacier mass loss and ice dynamics. Sugiyama et al. (2015) observed a two-fold acceleration near the glacier front from 1999 to 2003, which coincided with a small glacier retreat. The acceleration interrupted relatively stable glacier conditions since the 1980s, leading to rapid thinning and retreat since 2008. The thinning rate of Bowdoin Glacier from 2007 to 2010 was approximately 50% greater than that of the adjacent land-terminating Tugto Glacier. The rapid thinning was thus attributed to longitudinal stretching caused by acceleration (Tsutaki et al., 2016). Similar connections between acceleration and thinning were also suggested for other glaciers in Inglefield Bredning, i.e. Heilprin, Tracy, Farquhar, and Diebitsch Glaciers, based on data obtained between 2000 and 2014 (Sakakibara and Sugiyama, 2018). Thinning and acceleration are often associated with glacier front retreat. My data shows that the magnitude of acceleration has a stronger correlation with surface elevation change rate than does the magnitude of retreat (Fig. 2.8). Therefore, ice acceleration is more strongly linked with the thinning rates of the glaciers in the Prudhoe Land region during the period T1–T2.

The intriguing elevation change pattern observed at Morris Jesup Glacier is another example of glacier change driven by ice dynamics. Mouginot et al. (2019) reported a more than two-fold increase in the solid ice discharge of this glacier from 1975 to 1990 (from 0.15 to 0.35 Gt a^{-1}), which corresponds to the thinning (thickening) in the upper (lower) reaches during T0–T1 (Fig. 2.5d). Presumably, rapid ice transport resulted in the thickening downglacier, which was followed by a 5 m a^{-2} glacier decerelation (Sakakibara and Sugiyama, 2018) and thickening (thinning) in the upper (lower) reaches during T1–T2 (Fig. 2.5d). This observation indicates a long-lived surge event similar to that which has been documented at Hagen Bræ (Solgaard et al., 2020) and Storstrømmen (Mouginot et al., 2018).

Glaciers terminate in relatively narrow fjords (1.2–2.5 km wide), including Bamse, Cements, Meehan, Sun, Hubbard, and Hart Glaciers showed a stable or slightly

decreasing trend in the ice speed (Fig. 2.8a) (Sakakibara and Sugiyama, 2018), while my data indicate ice thinning during T1–T2 (Fig. 2.4 and 2.5). It is likely that ice dynamics of these glaciers were relatively insensitive to frontal retreat and decrease in basal drag after thinning because driving stress is more supported by lateral drag (Cuffey and Paterson., 2010). These glaciers decelerated under a greater influence of reduction in the driving stress, while the glaciers thinned by increasingly negative mass balance rather than changes in glacier dynamics.

(4) Fjord bathymetry

Fjord bathymetry is critically important for ice dynamics near the glacier front (e.g., Enderlin et al., 2013; Sakakibara and Sugiyama, 2018). It also affects frontal ablation because fjord depth controls the access of the relatively warm deep ocean water to the ice front (Holland et al., 2008; Porter et al., 2014). Among the glaciers studied, the changes observed in the neighboring Tracy and Heilprin Glaciers have varied greatly in terms of their front position, flow speed, and surface elevation since the 2000s (Moon et al., 2012; Rignot and Kanagaratnam, 2006). Tracy Glacier has experienced more rapid retreat, speedup, and surface lowering than Heilprin Glacier (Porter et al., 2014; Pritchard et al., 2009; Sakakibara and Sugiyama, 2018; Willis et al., 2018). Porter et al. (2014) suggested that Tracy Glacier is more vulnerable to changes in the ocean because of its deeper grounding line (> 600 m), compared to Heilprin Glacier (~350 m), causing its ice front to be more exposed to warm water at depth. To assess the influence of fjord bathymetry on glacier thinning, I investigated the basal topography from the BedMachine v3 product (Morlighem et al., 2017) (Fig. 2.9). The fjords on the Baffin Bay side are shallower than those belonging to Inglefield Bredning, which generally exceed several hundred meters in depth. Ocean temperature data from Bowdoin Fjord indicated that a depth below ~200 m is occupied by relatively warm Atlantic water (Kanna et al., 2018; Ohashi et al., 2020). Therefore, more rapid glacier thinning in the Inglefield Bredning region is most likely affected by greater exposure to oceanic heat. This situation contrasts to that on the western side of Baffin Bay. Cook et al. (2019)

studied recent frontal variations of marine-terminating glaciers in the Canadian Arctic Archipelago, namely Queen Elizabeth, Baffin and Bylot Islands. They concluded that elevated atmospheric temperature was the primary driver of glacier change, and that the influence of deep ocean water temperature was insignificant because the fjords are shallower than those along the western coast of Greenland and deep ocean water was not able to access the glacier front (Cook et al., 2019).

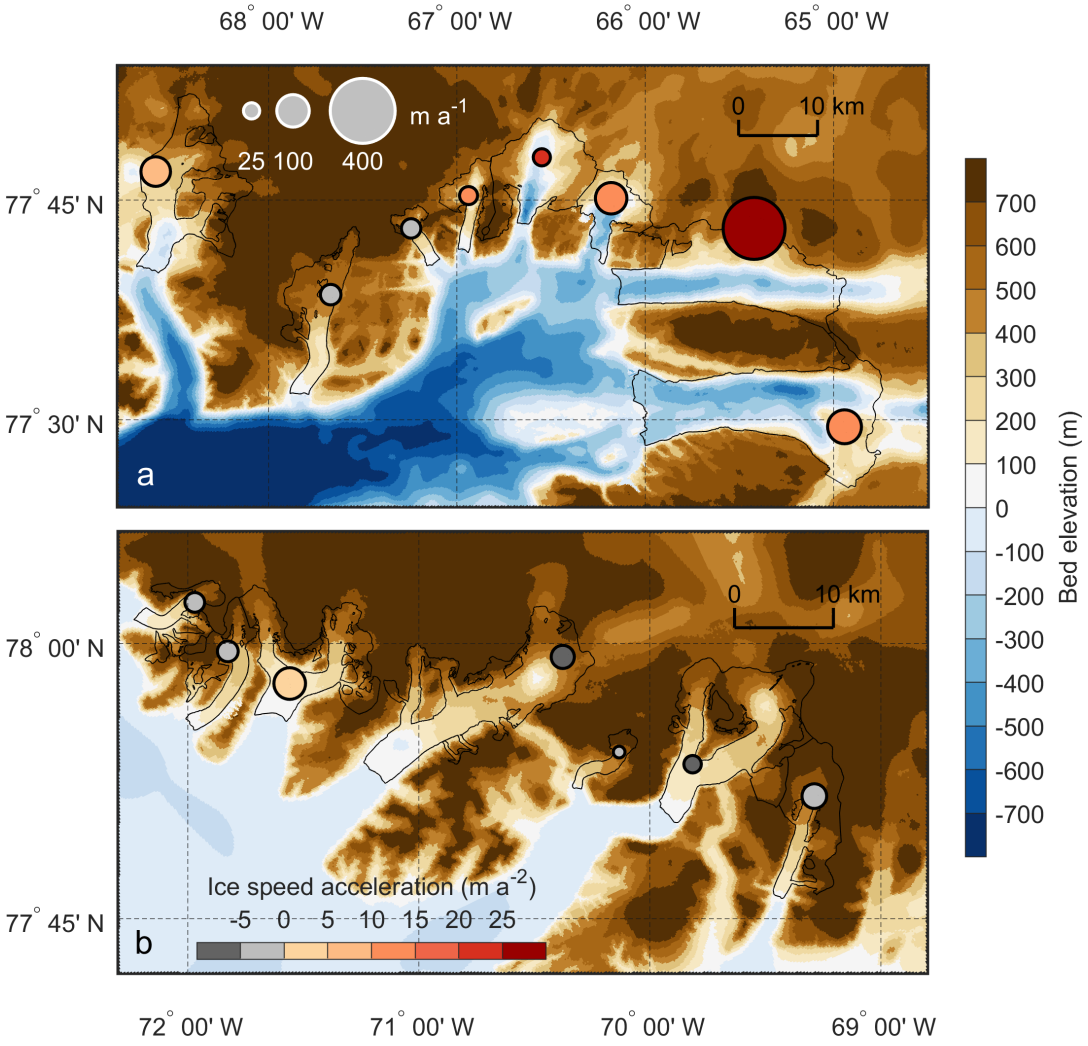

Figure 2.9 Basal topography in the study site
Basal topography from the BedMachine v3 product (Morlighem et al., 2017) in (a) the Inglefield Bredning region and (b) the Baffin Bay region. The black curves indicate the glacier areas studied. The area and color of the circle indicate the frontal displacement rate and flow acceleration of each glacier between 2000 and 2014 (Sakakibara and Sugiyama, 2018).

In addition to the role of fjord depth in ocean heat transfer, glaciers terminating in deep fjords are more subject to the influence of buoyancy when ice thins close to flotation.

Although the glaciers along Inglefield Bredning are grounded, Heilprin, Tracy, Farquhar, and Bowdoin Glaciers are near flotation condition (Sugiyama et al., 2015; Sakakibara and Sugiyama, 2018). Therefore, even a small perturbation in ice thickness or front position has a significant impact on the stress balance and stability of the terminus region (Benn et al., 2007). Due to the ice's exposure to heat in the deep ocean, as well as the greater susceptibility in the stress balance, I hypothesize that deep glacier bed geometries have an effect on the rapid thinning that has been observed.

2.6 Conclusions

In this study, I measured the glacier surface elevation change of 16 outlet glaciers along the coast of Prudhoe Land in northwestern Greenland. The measurements were taken from 1985 to 2018 using ASTER-VA DEM and the recently released AeroDEM. All the glaciers studied experienced surface lowering between 1985 to 2018 at a mean rate of -0.55 ± 0.22 m a^{-1}. The elevation change greatly accelerated after the 2000s. I detected a slight thickening (0.14 ± 0.16 m a^{-1}) prior to 2000, whereas substantial thinning (-1.31 ± 0.19 m a^{-1}) was observed during the period 2000–2018. Of the glaciers studied, Tracy and Farquhar Glaciers located in Inglefield Bredning thinned most rapidly, at a rate exceeding -9 m a^{-1} in the period 2000–2018.

Summer air temperatures have shown a warming trend from 1996 to 2019, indicating that enhanced surface melting is an important driver of glacier mass loss. Nevertheless, the acceleration of thinning that has been observed cannot be attributed to atmospheric warming alone. Deep ocean temperatures showed a warming trend between 1998 and 2007, which was potentially the driving force behind the rapid thinning and retreat of the glaciers located in deep fjords after the year 2000. Relatively deep fjords increase the exposure of the ice front to deep warm ocean water, which might have amplified the impact of deep ocean warming on the glaciers terminating in Inglefield Bredning. Near surface ocean temperature showed a similar warming trend to that of the atmosphere, suggesting a possible influence on the glacier change. There was a

significant correlation between the rate of change in glacier elevation and flow acceleration, suggesting the importance of dynamic thinning in the surface lowering of the glaciers studied. I also identified signs of a surge event on the elevation change pattern of Morris Jesup Glacier. Therefore, I conclude that the recent thinning of the glaciers along the Prudhoe Land region was generally controlled by atmospheric and oceanic conditions. In addition to the general trend, the response of individual glaciers to the atmospheric/oceanic forcing was modified by ice dynamics and fjord bathymetry.

2.7 Appendix

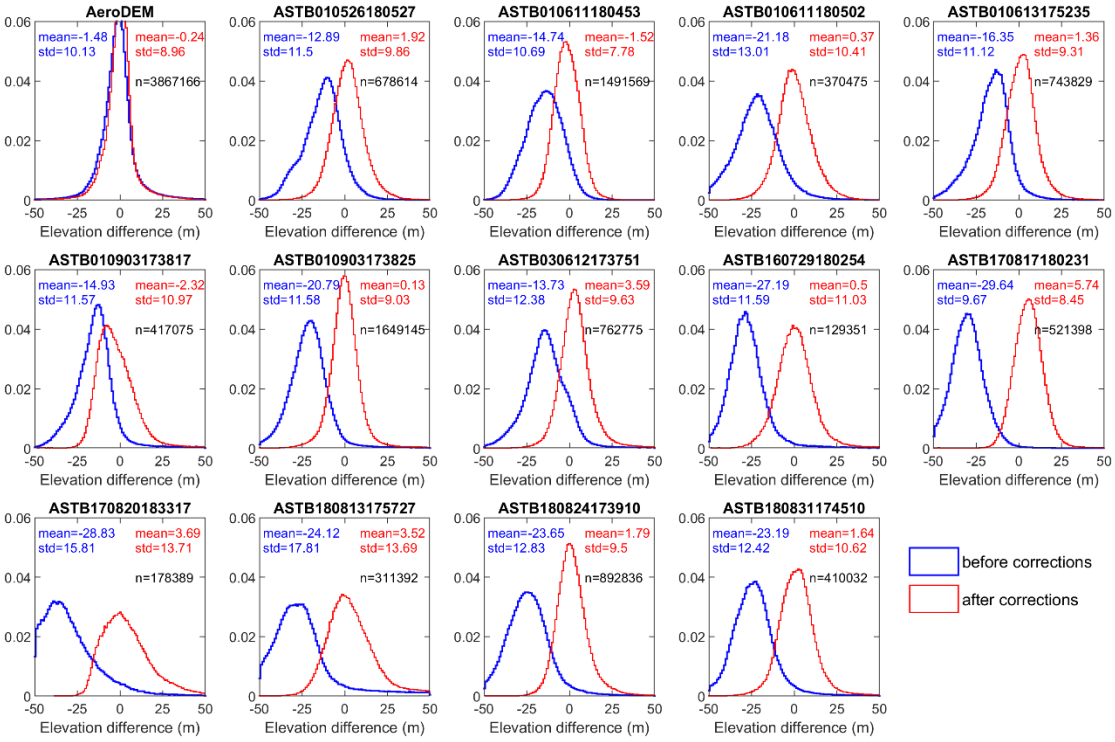

Figure 2.10 Elevation differences of the DEMs used in this study against GIMP DEM over ice-free areas

Title of each subplot indicates the DEM listed in Table 1. The blue and red curves/texts show histograms/statistics before and after the corrections. The mean elevation differences, standard deviation, and number of corrected pixels are given in each plot.

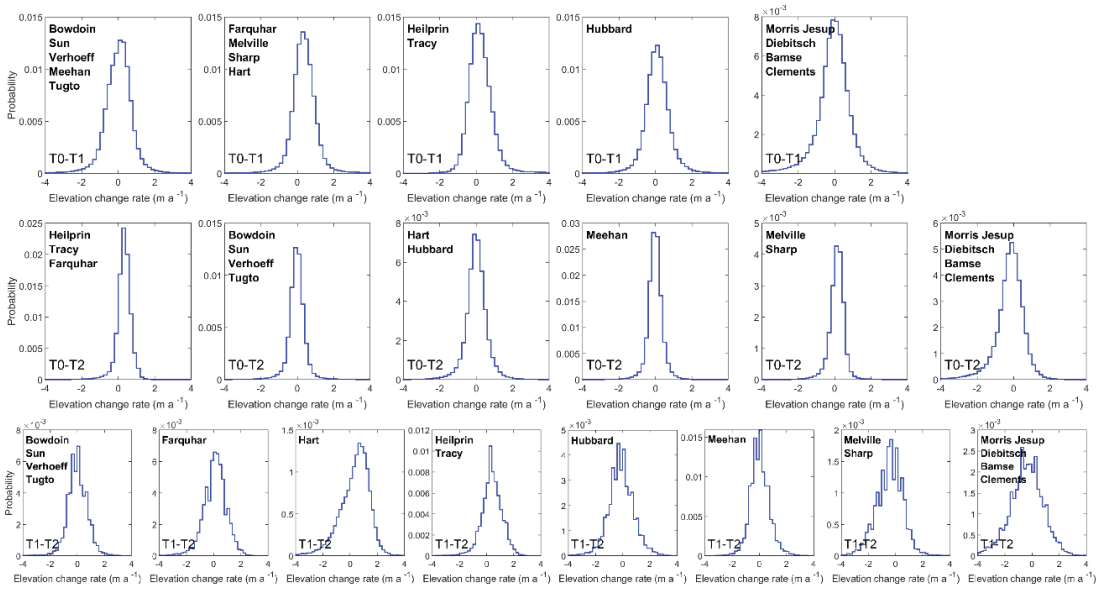

Figure 2.11 Histograms of the elevation change rates on the ice-free area near each glacier during each period

Corresponding glaciers and periods are given in each plot.

Chapter 3
Supraglacial lakes evolution on Tracy and Heilprin Glaciers from 2014 to 2021, northwestern Greenland

3.1 Introduction

Meltwater runoff from the Greenland ice sheet substantially increased in the recent two decades (Slater et al., 2021; Tedstone and Machguth, 2022), which was accompanied by the expansion of runoff area by 29% between 1985 and 2020 (Tedstone and Machguth, 2022). Except for the part that directly flows into the subglacial system through the crevasses or moulins, meltwater usually accumulates in surface topographic depressions within the ablation zone, forming supraglacial lakes (SGLs) during the melt season (Echelmeyer et al., 1991). Generally, the SGLs influence the ice sheet mass loss in two ways. First, lake enhance surface melting by 100–170% relative to the surrounding bare ice area due to the lower albedo (Lüthje and et al, 2006; Tedesco et al, 2012). Second, the rapid lakewater drainage event may cause ice flow acceleration due to elevated basal water pressure and reduced basal friction (Chudley et al., 2019; Das et al., 2008; Doyle et al., 2013; Stevens et al., 2015).

The lake development is mainly controlled by topography, climate, and glaciological-related factors. Given sufficient meltwater is produced in the melt season, SGLs location is foremostly controlled by the surface topography (Lüthje et al., 2006). Since the surface topography is sometimes a reflection of the bed geometry, the position of lakes on the ice surface is therefore largely controlled by the underlying bedrock topography (Lampkin and Vanderberg, 2011). Numerous small lakes tend to cluster in the near-terminus low elevation area; however, relatively large lakes tend to reoccur in the same location annually at high elevations (~1000–1200 m) and are less clustered. In more inland areas (above ~1200 m), lakes are sparse and poorly developed (Lampkin, 2011; Liang et al., 2012). The surface depressions provide potential locations for lake development, while lake ponding is controlled by air temperature. the formation of

lakes shows seasonal progress from lower elevations to higher elevations as the temperature increases (Chu, 2014). Under the currently warming Arctic climate, the lake development is likely to migrate to higher elevations where surface slopes are small and ice speeds are slow (Leeson et al., 2015; Ignéczi et al., 2016). Therefore, investigating the lake evolution and drainage is crucial for assessing the influence of SGLs on the Greenland peripheral glaciers and the impact on surface mass balance in the GrIS.

At present, the methods for tracking SGLs from optical imagery can be generally categorized into two types: threshold-based method (e.g. Fitzpatrick et al., 2014; Williamson et al., 2018; Moussavi et al., 2020; Turton et al., 2021) and machine learning (ML) method (e.g. Dirscherl et al., 2020; Halberstadt et al., 2020; Dell et al., 2021; Hu et al.,2022). For the threshold-based mapping, water bodies were identified where pixels satisfied a certain condition (exceed or less than a certain threshold) in spectral bands or spectral indices. The Normalized Difference Water Index adapted for ice (NDWIice), which is based on exceedance of an empirically selected red/blue reflectance threshold (typically > 0.2–0.5), is the most widely used spectral indices for lake identification (e.g. Fitzpatrick et al., 2014; Williamson et al., 2018). However, the solely NDWI-based approach sometimes brings about misclassification with cloud cover, cloud shadows, and other spectrally similar classes such as slush, blue ice, shaded rocks, and shaded snow. To avoid the misclassification, additional thresholds have been applied to distinguish these water-like features. Moussavi et al. (2020) employed Normalized Difference Snow Index (NDSI), ratio of thermal infrared band and blue band, difference between blue and green band, green and red band, and other band thresholds. In addition to NDWI, the introduction of NDSI lead a successfully mapping of SGLs on pan-Antarctic scale with fewer misclassification errors (Moussavi et al., 2020). And the multiple threshold approach has been widely used in the subsequent SGLs research (e.g. Spergel et al., 2021; Tuckett et al., 2021; Arthur et al., 2022). However, the threshold method may work not well when solving large temporal

and spatial SGL problems because the thresholds may change in different location and season. Thus, the threshold method lacks transferability due to the influence of different background environments (Dell et al., 2021). In recent years, the ML method has been applied in the SGLs studies. This method not only substantially reduces misclassification (Dirscherl et al., 2020; Halberstadt et al., 2020) but also has a potential to distinguish slush (Dell et al., 2021). Because the ML method utilizes greater amount of spectral information than the threshold method, it has an ability to determine the most important spectral information for make classification decisions automatically. While the previously reported ML-based SGL studies are mainly conducted in Antarctic ice shelves (e.g. Dirscherl et al., 2020; Halberstadt et al., 2020; Dell et al., 2021). Although several studies focused on pan-Greenland (Hu et al., 2022) and southwest Greenland (Yuan et al., 2020), temporal scales of the studies are relatively short and lacks research on seasonal change.

In this study, I implement a supervised machine learning methodology for SGL identification in Google Earth Engine (GEE), creating an automatic method for mapping SGLs over two major marine-terminating glaciers (Tracy and Heilprin Glaciers) in Inglefield Bredning, northwestern Greenland. I use a combination of Sentinel-2 and Landsat 8 imagery, which enable us to generate a high-temporal resolution (sub-weekly) record to better understand the lake evolution in the Greenland marine-terminating glaciers. By the multi-year SGL extent record, I present results showing the distribution of SGLs over the study glaciers and aim to analyze the intra-annual and inter-annual evolution of SGLs in the study region. In addition to the lake analyses, I compare my results with glaciological and climatic datasets, to explore the potential factors controlling the SGL formation and distribution on the marine-terminating glacier in order to improve my understanding of the feedback between meltwater generation and glacier dynamics.

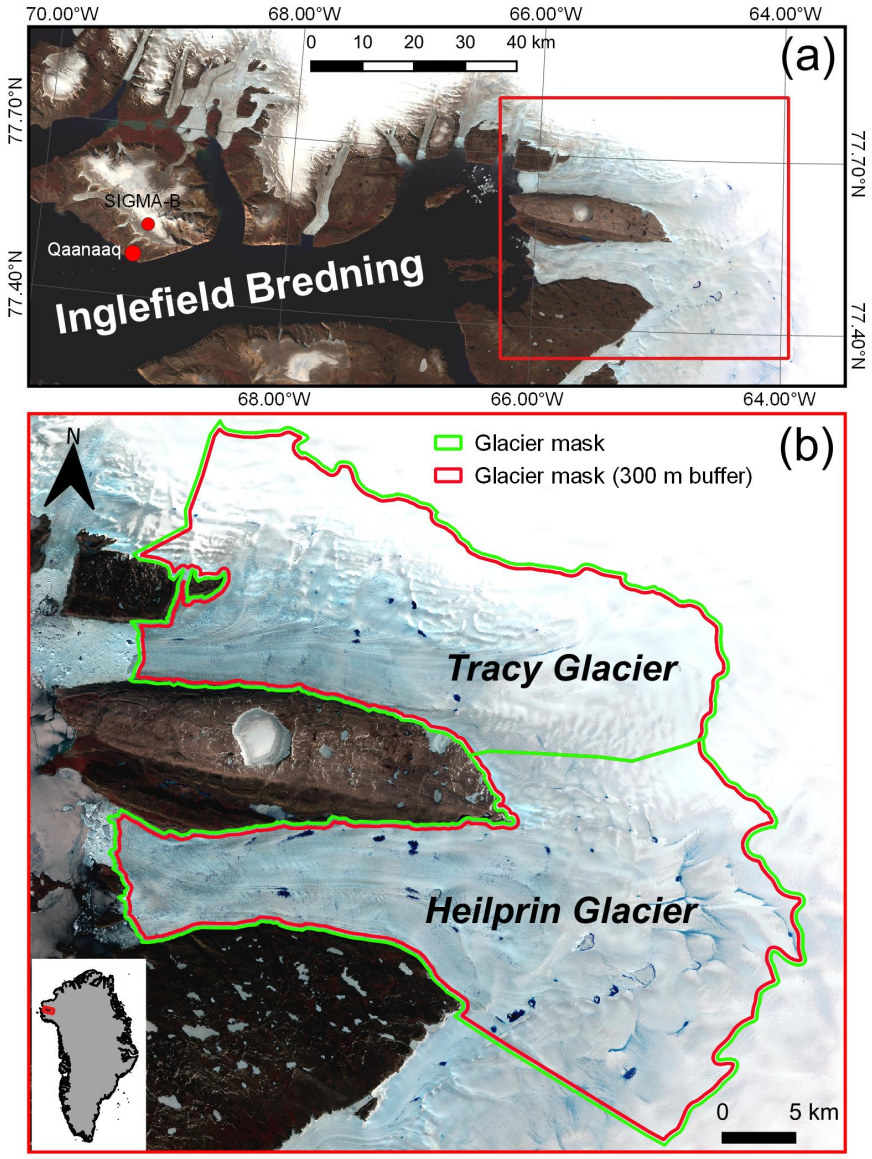

Figure 3.1 Study site
(a) Overview of the glaciers studied and surrounding area. The background is a mosaicked Sentinel-2 image acquired during July–August 2020. The red rectangle corresponds to the extent of the panel (b). (b) Details of Tracy and Heilprin Glacier. The red and green boundaries are the glacier mask described in 3.1. The background is a Sentinel-2 image acquired on 27 June 2020.

3.2 Study site

Tracy and Heilprin Glaciers are the largest two glaciers that terminate in Inglefield Bredning, northwestern Greenland (Fig. 3.1). The widths of the glaciers near the front in 2020 are 4.1 and 8.1 km, respectively. These two glaciers are only separated by a ~10

km-wide bedrock ridge, thus environmental controls affecting the glaciers are assumed to be similar (Porter et al., 2014; Willis et al., 2018). However, remarkably different patterns were observed in the changes of terminal positions, ice speed, and surface elevation between these two glaciers. Since 1892, Tracy Glacier has retreated by more than 15 km, but the retreat of Heilprin Glacier during the same period was smaller than 4 km (Dawes and Van As, 2010). From 1999 to 2014, the total retreat distance of Tracy and Heilprin Glaciers were 5.7 and 2 km, respectively (Sakakibara and Sugiyama, 2018). Both of the two glaciers are thinned after 2000. Thinning rate of Tracy Glacier between 2001 and 2018 was 3.91 m a^{-1}, while only 0.51 m a^{-1} for Heilprin Glacier (Wang et al., 2021). The difference in thinning was the most significant near the terminus. Surface lowering of 9.9 m was observed near the front of Tracy Glacier from 2016 to 2017, which is five times larger than that of Heilprin Glacier (1.9 m) during the same period (Willis et al., 2018). Meanwhile, ice speeds of both glaciers were accelerated during 2000–2014, but the acceleration in Tracy Glacier (51 m a^{-2}) was almost four times greater than that in Heilprin Glacier (13 m a^{-2}) (Sakakibara and Sugiyama, 2018). The significantly different behaviors of the two glaciers have been attributed to the deeper grounding line of Tracy Glacier, which makes the glacier front more exposed to deep warm water and subjected to stronger submarine melting (Porter et al., 2014; Wang et al., 2021; Willis et al., 2018).

3.3 Data and methods

3.3.1 Glacier masks

Considering the distribution of supraglacial lakes and the coverage of satellite images, the analysis in this study was carried out within the glacier mask shown in Figure 3.1b. The glacier mask is defined as follows: (1) extracting glacier basins of Heilprin and Tracy Glacier from Glacier catchments/basins for the GrIS (Mouginot and Rignot, 2019); (2) choosing the area with elevation lower than 1200 m a.s.l. based on ArcticDEM Mosaic (Porter et al., 2018) within the extracted glacier basin in (1); (3)

revising the glacier boundaries using Sentinel-2 images taken in late August 2020, then I generated the glacier mask as indicated by green curves in Figure 3.1b; (4) to avoid the influence of seasonal glacier boundary variations, I made a red glacier mask (Fig. 3.1b) which have a 300 m buffer inside the green glacier mask. This relatively conservative glacier mask with a 300 m buffer would not cause the information loss of supraglacial lakes because supraglacial lakes are rarely appeared on the edge of my research glaciers after inspecting the optical images.

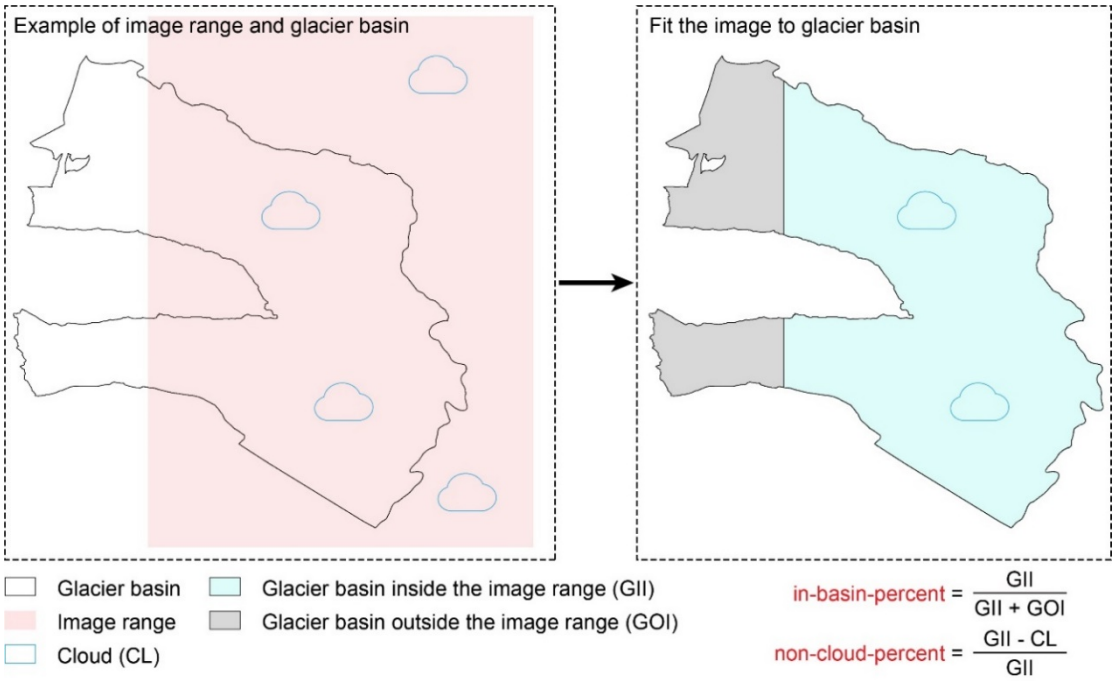

Figure 3.2 Schematic illustration of the calculation for in-basin-percent and non-cloud-percent

3.3.2 Satellite imagery acquisition

In this study, I used Landsat 8 (L8) and Sentinel-2 (S2) imageries. L8 images are acquired from the product of Level-1 Tier 1 Top of Atmosphere (TOA) and S2 images are acquired from the product of S2 Level-1C (TOA), both datasets are available for analysis through GEE. TOA reflectance values are known to better represent surface conditions over the ice sheets than the image with raw digital numbers (Pope et al., 2016b), and have been used previously for supraglacial lake studies (Moussavi et al., 2020; Williamson et al., 2018a). I first selected images that cover the glacier mask from May to September between 2014–2021 and 2016–2021 for L8 and S2, respectively.

Next, images with sun elevation angle less than 20° were removed from the generated image collections because the surface water bodies are not significantly spectrally different from surrounding features under low light conditions (Halberstadt et al., 2020; Moussavi et al., 2020; Dirscherl et al., 2020). To further select the usable images, I calculated how much the image can cover the glacier mask as "in-basin-percent" which showed in Figure 3.2. Besides, I introduced "Simple Cloud Score Algorithm" (ee.Algorithms.Landsat.simpleCloudScore) in GEE to assess the cloud cover inside the glacier mask for L8 imagery. This algorithm performs better than other methods based on a single band threshold, by assigning a simple cloud-likelihood score between 0 and 100 to every pixel in the image using multiple bands or band combinations (Dell et al., 2020). I arbitrarily set 40 as the cloud threshold after investigating the cloud mask, which means pixels with a value higher than 40 are treated as clouds. For S2 images, I introduced the dataset of "Sentinel-2: Cloud Probability", which is also directly available from GEE. The dataset is created with sentinel2-cloud-detector library developed by Sentinel Hub (https://github.com/sentinel-hub/sentinel2-cloud-detector). Similar to the Simple Cloud Score Algorithm for L8 imagery, a mask of cloud-likelihood score between 0 and 100 for every S2 scene was derived utilizing the cloud probability dataset. I set 65 as the cloud threshold after checking the cloud mask. By using these thresholds, I calculated non-cloud coverage within the part of image inside the glacier mask as "non-cloud-percent" (Fig. 3.2). I then removed the images with less than 90% of in-basin-percent and non-cloud-percent, generated a L8 image collection with 166 images and a S2 image collection with 317 images.

3.3.3 Lake area delineation

I employed a pixel-based random forest supervised classification approach on the GEE to derive water extent from L8 and S2 imageries. An overview of the methodology is shown in Figure 3.3, and I will introduce the processing steps in the following sections.

Table 3.1 Predictors used to derive training data for each satellite

Circle represents the spectral band or index is used for the corresponding satellite, cross represents the spectral band or index is not used for the corresponding satellite.

Predictors	Formula	Satellites	
		L8	S2
Spectral bands			
blue		○	○
green		○	○
red		○	○
nir		○	○
swir1		○	×
swir2		○	×
vre (1–4)[1]		×	○
Spectral indices			
$NDWI_{ice}$[2]	(blue − red) / (blue + red)	○	○
NDSI[3]	(green – swir1) / (green – swir1)	○	○
$AWEI_{sh}$[4]	blue + 2.5 × green – 1.5 × (nir + swir1) – 0.25 × swir2	○	○
$AWEI_{nsh}$[5]	4 × (green – swir1) – 0.25 × nir – 2.75 × swir2	○	○
TC_{wet}[6]	0.1509 × blue + 0.1973 × green + 0.3729 × red + 0.3406 × nir + 0.7112 × swir1 – 0.4572 × swir2	○	○
$SAVI_{mod}$[7]	(nir – red) / (nir + red + 1) × 2	○	○
NWI[8]	(blue – nir – swir1 –swir2) / (blue + nir + swir1 + swir2)	○	○
SI_{mod}[9]	(blue − nir) / (blue − nir)	○	○

Note: (1) 4 Vegetation Red Edge bands of S2 imagery (band 5, 6, 7 and 8A). (2) Normalized Difference Water Index (Moussavi et al., 2020; Williamson et al., 2018a; Yang and Smith, 2013). (3) Normalized Difference Snow Index (Hall et al., 1995; Dozier, 1989). (4) Automated Water Extraction Index with the option of shadow (Feyisa et al., 2014). (5) Automated Water Extraction Index with the option of dark area removal (Feyisa et al., 2014). (6) Tasseled Cap for wetness (Crist and Cicone, 1984). (7) modified Soil-Adjusted Vegetation Index (Huete, 1988). (8) New Water Index (Feng, 2012). (9) modified Shadow Index (Li et al., 2016)

(1) Training data generation

Training labels are required to support the supervised classification algorithms during

the model training. My goal is to identify water pixels within the glacier mask thus I created binary training labels as water and non-water. For each of the datasets (L8 and S2), I selected training images (Table 3.3) from the already generated image collections in 3.2. In order to collect information of seasonally variable water conditions as possible, the training images were selected so that they cover the whole melt season (May–September). Besides, I deliberately chose typical images that include cloud and shade inside the glacier mask to enrich the training sample of non-water. For each of the training images, training regions were defined manually by drawing polygons in GEE. The regions were evenly distributed inside the glacier mask containing information on water and non-water (including snow, ice, cloud, shade).

Following Dirscherl et al. (2020), spectral bands and spectral indices are calculated and used as predictors for the classification process to support the discrimination between water and non-water. Due to the different spectrum designs between the two satellites, the predictors are employed differently (see Table 1 for details). For the S2 imagery, I harmonized all spectral bands involved in the spectral index calculation of to the spatial resolution of 10 m using bilinear resampling algorithm. All the L8 images were resampled from the resolution of 30 m to 10 m to match the S2 imagery for the time series generation (see 3.4 for details). Lastly, pixel values of these predictors inside the training regions are derived as training data to be fed to the classifier. The relative importance of each predictor used for the random forest classifier was also determined within GEE.

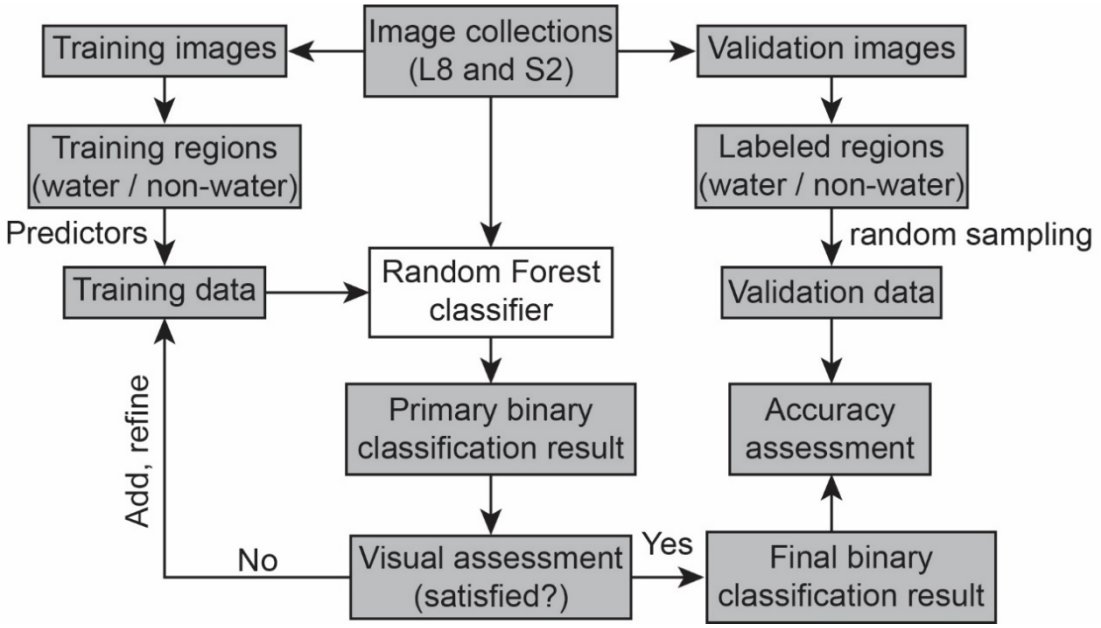

Figure 3.3 Flowchart illustrating the lake area delineation by random forest method

(2) Image classification

I applied a random forest classifier (Breiman, 2001) to classify the selected satellite images. As a machine learning method, random forest algorithm constructed multiple uncorrelated random decision trees, which are bootstrapped and aggregated to classify a dataset by using the mode of predictions from all decision trees (Pal, 2005; Belgiu and Drăguţ, 2016). The random forest method has been widely applied for resolving remote sensing classification issues not only due to its robust performance, but its computational efficiency and easy implementation compared to other machine learning method (Belgiu and Drăguţ, 2016; Chan and Paelinckx, 2008; Denisko and Hoffman, 2018). And it has been used in supraglacial lake detecting recently (Dell et al., 2021; Dirscherl et al., 2020; Dirscherl et al., 2021; Halberstadt et al., 2020).

The classification was carried out in GEE using random forest classifier (function ee.Classifier.smileRandomForest in GEE). Number of decision trees is an input parameter in the random forest classifier, the overall accuracy of classification would increase when the number of decision trees increasing without overfitting (Breiman, 2001), but the computational complexity increasing accordingly. To avoid computational limits in GEE, I balance the computational complexity and accuracy,

setting the number of trees as 96 and 128 for L8 and S2 imagery, respectively. Visual assessment of initial binary classification results is compared with the optical image. For some obvious false classification areas (e.g. cloud shade, cloud, and water extent under thin cloud), I added or refined the training samples and then used the enlarged training data to classify the image. This process will loop until the classification becomes stable and high classification accuracy is achieved. An overview of the methodology is illustrated in Figure 3.3.

(3) Accuracy assessment

Once a satisfactory classification result was attained, the accuracy assessment was performed using independent validation datasets. Validation images were selected from the already generated image collections described in 3.2, but different from training images. Since L8 and S2 images were overlapping in time between 2016−2021, I selected 5 L8 and S2 image pairs (Table 3.3) which are taken within < 10 min of each other, and then visually inspected the image pairs to make sure no obvious difference (e.g. fast cloud movement or rapid lake drainage event) within the glacier mask between the image pair.

Since there is no pan-Greenland supraglacial lake inventory published up to now and the supraglacial lake extent is changing with time, I manually checked the image pairs and labeled the water area, treating the labeled area as the ground truth. The labeled water area could be applied for the contemporaneous L8 and S2 images since they are nearly the same. For every validation scene, I randomly sampled 1500 points within the labeled water area as the water pixels. Then I established a 300 m buffer area around every labeled water area, and randomly sampled 1500 points within the buffer area as non-water pixels as well. These non-water pixels are more representative to be the validation data because the surrounding-water-areas are potentially prone to misclassification (Dirscherl et al., 2020). To ensure the non-water pixels are derived from various environmental objects, I intendedly chose the cloud, shade, or slush area as the non-water area beside the surrounding-water-areas, and further selected 1500

points randomly as the non-water pixel from these areas. These selected water and non-water pixels are deemed as manual-labeled binary result (hereafter, actual result).

The accuracy assessment was performed by a comparison between the actual result and the predict result (selected pixels classified by the already established random forest classifier), and shown as a confusion matrix (Table 3.2) (Stehman, 1997). Following Dirscherl et al. (2020) and Teluguntla et al. (2018), I calculated the user accuracy (*UA*) and producer accuracy (*PA*), which were used to evaluate performance of the random forest classifier for each class. Additionally, overall accuracy (*OA*) and Cohen's Kappa (*K*) were computed to assess the overall performance of the random forest classifier (Dirscherl et al., 2020; Landis and Koch, 1977; Teluguntla et al., 2018).

Table 3.2 A framework of confusion matrix for the accuracy assessment

		Actual		*UA*
		water	non-water	
Predict	water	True positive (*TP*)	False negative (*FN*)	*TP* / (*TP* + *FN*)
	non-water	False positive (*FP*)	True negative (*TN*)	*TN* / (*FP* + *TN*)
	PA	*TP* / (*TP* + *FP*)	*TN* / (*FN* + *TN*)	

The precision indicators (*OA* and *K*) were calculated as follows (*EA*: expected accuracy, a parameter used for calculating *K*):

$$OA = \frac{TP + TN}{TP + FN + FP + TN} \tag{3.1}$$

$$K = \frac{OA - EA}{1 - EA} \tag{3.2}$$

$$EA = \frac{(TN + FP) \times (TN + FN) + (FN + TP) \times (FP + TP)}{(TN + FN + FP + TP) \times (TN + FN + FP + TP)} \tag{3.3}$$

3.3.4 Time series generation

I obtained two binary lake mask collections from L8 and S2 imageries at 10 m resolution through the lake area delineation. From these binary lake masks, clusters that ≤ 18 pixels in total and linear features ≤ 3 pixels wide were removed because these

kinds of features may represent areas of mixed slush or supraglacial rivers rather than lakes (Moussavi et al., 2020; Pope et al., 2016a; Williamson et al., 2018a).

S2 and L8 have a revisit time of 5-day (a combination of S2A and S2B) and 16-day at the equator, respectively. However, the scenes are usually overlapping in the polar region so that the images there have a higher revisit frequency (e.g. S2 images can be derived nearly daily frequency regardless of the cloud cover), which enable us to monitor the supraglacial lakes at a high temporal resolution. Additionally, a combination of L8 and S2 offers a great opportunity to catch the condition of the lakes more frequently, and the dual-satellite-monitoring has been used to track the supraglacial lake evolution in Greenland (Williamson et al., 2018a) and Antarctic (Dell et al., 2020; Moussavi et al., 2020). Here I followed Williamson et al. (2018), generated a seasonal series of the supraglacial lake area using L8 and S2 imagery between 2014 and 2021. The L8 and S2 images are selected by a strict criterion of in-basin-percent (> 90%) and non-cloud-percent (> 90%) (see 3.2). Although not all images can fully cover the entire glacier mask, the average in-basin-percent of L8 and S2 images are 99.4% and 99.2%, respectively. The uncovered parts are distributed in the edge of the glacier mask where supraglacial lake rarely appears. Besides, the limited cloud cover may occlude the lake in very few cases even the average non-cloud-percent is 98.4% and 98.7% for L8 and S2, respectively. Considering most of the images are not effect by the cloud or image coverage, I arbitrarily deem that every individual image can fully present the environment within the glacier mask. To test the agreement between L8 and S2 lake areas. I compared areas of 1249 lakes defined using random forest algorithm from 21 contemporaneous L8 and S2 images pairs (acquired within < 20 minutes of each other). The result (Fig. 3.12) showed a significant correlation between the two sets of lake areas (r^2 = 0.996, p = 0.000, RMSE = 0.010 km^2), thus, I deem that lake area derived from L8 and S2 images defined by my method are the same. I then fused L8 and S2 lake masks between 2014 and 2021 into one time series. When both L8 and S2 lake masks are available on the same day, S2 lake mask is preferentially used because

the S2 lake masks have a better resolution (10 m) in the raw image than the L8 images which have been resampled from 30 m to 10 m (see 3.3.1). There are, in some cases, two S2 lake masks available on the same day, the lake masks which have a higher non-cloud-percent would be used in this case.

3.3.5 Climate data

To compare lake areas with surface climate conditions, I used near-surface air temperature, modeled surface snowmelt, and modeled surface mass balance (SMB) data. I used air temperature data at Qaanaaq (77.48°N, 69.38°W; 16 m a.s.l.) (Fig. 3.1a), obtained from NOAA's National Centers for Environment Information (https://www.ncei.noaa.gov/), representing low elevation air temperature. I also obtained the temperature record at SIGMA-B (77.54°N, 69.07°W; 944 m a.s.l.), located on Qaanaaq Ice Cap (Fig. 3.1a), representing the high elevation air temperature. The SIGMA-B station belongs to the Japan SIGMA project (Aoki et al., 2014) and the data could be obtained through Arctic Data archive System (https://ads.nipr.ac.jp/). Both stations situated about 75 km west of the glacier terminus.

In addition to the air temperature data, I also adopted modelled snowmelt and SMB outputs from the Regional Atmospheric Climate Model version 2.3p2 (RACMO2.3p2) downscaled dataset (Noël et al., 2019), which has a resolution of 1 km. Details of the model can be found in Noël et al. (2016, 2019).

3.4 Results

3.4.1 Evaluation of the classification method

1). Relative importance of predictors

The random forest classifier provides a quantitative measurement of each predictor's contribution to the classification result, which is useful in evaluating the importance of each predictor. The results showed us all predictors (spectral bands and spectral indices) contribute toward the classification of water and non-water features in both satellite

imagery datasets (Fig. 3.13). The predictors are used partly different between L8 and S2 imageries, therefore they contribute differently to the random forest classifier for both datasets. For the L8 imagery, $NDWI_{ice}$, as a spectral index, is of the greatest importance for the random forest classifier, with a relative importance over 10% (Fig. 3.13a). Followed by $NDWI_{ice}$, spectral bands blue, swir2, swir1, and spectral indices $SAVI_{mod}$, NDSI, also contribute significantly (> 7%) to the classification (Fig. 3.13a). For the S2 imagery, NDSI and $NDWI_{ice}$, with a relative importance of 8.1% (Fig. 3.13b), are the most two important contributors fed to the random forest classifier. Followed by the two spectral indices, spectral band vre4 (band 8A), blue, and vre2 (band 6) showed a relative importance over 6% (Fig. 3.13b). The rest of the predictors I did not mention above have similar weightings, with the relative importance range between 5.96% – 6.76% for L8 imagery (Fig. 3.13a), and 5.28% – 6.04% for S2 imagery (Fig. 3.13b).

2). Classification accuracy

The results of the accuracy assessment for classification of L8 and S2 imageries were shown as confusion matrixes in Table 3.4, providing producer accuracy (a measure of omission error), user accuracy (a measure of commission error), overall accuracy, and Kappa. The results showed a high overall accuracy of 98.48% and 98.56% for L8 and S2, respectively. As the other indicator to assess overall performance, Kappa also showed a similarity between L8 (0.9653) and S2 (0.9673). As for the producer accuracy, the performance of water class is lower that non-water class for both L8 (97.28% vs 99.06%) and S2 (96.73% vs 99.46%). However, the performances of water class and non-water class in user accuracy are similar for L8 (98.06% vs 98.68 %) and S2 (98.88% vs 98.41%).

3.4.2 Spatial extent and distribution of SGLs

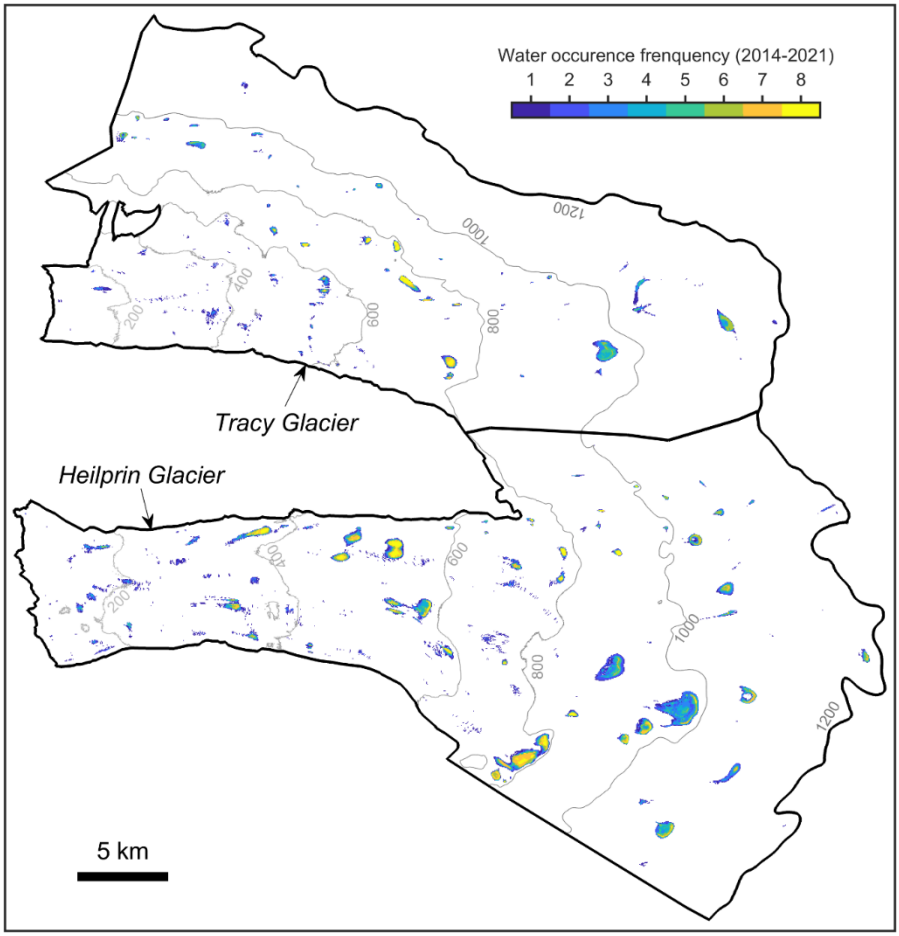

Figure 3.4 Spatial distribution of SGLs on Tracy and Heilprin Glacier
The colormap showed the recurrence frequency of water pixels between 2014 and 2021. Elevation contours derived from ArcticDEM Mosaic (Porter et al., 2018) are shown in gray.

To understand the maximum lake extent within the research area over the eight melt seasons, I calculated the cumulated SGL extent over 2014–2021 (Fig. 3.4). SGLs are found in every 200 m elevation bands in both Heilprin and Tracy Glacier (Fig. 3.4). Although the basin area of Tracy Glacier (540.62 km^2) is comparable to that of Heilprin Glacier (654.15 km^2), the lake extent in Tracy Glacier is 7.60 km^2, accounting for only one-third of that in Heilprin Glacier (22.84 km^2) (Fig. 3.5a). The basin area increased with the rising elevation band, while the lake extent also increases with the basin area up to the elevation band 800–1000 m, with the largest area of 5.94 km^2 and 2.28 km^2 among all elevation bands in Heilprin and Tracy Glacier, respectively (Fig. 3.5b). Despite the continuous basin area increasing in elevation band 1000–1200 m, the lake

extent decreased to 3.66 km^2 and 1.37 km^2 in this band for Heilprin and Tracy Glacier (Fig. 3.5b).

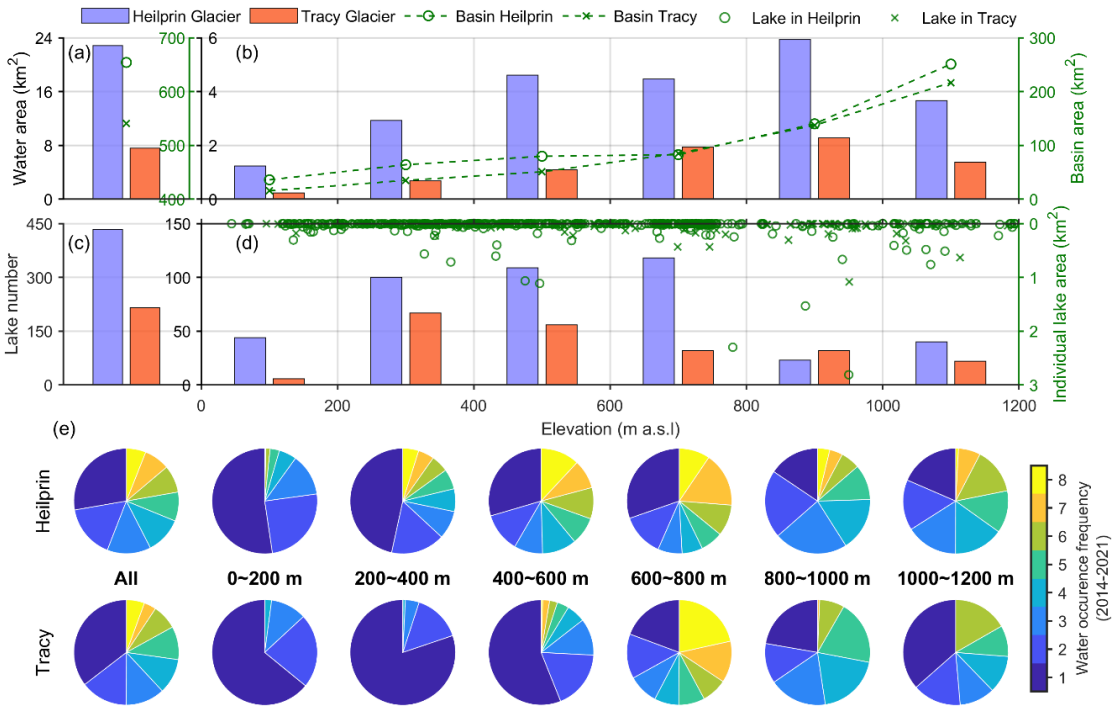

Figure 3.5 Lake area, number, and occurrence frequency for the studied glaciers Water area (bar graph) and basin area (blue dash line) in the whole glacier (a) and 200 m elevation bands (b) and for Heilprin and Tracy Glacier. Number of SGLs in the whole glacier (c) and 200 m elevation bands (b) for Heilprin and Tracy Glacier, green circle and cross markers in (d) are area of individual SGL and altitudinal distribution in Heilprin and Tracy Glacier. (e) Contribution of water occurrence frequency in whole glacier and 200 m elevation bands for Heilprin and Tracy Glacier.

To count the lake number within the two glaciers, I applied a two-dimensional eight-connected threshold (i.e. pixels are connected if their edges or corners touch) to define each individual SGL (Dell et al., 2020). I observed 434 and 215 SGLs in Heilprin and Tracy Glacier, respectively (Fig. 3.5c). In Heilprin Glacier, the number of SGLs increases with the altitude increasing and reach the maximum (118) in elevation band 600–800 m, but sharply decrease above 800 m. Conversely, the maximum number of SGLs (67) appears in the elevation band 200–400 m, then showed a gradual upglacier decreasing trend in Tracy Glacier (Fig. 3.5d). Among all the SGLs, over 98% of the SGLs areas are smaller than 0.5 km^2, mean lake areas are 0.053 km^2 and 0.035 km^2 for Heilprin and Tracy Glacier, respectively. Large lakes (> 0.5 km^2) are mainly distributed

in the area higher than 400 m a.s.l. (Fig. 3.5d). The largest lakes in Heilprin and Tracy Glacier are both located in the elevation of 950 m a.s.l, with an area of 2.81 km^2, and 1.09 km^2, respectively (Fig. 3.5d).

Figure 3.5e illustrated the contribution of water occurrence frequency in 200 m elevation bands and whole glacier for these two glaciers. I find that over 60% of the water pixels occurred at least twice between 2014–2021 in Heilprin (72%) and Tracy Glacier (65%) (Fig. 3.5e). Over the eight research years, 6% of the water pixels were observed every year in both glaciers (Fig. 3.5e). Water pixels form more randomly near the glacier terminus but have a high tendency to reform annually in the same locations in the upstream of the glacier, and this trend is more significant in Tracy Glacier. Water pixels with an occurrence frequency less than 2 (including 2) account for 87%, 95% and 74% of the total water pixels in the elevation band 0–200 m, 200–400 m and 400–600 m in Tracy Glacier, however, account for only 33%~51% in the elevation band higher than 600 m, and the range is 34%~44% in the elevation band higher than 400 m in Heilprin Glacier (Fig. 3.5e). I noticed that water pixels most recurred in the middle part of the glaciers, about 34% of the water pixels were observed 7 or 8 times in the elevation band 600–800 m but no more than 3% in other elevation bands in Tracy Glacier (Fig. 3.5e). Meanwhile, 21% and 26% of the water pixels have an occurrence frequency equal to or more than 7 in elevation band 400–600 m and 600–800 m in Heilprin Glacier, except for the near-terminal area (0–200 m band), at least 7% of the water pixels recurred 7 or 8 times in other elevation bands, which is different from Tracy Glacier (Fig. 3.5e).

3.4.3 Intra-annual and inter-annual lake evolution

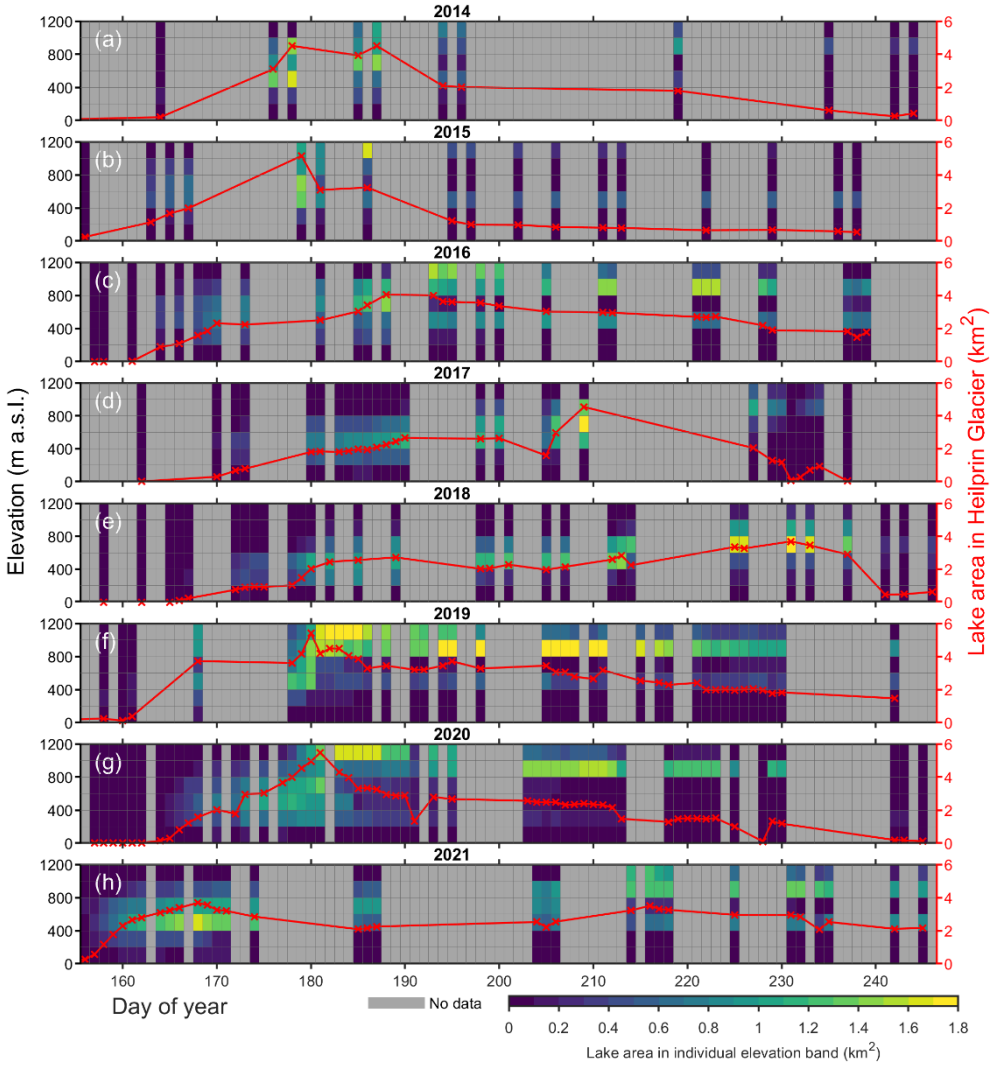

Figure 3.6 Lake area variation in Heilprin Glacier

The lake areas are showed by 200 m elevation band over the melting season between 2014 and 2021 (color patches), grey patches indicate no data available, red lines indicate total lake area in Heilprin Glacier.

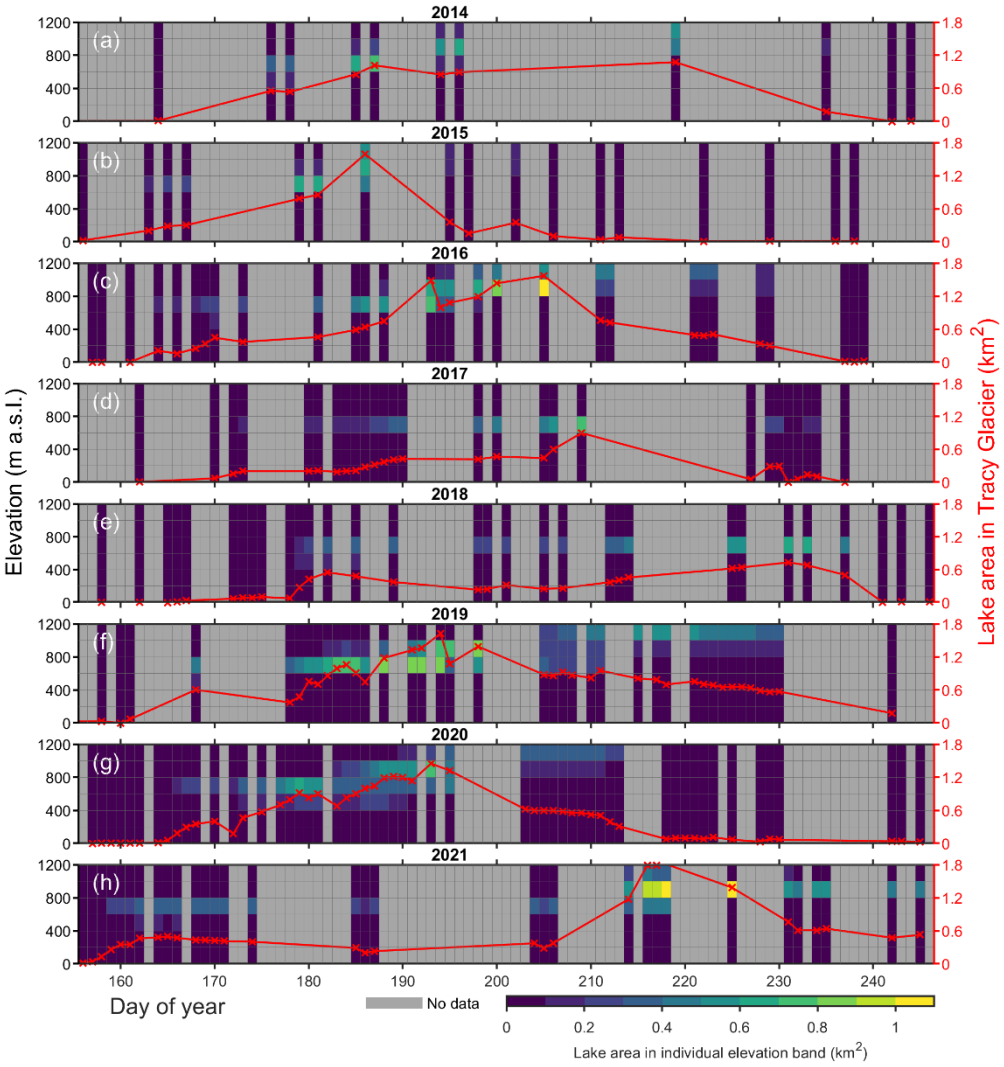

Figure 3.7 Same as Figure 3.6 but for Tracy Glacier.

Over the eight melting seasons, the onset of lake formation usually occurs in early June (days 155–165) from low elevation areas (Fig. 3.6 and 3.7), which was followed by a substantially increasing of the lake area, meanwhile, the lake extent migrated up-glacier in both Heilprin and Tracy Glaciers. The peaks of lake area are usually observed in late June and early July (days 178–187) in Heilprin Glacier (Fig. 3.6), while the peaks have about 10 days delay in Tracy Glacier (Fig. 3.7). However, increasing in the total area are relatively slow in 2017 and 2018 in Heilprin Glacier, the peaks occurred on 28 July (days 209) and 19 August (days 231), respectively (Fig. 3.6d–e), and interestingly, synchronized peaks are observed in Tracy Glacier in 2017 and 2018 (Fig 3.7d–e), which is different from other years. After reaching a maximum thereafter, the lake area gradually decreased toward the end of melt season. Most of the lakes were demised at

the end of August (around days 240), except for a few large lakes that still exist in high elevation areas in Heilprin Glacier until the last available image during the melt season (Fig. 3.6). In the two research glaciers, the SGLs are typically disappeared by surface refreezing or/and buried in snow and discharged into the englacial environment. The surface-refreezing-or/and-buried type SGLs are commonly observed at the end of melt season or after heavy snowfalls in the area higher than 800 m a.s.l., this kind of lake disappearance is often started with growing floes from one side of the lake or ice lid enlarged from lake centers outward (e.g. Fig. 3.14a–c). While the discharge type SGLs are generally observed before August in low and mid-elevation areas, among which some lakes drain rapidly (i.e. almost lost all its area within four days) via moulins or crevasses (e.g. Fig. 3.14d–e).

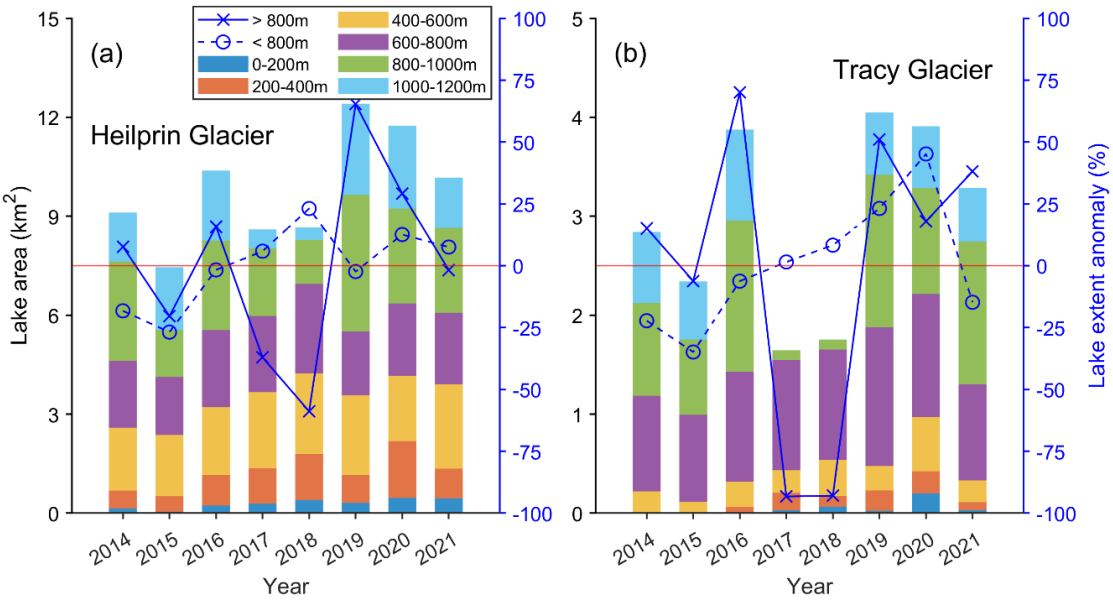

Figure 3.8 Inter-annual lake area variation
The lake areas are showed within individual 200 m elevation bands (stacked bar graph) for Heilprin Glacier (a) and Tracy Glacier (b). Blue solid and dashed lines show the lake extent anomaly within the area higher and lower than 800 m a.s.l., respectively.

The inter-annual lake area variation over the eight research years for Heilprin and Tracy Glacier is shown in Figure 3.8. A marked difference could be found between different years. The highest total lake area was observed in melt in 2019 for both Heilprin (12.41 km^2) and Tracy Glacier (4.05 km^2). The lowest total lake area was seen in 2015 for Heilprin Glacier (7.45 km^2), and relative low lake areas were also seen in 2017 (8.60

km^2) and 2018 (8.67 km^2), which account for only 70% of the peak area in 2019 (Fig. 3.8a). The variations are more striking in Tracy Glacier, the relatively low lake coverage was found in 2017 (1.65 km^2) and 2018 (1.75 km^2), which was only 40% of the peak lake extent in 2019 (Fig. 3.8b).

Although a clear inter-annual variation could be seen in the total lake area, different variation pattern exists in different parts of the glaciers. A relatively low amplitude variation was observed in the region lower than 800 m a.s.l., the maximum anomalies of the lake extent are −27% (2015) and 45% (2020) for Heilprin and Tracy Glacier, respectively (Fig. 3.8). However, drastic changes are detected in the region higher than 800 m a.s.l., with maximum anomalies of 65% (2019) and −93% (2017 and 2018) for Heilprin and Tracy Glacier, respectively (Fig. 3.8). Generally, SGLs are widely distributed in the elevation higher than 800 m a.s.l. (Fig. 3.4 and Fig. 3.5b), with a mean coverage of 42% and 43% for the total lake area for Heilprin and Tracy Glacier, respectively. However, the lake extents are anomaly low in 2017 and 2018 within the elevation band above 800 m a.s.l. (Fig. 3.8), accounting for only ~30% and 6% of the total lake area of Heilprin and Tracy Glacier in that year. Specifically, lakes were even not appeared in the 1000–1200 m band of Tracy Glacier in 2017 and 2018 (Fig. 3.8b and Fig. 3.15d-e). The fluctuations of lake area at altitudes from 800 to 1200 m dominate the variation of the total lake area.

3.4.4 Comparison with climatic data

To investigate the potential climate control of the lake development, I compared my lake area results with the daily surface snowmelt rates from RACMO2.3p2 downscaled product (Noël et al., 2019) within three discrete elevation bands (0–400, 400–800, 800–1200 m a.s.l.), and the daily average air temperature in Qaanaaq (16 m a.s.l.) and SIGMA-B (944 m a.s.l.) during the 2016–2021 melt season. The mean air temperature in Qaanaaq is 3.6 °C during the 2016–2021 melt season, which is about 5 °C higher than that in SIGMA-B. And the air temperature in the two stations is well correlated ($r^2 = 0.74$, $p < 0.001$).

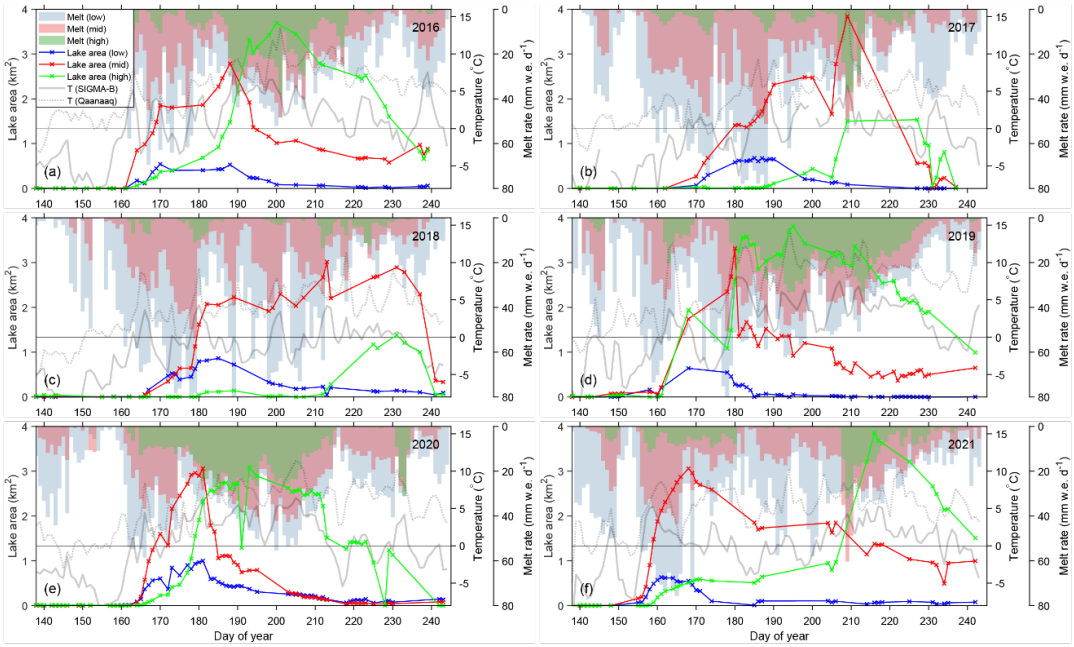

Figure 3.9 Comparison between lake area and climatic data

Time series of total lake area (line plot) and daily average RACMO melt rate (bar graph) and within low (0–400 m), mid (400–800 m), and high (800–1200 m) area of Tracy and Heilprin Glacier between 2016 and 2021 (a–f). Gray solid and dashed lines denote daily average air temperatures in Qaanaaq (16 m a.s.l.) and SIGMA-B (944 m a.s.l.), respectively.

I find that high air temperature or high melt rate do not necessarily correlate with larger area of lake coverage, particularly because the lake area demonstrated different variation patterns among different elevation bands. In the low elevation area (0–400 m a.s.l.), the lakes form with the first sharp temperature rise (5 °C or more increasing within five days) in Qaanaaq every year and draining earlier in the melt season than the higher regions (Fig. 3.9). Although the melt rate is the strongest among the three elevation bands, the total lake area is always lower than 1 km^2 through all the six melt seasons, which is much lower than those in higher elevation bands (Fig. 3.9). In the middle elevation area (400–800 m a.s.l.), the initial lake evolution has a similar timing, but the rate of lake growth is much faster as compared with those in the low elevation area (Fig. 3.9). The lake area progressively increased until a peak value. Before reaching the peak value, the fluctuation of lake area keep pace with the variation of melt rate and temperature. After reaching the peak, a steep decrease was thereafter observed except in 2018, and the lake area showed less clear relationship with the air

temperature and melt rate. In 2018, the lake area did not experience a sharp decline but varied with the fluctuation of air temperature and melt rates throughout the whole melt season (Fig. 3.9). Lake area in the high elevation area (800–1200 m a.s.l.) showed the greatest interannual variations, which were largely in agreement with the melting rate (Fig. 3.9). The peak lake areas in 2017 and 2018 are only 1.53 (days 227, 15-Aug) and 1.17 (days 231, 19-Aug) km2, less than half of the peak area in the other years. Melt rates in those two years are obviously smaller compared with other years (Fig 3.9b-c). Also, the mean temperature at SIGMA-B during the June–August in 2017 and 2018 is −0.54 and −0.98 °C, which is more than 1°C lower than the 6-year average (0.52°C).

3.5 Discussion

3.5.1 Method assessment

(1) Relative importance of predictors

As shown in Figure 3.13, each predictor contributes differently (5.3–8.1% for S2 and 6.0–10.6% for L8) in the random forest classifier. In both imagery datasets, $NDWI_{ice}$ contributes the most (or nearly most) in the classification, meaning that the $NDWI_{ice}$ is a predominant spectral index in differentiating ice and water. This proves that $NDWI_{ice}$, which widely used in threshold-based method, is an effective index to classify water and ice (Fitzpatrick et al., 2014; Moussavi et al., 2020; Williamson et al., 2018a). Although some predictors contribute less than the others, they may still be important in the classification because my non-water class contains not only ice and snow but cloud and shade. Also, these predictors are proved effective in the discrimination of water, ice, and shadow (Dirscherl et al., 2020; Dirscherl et al., 2021; Moussavi et al., 2020). As mentioned by Dirscherl et al. (2021), a broader range of predictors is beneficial to adopt the lake detection approach more widely in space and time. Thus, I consider all the predictors are necessary for the classification regardless of the different contributions.

(2) Cloud effect

The optical imagery is sometimes blocked by clouds and other weather-related

obstacles (e.g. fog), therefore may hinder the lake detection if the cloud cover were just above the lake. To compensate for the underestimation of lake area caused by cloud cover, Williamson et al. (2018) adopted an index called “portion of region visible”, which measures the percentage of pixels not obscured by cloud or are not missing data values. And the total lake area is adjusted by dividing the daily total lake area by the portion of the region visible on that day. Tuckett et al. (2021) introduced a similar index of “image visibility scores” to measure the image visibility from cloud cover and adjust the lake area.

I did not adopt such an index to adjust the lake area in the calculation because I have used a similar index called “non-cloud-percent” to acquire the images with less than 10% of cloud coverage within the glacier basin (see 3.2), which minimizes the impact of cloud cover. Despite I have adopted the relatively strict cloud criterion, few of the selected S2 images are still widely covered by thin cloud because the dataset of Sentinel-2: Cloud Probability might have performed not well on a thin cloud area. In that case, the thin cloud hinders the discrimination of water (Fig. 3.16) and thus I noticed the cases that lake area sharply decreased and soon recovered anomaly (e.g. day 231 in 2017, day 191 and 228 in 2020, day 234 in 2021, see Fig. 3.6 and 3.7). However, these cases are rarely appeared and could be easily found in a continuous lake area series because sharply decrease in lake area induced by fast discharge events would not be followed by recovering in a short time (Williamson et al., 2018a). Moreover, underestimation of lake area happened only when other objects were wrongly identified as water bodies. So that I think my method to calculate the lake area is effective although a few results may be affected by the cloud.

3.5.2 Spatial distribution

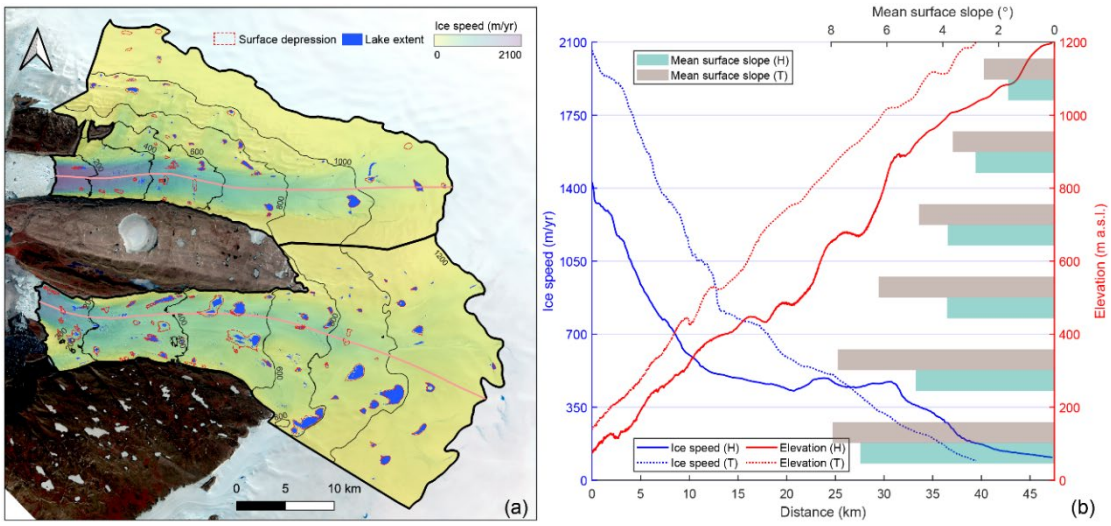

Figure 3.10 Lake extent and glaciology factors

(a) Ice speed distributions over Tracy and Heilprin Glaciers, ice speed derived from ITS_LIVE velocity mosaics dataset (Gardner et al., 2019), blue patches represent maximum annual lake extent from 2014 to 2021, red dash line polygons are surface depressions calculated by MATLAB package TopoToolbox (Schwanghart and Scherler, 2014) based on ArcticDEM Mosaic (Porter et al., 2018), the two pink curves are flowlines used for extracting elevation and ice speed profiles shown in (b). (b) Ice speed and elevation along the flowlines shown in (a) at Tracy and Heilprin Glaciers. Mean surface slope in 200 m elevation band is shown as bar graph.

The supraglacial lakes tend to form in topographic depressions on the ice surface (Lüthje et al., 2006; Echelmeyer et al., 1991; Box and Ski, 2007). Ice surface depressions on grounded ice are translation of the subglacial topographic undulations, thus the lakes tend to reform annually in the same location on the grounded ice (Echelmeyer et al., 1991; Sergienko, 2013). They are therefore do not migrate with ice flow, which mostly happened on the floating tongue of glaciers (e.g. Peterman Glacier, Macdonald et al., 2018; Nioghalvfjerdsfjorden Glacier, Turton et al., 2021). In my research, although Tracy Glacier had a floating terminus until 2005 (Porter et al., 2014; Veitch and Nettles, 2012), Heilprin and Tracy Glacier are now both grounded since 2005 (Hill et al., 2018). I delineated the surface depressions (>0.05 km^2) using the MATLAB package TopoToolbox (Schwanghart and Scherler, 2014) based on ArcticDEM Mosaic (Porter et al., 2018). Agreement between the distribution of maximum annual lake extent from 2014 to 2021 and the surface depressions indicates

that most of the lakes developed within the ice surface depressions (Fig. 3.10a), which agrees with the result of Ignéczi et al. (2016) that 75% of the SGLs fall within the surface depressions in Greenland Ice Sheet. The largest lakes are developed in the elevation of 950 m a.s.l. in both Heilprin and Tracy Glacier (Fig. 3.5d). The largest lake extents and mean individual lake areas are observed in the elevation band 800–1000 m for both glaciers (Fig. 3.5b and 3.5d), where the largest lake located. This is presumably because the slow-moving ice and low surface slope facilitate the growth of SGLs (Fig. 3.10). Despite relatively slow ice speed and gentle surface slope in the elevation band 1000–1200 m, the lake extents are not as extensive as that in the elevation band 800–1000 m in both glaciers. The decline in lake extents is likely attributed to the infilling of snow and/or refreezing of meltwater in the shallow surface depressions in the high elevation (Koenig et al., 2015; Ignéczi et al., 2016). I found that the water pixels occurred most frequently in the middle part of the glaciers (see 4.2 and Fig. 3.5e), especially concentrated in the elevation band 600–800 m, where 26% and 34% of the water pixels appeared at least 7 times in the 8-year observation for Heilprin and Tracy Glaciers. However, only less than 8% of the water pixels appeared over 7 times in the higher elevation band despite a larger lake extent, suggesting the appearance of lake in higher elevation is not only controlled by ice surface topography, but may be influenced by other factors. According to the field measurement in Qaanaaq ice cap, situated 75 km west of the studied glaciers, the melt rate is relatively less sensitive to elevation from about 400 m to 700 m a.s.l., but more sensitive to the elevation rising from 700 to 1000 m a.s.l. (Sugiyama et al., 2014), suggesting the production of meltwater is less affected by the elevation from 400 m to 700 m a.s.l., approximately the most frequently water recurred region. Subsequent research by Tsutaki et al. (2017) revealed that the ELA varied in 862–1001 m a.s.l. between 2012 and 2016 in Qaanaaq ice cap, further confirmed that there is an obvious transition in the melt condition between the elevation band 800–1000 m, which explained the dramatic change in the proportion of water occurrence frequency. Similar lake reform patterns also have been observed in Russell

Glacier (Fitzpatrick et al., 2014), grounded part of Peterman Glacier (Macdonald et al., 2018) and Nioghalvfjerdsfjorden Glacier (Turton et al., 2021) in Greenland Ice Sheet, suggesting that the ice surface topography provide a potential region for the formation of supraglacial lakes, but temperature may control whether the lake growing or not, especially in the high elevation area.

The lake extents are not always confined by the surface depression near the glacier terminus (in the elevation band 0–200 m in Heilprin Glacier and 0–600 m in Tracy Glacier). SGLs in these regions are in contrast appeared more randomly as over 70% of the water pixels occurred only one or two times in the 8-year observation (Fig. 3.5e) and the areas of individual lakes are generally smaller (no larger than 0.31 km^2, Fig. 3.5d and 3.10a) than lakes located higher in the glaciers. This may partly be attributed to the high surface slopes near the glacier terminus within these regions because the SGLs tend to develop in the relatively flat areas (Turton et al., 2021; Arthur et al., 2020; Sundal et al., 2009). I noticed that the surface slope in the elevation band 0–200 m in Heilprin Glacier and 0–600 m in Tracy Glacier is steeper than 6° (Fig. 3.10b), reflecting a widely crevassed surface there. However, the SGLs tend to develop in relatively flat regions, where the SGLs develop have an average slope of 2.8° and 2.5° for Tracy and Heilprin Glacier, respectively. Although the crevasses have the ability of meltwater retention (Colgan et al., 2016) and I do observe meltwater-filled crevasses in the early melt season, crevassing associated with fast ice flow prevents SGLs from growing as large before drainage occurs (Palmer et al., 2011; Fitzpatrick et al., 2014). The ice speed of Tracy and Heilprin Glaciers is over 1000 m a^{-1} along the flowline extending upstream from the front for about 12 km and 4.5 km, respectively (Fig. 3.10b). The fast ice flow results in the formation of new crevasses fields and changes the conditions of the existed crevasses (Colgan et al., 2016). Therefore, newly developed water-filled-crevasses (formation of new SGLs) and water discharge from existed crevasses (disappearance of existing SGLs) are frequently observed in the near-terminus region.

The ice speed in Tracy Glacier is faster than that in Heilprin Glacier until 26 km inland

from the glacier front along the flowline (Fig. 3.10b). The striking high ice speed of Tracy Glacier was previously reported by Sakakibara and Sugiyama (2018, 2020). Thinning rate of Tracy Glacier (−3.9 m a^{-1}) was over 7 times than that of Heilprin Glacier (−0.46 m a^{-1}) between 2000–2018 (Wang et al., 2021), which mostly attributed by the enhanced dynamic thinning at Tracy Glacier (Porter et al., 2014; Pritchard et al., 2009; Wang et al., 2021). In addition to the ice speed, the surface slope of Tracy Glacier is higher than that of Heilprin Glacier in every elevation band (Fig. 3.10b). As the SGLs are preferentially located away from the fast-flow units and steeper regions, I therefore speculate these glaciological factors limited the development of SGLs in Tracy Glacier.

3.5.3 Temporal evolution

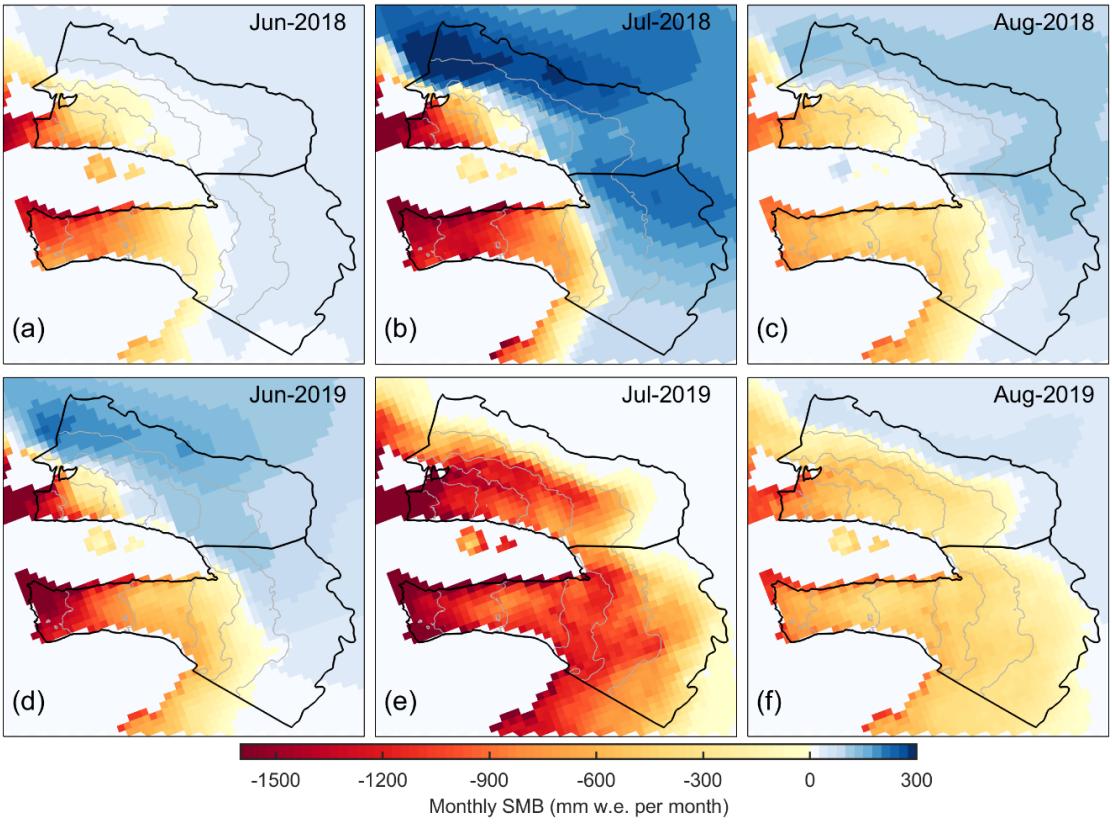

Figure 3.11 RACMO monthly surface mass balance
The monthly surface mass balance of Heilprin and Tracy Glaciers and surrounding regions from June to August in 2018 (a–c) and 2019 (d–e) from RACMO modeled output. The bold black lines are glacier boundaries, grey contours mark the elevations at every 200 m (same as Figure 3.4).

The maximum lake extent (Fig. 3.4) maps all the areas where SGLs have appeared over the melt seasons between 2014 and 2021 (i.e. the potential area where the lakes are likely to develop). However, the timing and extent of SGLs appearance vary inter/intra-annually, explaining the clear inter/intra-annual variation pattern of the total lake area. The initial spread of the SGLs in the two glaciers is observed from lower to higher elevations as the melt season progressed (Fig. 3.9). Generally, the surface melt/runoff, governed in part by air temperature and winter snowpack, controlled the initiation of SGLs formation (Arthur et al., 2020; Fitzpatrick et al., 2014; Macdonald et al., 2018; Tuckett et al., 2021). Although the total lake area or the evolution pattern of the SGLs varies inter-annually, the start of lake formation is approximately in early June (days 155–165, Fig. 3.6 and 3.7). This is similar to the timing with Peterman Glacier (81°N in northwestern Greenland, Macdonald et al., 2018), Nioghalvfjerdsfjorden Glacier (79°N in northeastern Greenland, Turton et al., 2021; Sundal et al., 2009), and Ryder Glacier (81°N in northwestern Greenland, Sundal et al., 2009). However, lakes began to develop as early as May in Russell Glacier (67°N in western Greenland, Fitzpatrick et al., 2014; Sundal et al., 2009) and Paakitsoq region (69°N in the western Greenland, McMillan et al., 2007), where the onset of above-freezing air temperature comes earlier due to the lower latitude. Before the lake area reaches its peak, a substantial increase in lake area was observed with the continuous above-freezing air temperature in Qaanaaq (Fig. 3.9). The peaks of the lake area of Heilprin Glacier were approximately 10 days earlier than that in Tracy Glacier in relatively warm years (2016, 2019 and 2020, Tedesco and Fettweis. (2020); Turton et al. (2021)), but nearly the same in 2017 and 2018, two anomalous cold summers in western Greenland (Sasgen et al., 2020). A possible explanation of the anomalous low lake area is that a larger portion (74%) of the lakes located above the elevation of 600 m in Tracy Glacier (Fig. 3.5d) where the above-freezing air temperature day comes later than low elevation area. Also, as I mentioned in 3.5.2, lakes in the area under the elevation of 600 m in Tracy Glacier are more randomly distributed and more likely concentrated in the crevasses (Fig. 3.4),

where lake tended to form small and have shorter longevity (Johansson et al., 2013; Selmes et al., 2011). Therefore, the peak lake area in Tracy Glaciers largely reflect the lake condition above 600 m a.s.l. (Fig. 3.6). In contrast to the peak lake area in Tracy Glacier, peak lake area in Heilprin Glacier not only include the lakes developed above 600 m a.s.l. but includes a significant portion of lakes developed in the elevation of 200–600 m (Fig. 3.7). However, in the relative cold year (2017 and 2018), the low temperature and small melt rate in the elevation 800–1200 m severely limited the lake growth there (Fig. 3.9b–c), peak area in Tracy Glacier only reflects lakes developed in the elevation of 600–800 m, therefore, synchronized with that of Heilprin Glacier.

There is a clear fluctuation in total area between 2014 and 2021, much attributed to the inter-annual variation in the total lake area above 800 m a.s.l (Fig. 3.8). As reported by Macdonald et al. (2018) and Turton et al. (2021), even in cold years, SGLs still form in low elevation of the glaciers because the development of SGLs is highly sensitive to the surface air temperature. Once daily mean temperature reaches 0 °C, a small rise in temperatures will cause surface melting resulting in the rapid growth of SGLs (Bartholomew et al., 2010). From my observations, I find that lake development under 800 m a.s.l. is not related with cold or warm year. Therefore, less fluctuation was seen in lake area below 800 m a.s.l. for Heilprin (< 25%) and Tracy Glacier (< 50%). However, in the elevation above 800 m, development of SGLs is restricted in cold years (2017 and 2018). In these two years, days with above-freezing air temperature were much limited and showed as short-lived spikes (Fig. 3.9b–c), whereas temperature continuously exceeded freezing temperature in the other years which resulted in well-developed SGLs above 800 m. As suggested by Turton et al. (2021), in addition to the local meteorology, the SMB also controlled the development of SGLs that the ELA marks the approximate maximum elevations of SGLs. From the monthly RACMO SMB, I noticed that the monthly SMB turned to negative at elevations band 600–800 m throughout the whole melt season in 2019 (Fig. 3.11a–c), while extended to 1000–1200 m in July and August 2020 (Fig. 3.11e–f), which coincides with the upper limit of

SGLs (Fig. 3.8 and 3.15).

Although the lake extent seems correlated with the local meteorology and SMB, more complex variation patterns exist inter-annually, particularly in the low (0–400 m) and mid-elevation (400–800) areas. SGLs in the low elevation region form and drain the earliest (Fig. 3.9) due to the lakes there are mostly water-filled crevasses or above transient closed moulin which is common at lower elevations than on thicker ice (Das et al., 2008; Johansson et al., 2013). In the midelevation region, total lake areas experienced obvious decreasings despite sustained high temperatures and melt rate through July and August, particularly in 2016, 2019 and 2020, losing over 50% of the peak area in one week or less (Fig. 3.9a, d and e). The sharp decrease was caused by individual or a serial of rapid drainage events which were commonly observed in Greenland ice sheet (Selmes et al., 2011).

The rapid drainage event occurs when the surface water penetrates ice, establishing a surface-to-bed connection through hydraulic fracture (Das et al., 2008; Stevens et al., 2015; Chudley et al., 2019). And the fast drainage events are usually happened in clusters because one individual drainage event possibly triggers one another through short-term perturbations in the regional stress/strain regime transmitted over length (Christoffersen et al., 2018; Fitzpatrick et al., 2014). I note that the rapid drainage events tend to recur in the same location in different years (e.g. Fig. 3.18 shows rapid drainage events in two locations in Heiprin Glacier and Fig. 3.19 shows rapid drainage events in one location in Tracy Glacier). Lakes sometimes undergo complete rapid drainage (Fig. 3.18c–d, h–j; Fig 3.19a–b), whereas sometimes undergo partial drainage (Fig. 3.18a–b, e–f, g–i; Fig. 3.19c–f). They did not drain at all in some cases but froze gradually till the end of the melt season alternatively. As suggested by Chudley et al. (2019), in the fast-flowing outlet glacier, the drainage types are largely dependent on the location of the moulin or fracture because moulins or fracture may experience a process of moving in and out of the lake bed due to the ice moving. The exact timing of the drainage initiation is difficult to forecast due to no common critical thresholds relating to lake

hydrology (depth, volume, or morphology), glaciological setting (hypsometry, velocity, or strain) or meteorological conditions have been found in the previous studies (Chudley et al., 2019; Fitzpatrick et al., 2014; Williamson et al., 2018b).

3.6 Conclusions

In this study, I have applied a machine learning method for mapping supraglacial lakes using two medium-resolution optical satellite datasets (Sentinel-2 and Landsat 8) within Google Earth Engine, generating a high spatial and temporal resolution record of lake area over Heilprin and Tracy Glaciers, northwestern Greenland from 2014 and 2021. To achieve this, I first made a glacier mask excluding ocean and rock which may lead to misclassification, then the random forest classifiers were trained on S2 and L8 imageries separately covering the two glaciers with two classes (water and non-water). The classifier performs well across the two glaciers over the 8 melt seasons, achieving overall accuracies over 98% for both satellites. Due to the good agreement ($r^2 = 0.996$, $p = 0.000$, RMSE = 0.010 km^2) between the two datasets of lake areas, these two datasets were combined into one lake area time series.

The maximum lake extent in Heilprin Glacier (22.84 km^2) is approximately 3 times as large as that in Tracy Glacier (7.60 km^2). In the low elevations (0–400 m), the lakes are relatively small and have a low occurrence frequency. In the middle elevations (400–800 m), the lakes tend to form larger and recur at the same location annually. The average lake area is largest in the high elevations (800–1200 m) but the occurrence frequency is not as high as that in the middle elevations because the lake development may be restricted in the cold year in the high elevations. The spatial distribution of SGLs is primarily determined by topography, surface slope and ice speed. Most of the SGLs are developed within the surface depressions and preferentially located away from the large slopes and fast-flow units in the glaciers.

The glaciology factors (e.g. topography, surface slope and ice speed) determine the potential area of the lake development, but the occurrence of lakes intra-annually relies

on the local meteorology and SMB. The SGLs on the two glaciers seasonally spread initially from lower to higher elevations as the temperature reaches above-freezing air temperature. High air temperature or high melt rate do not necessarily correlate with more extensive lake coverage particularly below the elevation of 800 m, because SGLs may drain extensively when moulin or fractures were opened as the melt season progressed. The maximum inland expansion of SGLs depends on the ELA, above which SGLs may not develop because no melting there. The fluctuation of the total areas in 2017 and 2018 is largely attributed to the limed developed lakes in the high elevations due to the cold weather conditions.

3.7 Appendix

Table 3.3 Summary of images used in the lake delineation

S2 product ID	Use
COPERNICUS/S2/20190514T173909_20190514T173911_T20XMM	Training (mainly water and non-water objects like ice)
COPERNICUS/S2/20190610T172909_20190610T172906_T20XMM	
COPERNICUS/S2/20190629T175919_20190629T175920_T20XMM	
COPERNICUS/S2/20190707T180921_20190707T180950_T20XMM	
COPERNICUS/S2/20190727T171909_20190727T171904_T20XMM	
COPERNICUS/S2/20190809T172909_20190809T172905_T20XMM	
COPERNICUS/S2/20190816T180921_20190816T180919_T20XMM	
COPERNICUS/S2/20190818T175919_20190818T175917_T20XMM	
COPERNICUS/S2/20200621T180921_20200621T180922_T20XMM	
COPERNICUS/S2/20200701T171859_20200701T171856_T20XMM	
COPERNICUS/S2/20200721T171859_20200721T171855_T20XMM	
COPERNICUS/S2/20200810T171859_20200810T171857_T20XMM	
COPERNICUS/S2/20200830T171859_20200830T171857_T20XMM	
COPERNICUS/S2/20200522T171859_20200522T171854_T20XMM	Training (mainly non-water objects like shadows and clouds)
COPERNICUS/S2/20200522T180921_20200522T180922_T20XMM	
COPERNICUS/S2/20200612T173911_20200612T173909_T20XMM	
COPERNICUS/S2/20200620T174909_20200620T174910_T20XMM	
COPERNICUS/S2/20200711T180921_20200711T180920_T20XMM	
COPERNICUS/S2/20200817T175921_20200817T180016_T20XMM	
COPERNICUS/S2/20190502T174911_20190502T174911_T20XMM	
COPERNICUS/S2/20190517T174919_20190517T174916_T20XMM	
COPERNICUS/S2/20190714T175921_20190714T180011_T20XMM	
COPERNICUS/S2/20180515T175909_20180515T175910_T20XMM	

COPERNICUS/S2/20190628T173911_20190628T173908_T20XMM	
COPERNICUS/S2/20160723T173912_20160723T173907_T20XMM	
COPERNICUS/S2/20190830T174911_20190830T174908_T20XMM	
COPERNICUS/S2/20180814T172959_20180814T173000_T20XMM	
COPERNICUS/S2/20190630T172909_20190630T172907_T20XMM	
COPERNICUS/S2/20200702T173911_20200702T173908_T20XMM	Validation
COPERNICUS/S2/20200711T171859_20200711T171855_T20XMM	
COPERNICUS/S2/20210806T173911_20210806T173906_T20XMM	
L8 product ID	**Use**
LANDSAT/LC08/C01/T1_TOA/LC08_034004_20190529	
LANDSAT/LC08/C01/T1_TOA/LC08_032004_20190702	
LANDSAT/LC08/C01/T1_TOA/LC08_030005_20190704	
LANDSAT/LC08/C01/T1_TOA/LC08_029005_20190713	Training
LANDSAT/LC08/C01/T1_TOA/LC08_033004_20190725	(mainly
LANDSAT/LC08/C01/T1_TOA/LC08_029005_20190729	water and
LANDSAT/LC08/C01/T1_TOA/LC08_032004_20190803	non-water
LANDSAT/LC08/C01/T1_TOA/LC08_029005_20190814	objects like
LANDSAT/LC08/C01/T1_TOA/LC08_029005_20200613	ice)
LANDSAT/LC08/C01/T1_TOA/LC08_031005_20200627	
LANDSAT/LC08/C01/T1_TOA/LC08_030005_20200722	
LANDSAT/LC08/C01/T1_TOA/LC08_030005_20200807	
LANDSAT/LC08/C01/T1_TOA/LC08_034004_20160824	Training
LANDSAT/LC08/C01/T1_TOA/LC08_032004_20170728	(mainly
LANDSAT/LC08/C01/T1_TOA/LC08_031005_20180825	non-water
LANDSAT/LC08/C01/T1_TOA/LC08_030005_20180903	objects like
LANDSAT/LC08/C01/T1_TOA/LC08_029005_20190830	shadows
LANDSAT/LC08/C01/T1_TOA/LC08_034004_20190630	and
	clouds)
LANDSAT/LC08/C01/T1_TOA/LC08_034004_20180814	
LANDSAT/LC08/C01/T1_TOA/LC08_034004_20190630	
LANDSAT/LC08/C01/T1_TOA/LC08_034004_20200702	Validation
LANDSAT/LC08/C01/T1_TOA/LC08_033004_20200711	
LANDSAT/LC08/C01/T1_TOA/LC08_034004_20210806	

Table 3.4 Accuracy assessment confusion matrix of L8 and S2 imageries

L8

		Actual		user accuracy
		water	non-water	
Predict	water	7829	155	98.06%
	non-water	219	16324	98.68%
producer accuracy		97.28%	99.06%	

Overall performance: Overall accuracy = 98.48%, Kappa = 0.9653

S2

		Actual		user accuracy
		water	non-water	
Predict	water	8551	97	98.88%
	non-water	289	17903	98.41%
producer accuracy		96.73%	99.46%	

Overall performance: Overall accuracy = 98.56%, Kappa = 0.9673

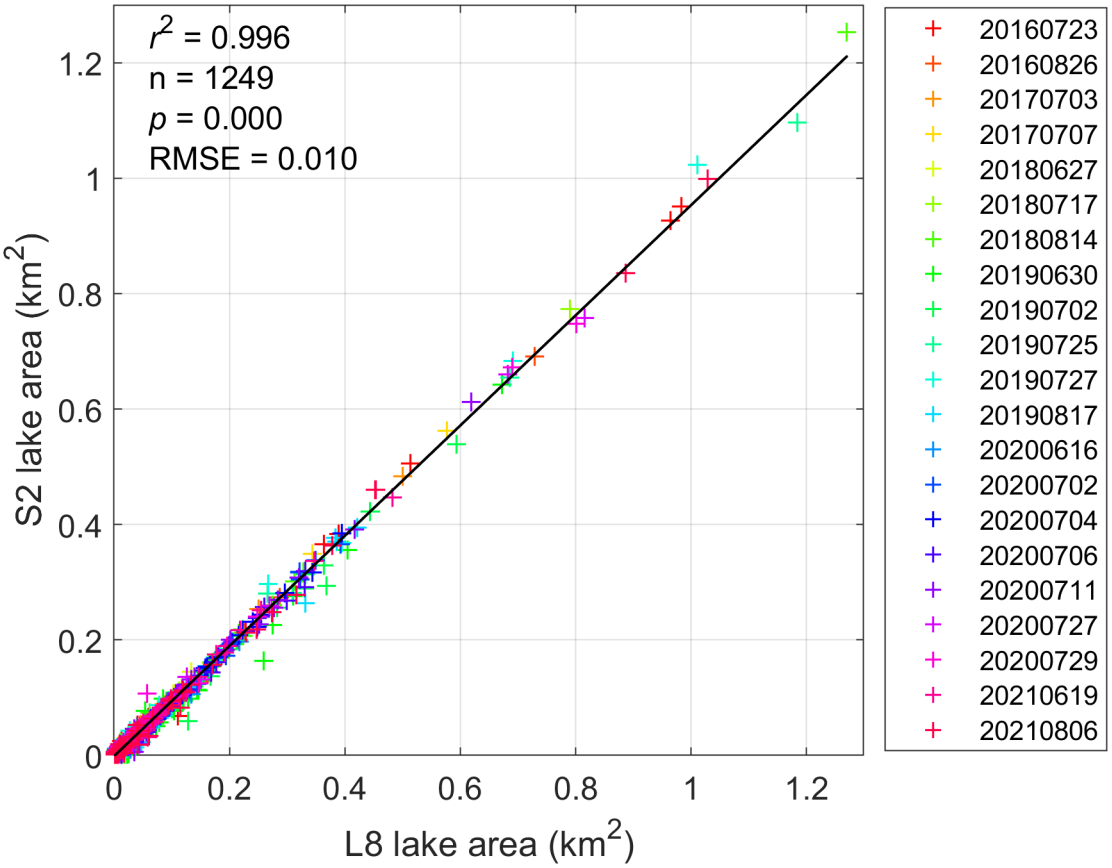

Figure 3.12 Comparison of lake area derived from L8 and S2 images

Comparison of 1249 lake area defined by 21 contemporaneous L8 and S2 images pairs (acquired within < 20 minutes of each other). The black line indicated an ordinary least-squares linear regression, which showed a very good agreement (r^2 = 0.996, p = 0.000) between the L8-derived and S2-derived lake area. The root mean square error (RMSE) is 0.010 km^2 between the two datasets, which is remarkably small.

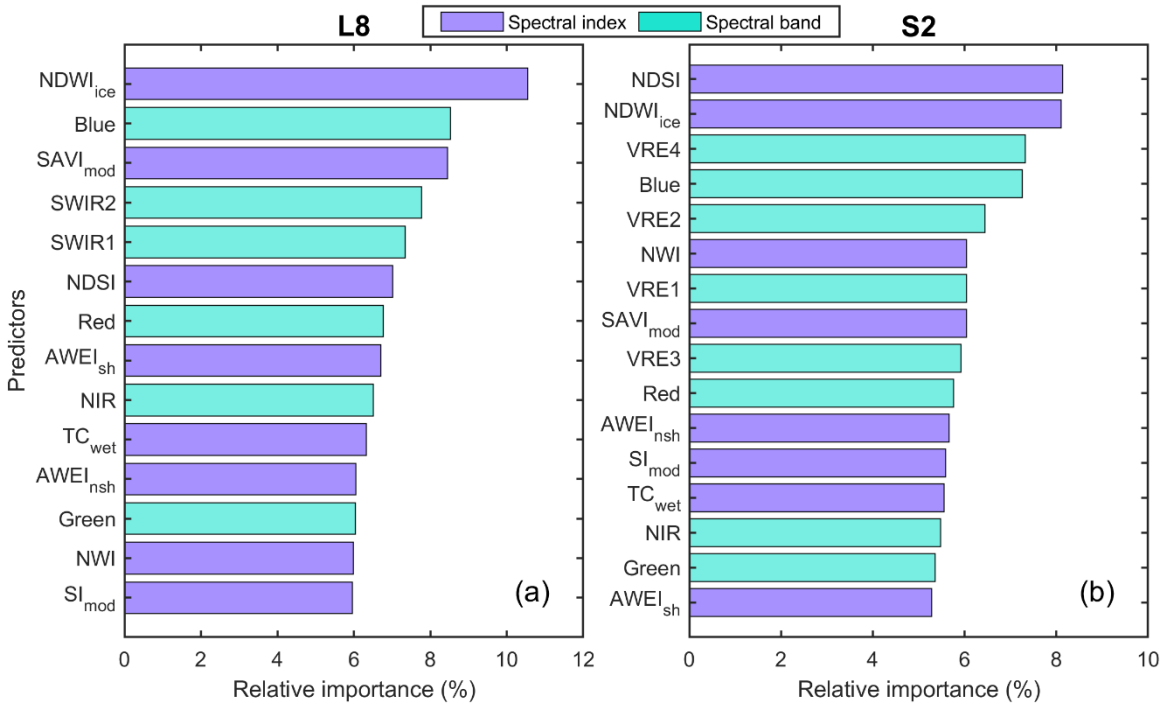

Figure 3.13 Relative importance of the predictors used by the random forest classifier for L8 and S2 satellite imagery datasets.

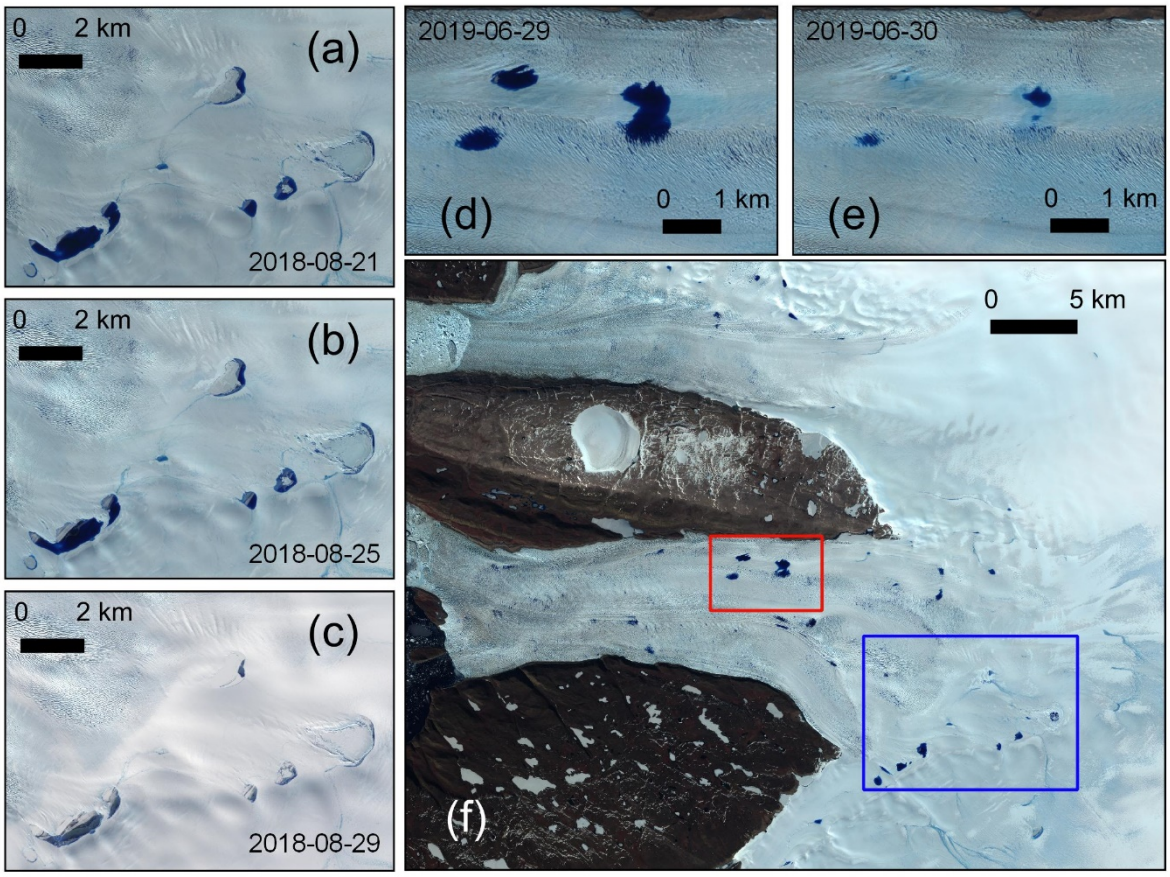

Figure 3.14 Different types of lake disappearing

Examples of the observed surface-refreezing-or/and-buried type SGL (a–b) and discharge type SGL (c–e). Red and blue box in (f) outlines the location of (a–b) and (c–e), respectively. The background in (f) is a Sentinel-2 image acquired on 18 June 2021.

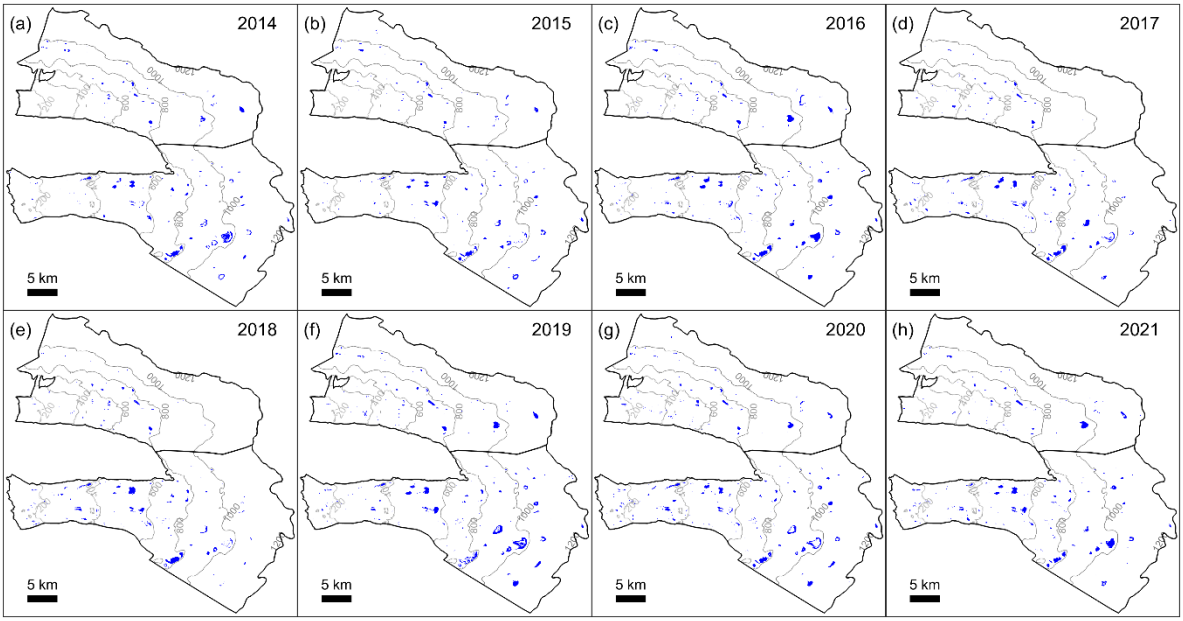

Figure 3.15 Spatial distribution SGLs across the study glaciers from 2014 to 2021
The blue patches represent maximum annual lake extents, and gray lines are the elevation contours derived from ArcticDEM Mosaic (Porter et al., 2018).

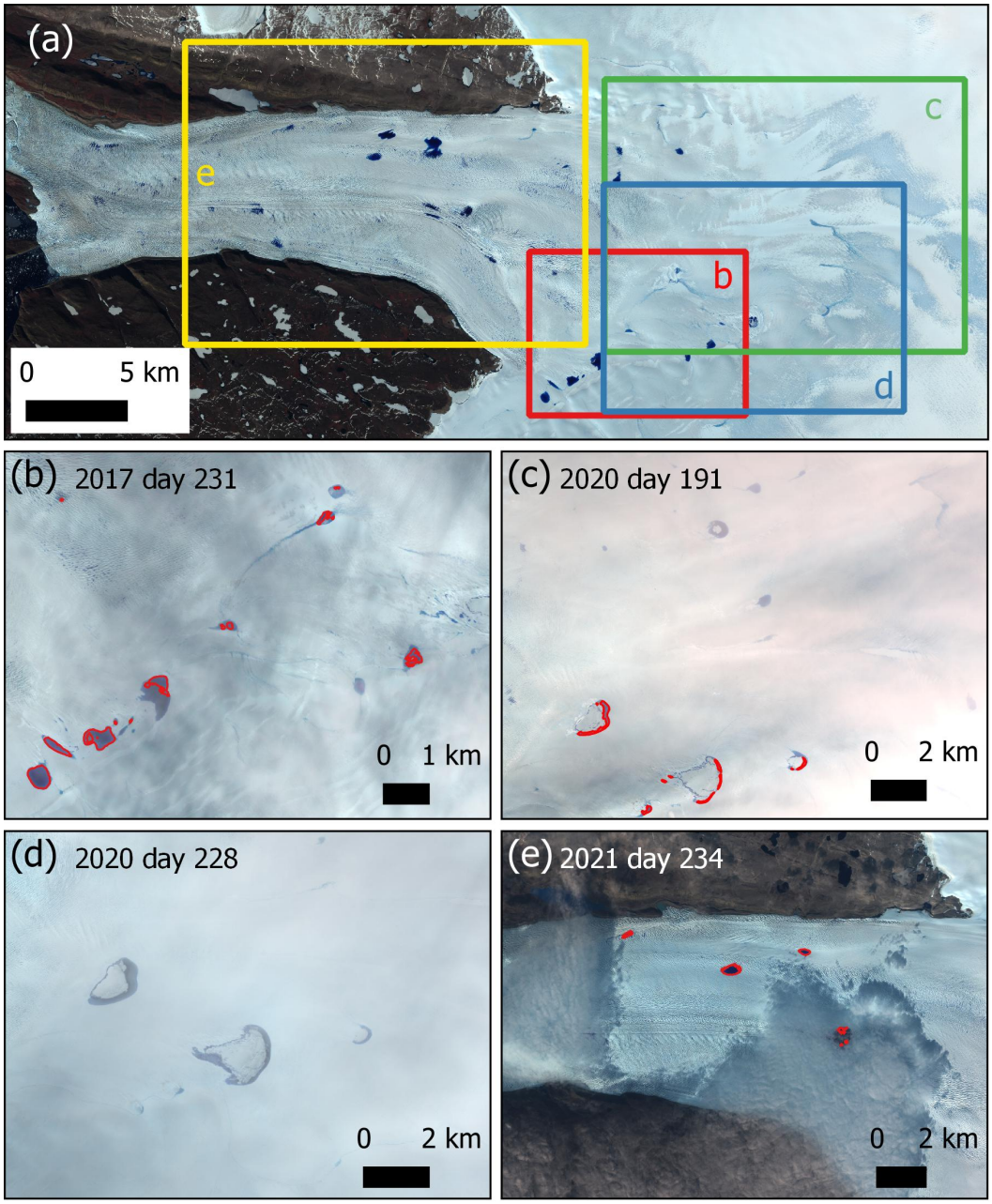

Figure 3.16 Examples of lake detection are hindered by the effect of cloud
(a) is the overview of Heilprin Glacier (from a Sentinel-2 image acquired on 18 June 2021), the colored squares indicate the image extent in (b), (c), (d), and (e). The red closed shapes are water bodies detected by my method.

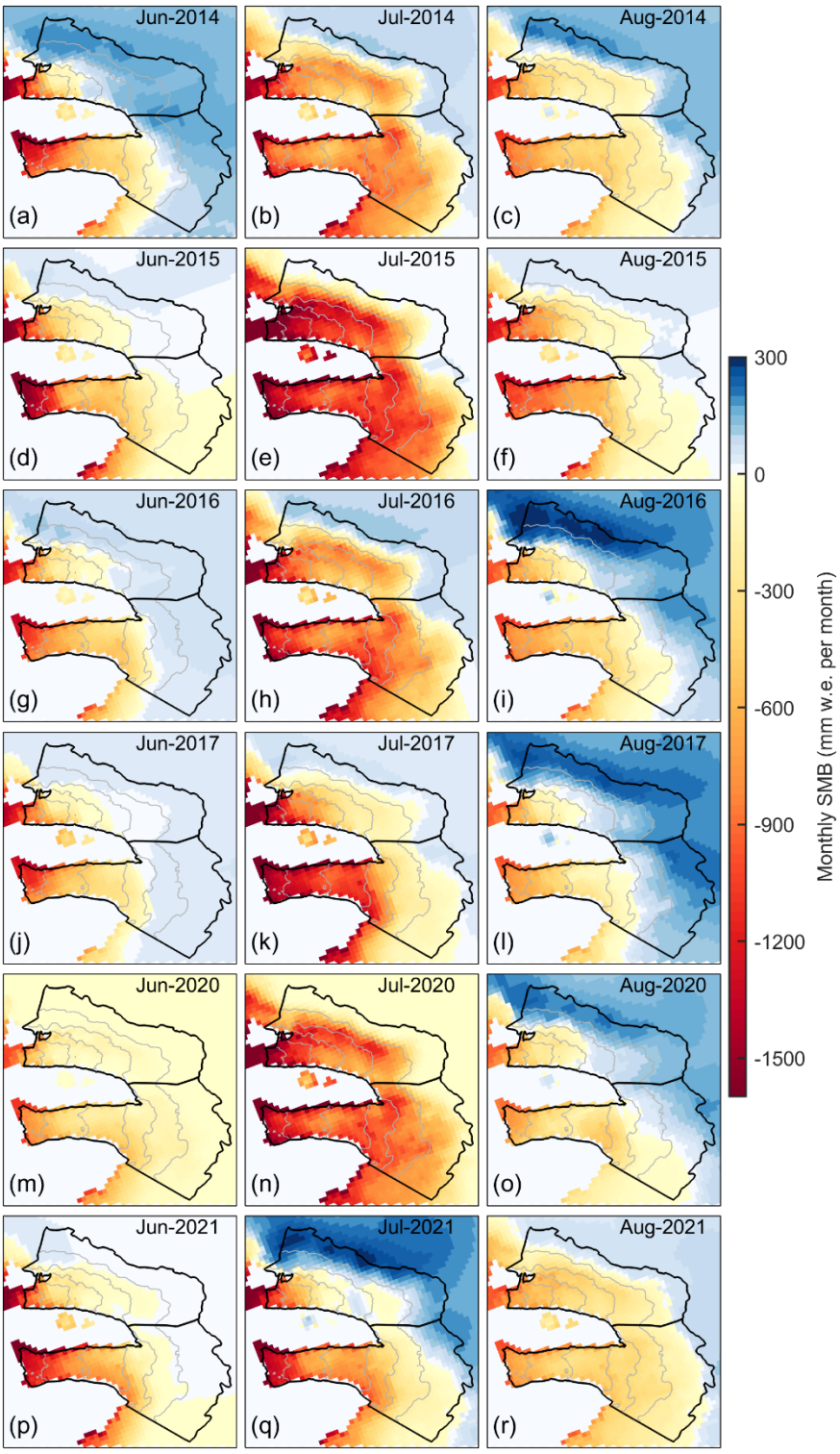

Figure 3.17 Same as Figure 3.11 in the main text, but for the years 2014–2017 and 2020–2021

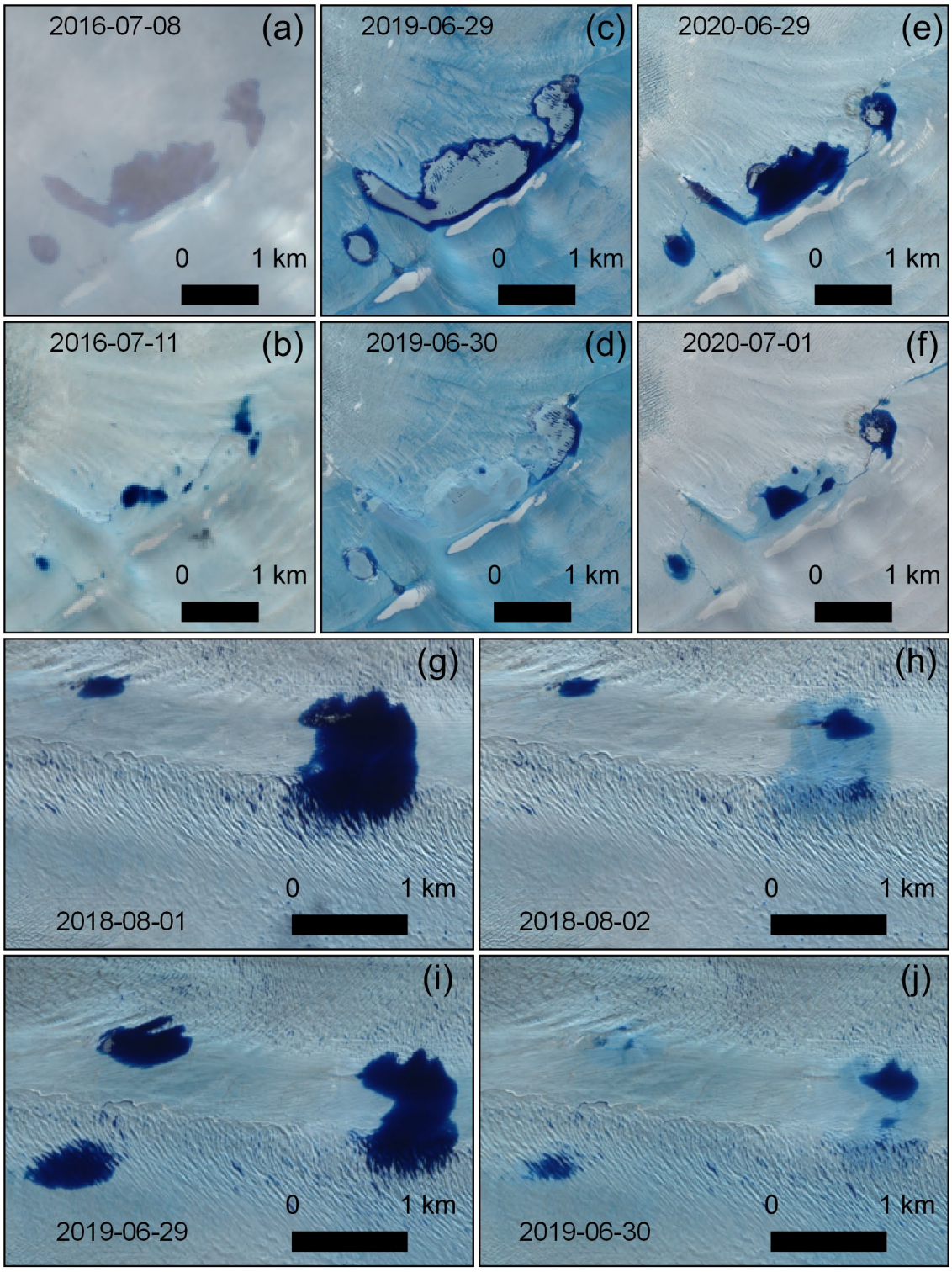

Figure 3.18 Examples of rapid drainage events in Heilprin Glacier.

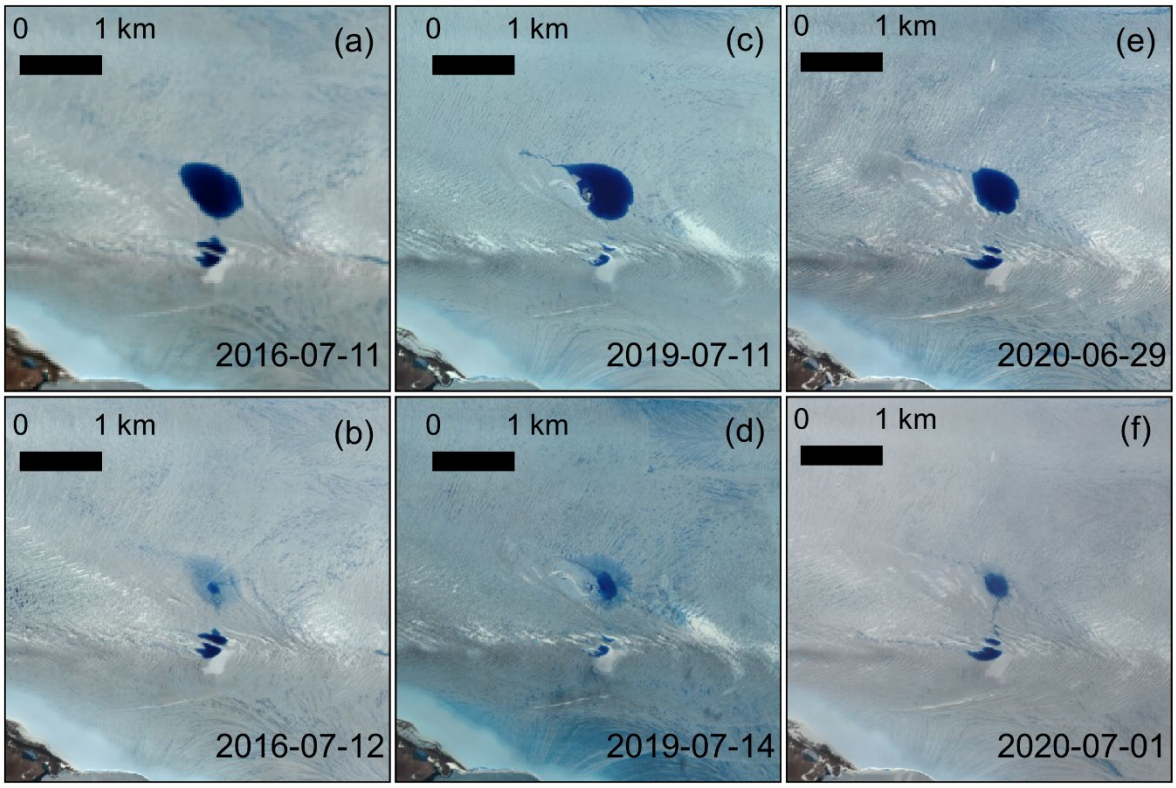

Figure 3.19 Examples of rapid drainage events in Tracy Glacier.

Chapter 4
Conclusions

4.1 Surface elevation changes

I use digital elevation models derived from satellite images and aerial photographs to quantify the surface elevation change of 16 glaciers (15 marine-terminating and 1 land-terminating glaciers) along the coast of Prudhoe Land in northwestern Greenland between 1985 and 2018. The mean rate of the surface elevation change over the studied glaciers was -0.55 ± 0.24 m a^{-1} for 1985–2018. Detailed analysis of the data revealed a clear shift from slight thickening (0.14 ± 0.17 m a^{-1}) in 1985–2001 to rapid thinning (-1.31 ± 0.20 m a^{-1}) in 2001–2018. Glaciers terminating in shallower fjords directly connected to Baffin Bay showed a thinning rate 40% lower than those in the Inglefield Bredning region. Among the glaciers studied, Tracy and Farquhar Glaciers located in Inglefield Bredning thinned most rapidly, at a rate exceeding -9 m a^{-1} in the period 2001–2018.

Since the late 1990s, warming trends were observed in both atmospheric (0.09°C a^{-1} in 1996–2009) and ocean temperatures (0.18°C a^{-1} in 1996–2012), which are the most likely triggers of the regime shift at around 2000. In addition to the climatic influence, ice speed acceleration might have enhanced the observed surface lowering as a result of dynamic thinning. The glacier change showed a substantially large spatial heterogeneity, which is attributed to the glacier geometry and fjord bathymetry. Glaciers terminating in deep fjords in the Inglefield Bredning side have lost greater mass because they are subjected to greater acceleration and are more affected by ocean warming. The data clearly showed a rapid increase in the glacier mass loss in the 21st century for the first time in northwestern Greenland. Together with the drivers of the regime shift identified by the analysis, the study results help our understanding of ongoing glacier changes as well as the future evolution of the Greenland ice sheet.

4.2 Supraglacial lake evolution

I present an intra-annual and inter-annual variations of Greenland surface hydrology across two major marine-terminating glaciers in Inglefield Bredning, northwestern Greenland, employing machine learning method on satellite observations from Landsat-8 and Sentinel-2 optical imageries by using Google Earth Engine platform. I derive fused classification products at 10 m spatial resolution and sub-weekly temporal scale to map supraglacial lake extent in Tracy and Heilprin Glaciers between 2014 and 2021. The machine learning classification is achieved by using a random forest classifier, which is trained using spectral data from manually-selected areas over the studied glaciers. The classifier performs well across the studied glaciers throughout multiple melt seasons, achieving overall accuracy of 98.48% and 98.56% for Landsat-8 and Sentinel-2 imagery dataset, respectively.

For the two studied glaciers, although the studied areas of Heilprin and Tracy glaciers are similar (654 km^2 and 540 km^2), the maximum lake extent on Heilprin glacier (22.84 km^2) was three times greater than that on Tracy glacier (7.60 km^2). For both glaciers, the lakes are relatively small and have a low occurrence frequency in the low elevations (0–400 m). The lakes tend to form larger at middle elevations (400–800 m) and tend to recur at the same location annually. The average lake area is largest in the high elevations (800–1200 m) but the occurrence frequency is not as high as that in the middle elevations. In the seasonal scale, lakes began formation in the early of June, which was followed by substantial increase in area from middle of June. After reaching a maximum, the lake area decreases in August. Due to annual variations in meteorological conditions, the area peaked in different timing every year. In 2016, 2019, and 2020, lake area reached peak values between late June and beginning of July. In 2017 and 2018, however, the peaks were observed later in late July because of cold summer temperature. For the inter-annual variation, peak lake coverage reached 12.41 km^2 for Heilprin Glacier and 4.05 km^2 for Tracy Glacier. However, in 2017 and 2018, the lake extents are anomalously low for both glaciers, and the anomaly low extents are

mainly attributed to the lake undeveloped above 800 m a.s.l.

To investigate a link between supraglacial lake evolution in 2015–2021 and potential metrological and glacial drivers, I compared my lake area dataset with glacier-relevant data including glacier topographic, ice speed and metrological-relevant data including temperature, modelled SMB and snowmelt data. The result revealed that the spatial distribution of SGLs is primarily determined by topography, surface slope and ice speed. Most of the SGLs are developed within the surface depressions and preferentially located away from the large slopes and fast-flow units in the glaciers. The initial spread of supraglacial lakes in the studied glaciers from lower to higher elevations as the temperature reaches above-freezing air temperature. High air temperature or high melt rate do not necessarily correlate with more extensive lake coverage particularly below the elevation of 800 m, because supraglacial lakes may drain extensively when moulin or fractures were opened as the melt season progressed. The maximum inland expansion of supraglacial lakes depends on the ELA, above which supraglacial lakes may not develop because no melting there. The fluctuation of the total areas in 2017 and 2018 is largely attributed to the limed developed lakes in the high elevations due to the cold weather conditions.

4.3 Future perspectives of the study

In the current study, I already have a good knowledge of the elevation change from 1985 to 2018 along the Prudhoe Land, northwestern Greenland, established a robust method to derive supraglacial lake extent from optical satellite imagery, and applied the method in the two major marine-terminating glaciers (Heilprin and Tracy Galciers), investigated the lake evolution there between 2014 and 2021. However, the supraglacial lake evolution in a longer time scale still remains unclear.

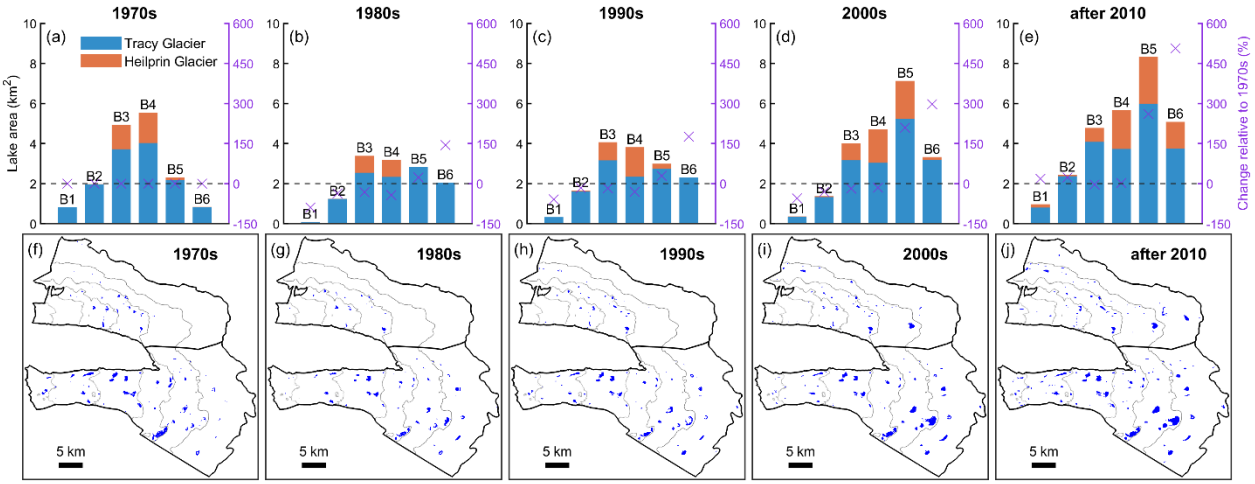

Figure 4.1 Decadal supraglacial lake extent

The lake areas are showed in individual 200 m elevation bands (a–e), and supraglacial lake extent (f–j).

In recent decades, supraglacial lakes experienced significant extent expansion and inland progression after 2000 (Gledhill and Williamson, 2018; Howat et al., 2013), and the lakes are likely to advance more under the current warming scenarios (Ignéczi et al., 2016; Leeson et al., 2015) in the GrIS. However, these studies mainly focus inland part of Greenland and have a coarse spatiotemporal resolution. Under this background, I plan to employ my method to the old Landsat imagery (Landsat 1–4, 5 and 7), date my study to the 1970s in the two marine-terminating glaciers. In the preliminary result (Fig. 4.1), I found a substantial expansion of supraglacial lake extents after 2000, the expansions are mainly concentrated in the area above 800 m a.s.l., and the inland progressions are most significant in Tracy Glacier. I am wondering whether the difference in glacier ice speed, frontal retreating, and thinning have some potential influence on the lake extent expansion and inland advancing. Specifically, Tracy Glacier experienced a 7-fold stronger surface lowering (-3.91 ± 0.13 m a^{-1}) than Heilprin Glacier (-0.51 ± 0.13 m a^{-1}), which means in addition to the atmospheric warming, the significant thinning in Tracy Glacier may also enhance the inland advancing. Further investigation about the feedback between the surface lowering and lake inland advancing is necessary to study.

Meltwater on the surface of the Greenland ice sheet drains into the ice base through

crevasses and moulins, or via rapid supraglacial lake drainages, causing ice flow acceleration due to elevated basal water pressure. Such a speed-up is usually observed at the beginning of the melt season, while ice speed deceases subsequently over the summer despite sustained meltwater input. The deceleration in late summer is generally explained by increasing efficiency of the subglacial drainage system. This general seasonal velocity pattern has been observed in land-terminating glaciers in Greenland (Bartholomew et al., 2010; Sundal et al., 2011), but little is known about detailed response of glacier dynamics to meltwater supply in marine-terminating glaciers. I have already derived a high temporal resolution of lake extent evolution. Based on that, future work might investigate the glacier dynamic response to seasonal variations in meltwater supply.

References

Abdalati, W., W. Krabill, E. Frederick, S. Manizade, C. Martin, J. Sonntag, R. Swift, R. Thomas, W. Wright, and J. Yungel (2001), Outlet glacier and margin elevation changes: Near-coastal thinning of the Greenland ice sheet, *Journal of Geophysical Research: Atmospheres*, *106*(D24), 33729-33741, https://doi.org/10.1029/2001jd900192.

Abermann, J., J. F. Steiner, R. Prinz, M. Wecht, and P. Lisager (2020), The Red Rock ice cliff revisited – six decades of frontal, mass and area changes in the Nunatarssuaq area, Northwest Greenland, *Journal of Glaciology*, *66*(258), 1-10, https://doi.org/10.1017/jog.2020.28.

Aoki, T., S. Matoba, J. Uetake, N. Takeuchi, and H. Motoyama (2014), Field activities of the "Snow Impurity and Glacial Microbe effects on abrupt warming in the Arctic"(SIGMA) Project in Greenland in 2011-2013, *Bulletin of Glaciological Research*, *32*, 3-20, https://doi.org/10.5331/bgr.32.3.

Arthur, J. F., C. R. Stokes, S. S. R. Jamieson, J. R. Carr, and A. A. Leeson (2020), Distribution and seasonal evolution of supraglacial lakes on Shackleton Ice Shelf, East Antarctica, *The Cryosphere*, *14*(11), 4103-4120, http://doi.org/10.5194/tc-14-4103-2020.

Bartholomew, I., P. Nienow, D. Mair, A. Hubbard, M. A. King, and A. Sole (2010), Seasonal evolution of subglacial drainage and acceleration in a Greenland outlet glacier, *Nature Geoscience*, *3*(6), 408-411, http://doi.org/10.1038/ngeo863.

Bartholomew, I., P. Nienow, A. Sole, D. Mair, T. Cowton, and M. A. King (2012), Short-term variability in Greenland Ice Sheet motion forced by time-varying meltwater drainage: Implications for the relationship between subglacial drainage system behavior and ice velocity, *117*(F3), https://doi.org/10.1029/2011JF002220.

Belgiu, M., and L. Drăguţ (2016), Random forest in remote sensing: A review of applications and future directions, *ISPRS Journal of Photogrammetry and Remote Sensing*, *114*, 24-31, https://doi.org/10.1016/j.isprsjprs.2016.01.011.

Benn, D. I., C. R. Warren, and R. H. Mottram (2007), Calving processes and the dynamics of calving glaciers, *Earth-Science Reviews*, *82*(3), 143-179, https://doi.org/10.1016/j.earscirev.2007.02.002.

Benn, D. I., and D. J. Evans (2014), Glaciers & Glaciation, Routledge.

Berthier, E., Y. Arnaud, D. Baratoux, C. Vincent, and F. Rémy (2004), Recent rapid thinning of the "Mer de Glace" glacier derived from satellite optical images, *Geophysical Research Letters*, *31*(17), https://doi.org/10.1029/2004gl020706.

Berthier, E., V. Cabot, C. Vincent, and D. Six (2016), Decadal Region-Wide and Glacier-Wide Mass Balances Derived from Multi-Temporal ASTER Satellite Digital Elevation Models. Validation over the Mont-Blanc Area, *Frontiers in Earth Science*, *4*(63), https://doi.org/10.3389/feart.2016.00063.

Bevan, S. L., A. J. Luckman, D. I. Benn, T. Cowton, and J. Todd (2019), Impact of warming shelf waters on ice mélange and terminus retreat at a large SE Greenland glacier, *The*

Cryosphere, *13*(9), 2303-2315, https://doi.org/10.5194/tc-13-2303-2019.

Bjørk, A. A., L. M. Kruse, and P. B. Michaelsen (2015), Brief communication: Getting Greenland's glaciers right – a new data set of all official Greenlandic glacier names, *The Cryosphere*, *9*(6), 2215-2218, http://doi.org/10.5194/tc-9-2215-2015.

Black, T. E., and I. Joughin (2022), Multi-decadal retreat of marine-terminating outlet glaciers in northwest and central-west Greenland, *The Cryosphere*, *16*(3), 807-824, http://doi.org/10.5194/tc-16-807-2022.

Bolch, T., L. Sandberg Sørensen, S. B. Simonsen, N. Mölg, H. Machguth, P. Rastner, and F. Paul (2013), Mass loss of Greenland's glaciers and ice caps 2003–2008 revealed from ICESat laser altimetry data, *Geophysical Research Letters*, *40*(5), 875-881, https://doi.org/10.1002/grl.50270.

Box, J. E., and K. Ski (2007), Remote sounding of Greenland supraglacial melt lakes: implications for subglacial hydraulics, *Journal of Glaciology*, *53*(181), 257-265, http://doi.org/10.3189/172756507782202883.

Box, J. E., L. Yang, D. H. Bromwich, and L.-S. Bai (2009), Greenland Ice Sheet Surface Air Temperature Variability: 1840–2007*, *Journal of Climate*, *22*(14), 4029-4049, https://doi.org/10.1175/2009JCLI2816.1.

Breiman, L. (2001), Random Forests, *Machine Learning*, *45*(1), 5-32, http://doi.org/10.1023/A:1010933404324.

Bunce, C., J. R. Carr, P. W. Nienow, N. Ross, and R. Killick (2018), Ice front change of marine-terminating outlet glaciers in northwest and southeast Greenland during the 21st century, *Journal of Glaciology*, *64*(246), 523-535, http://doi.org/10.1017/jog.2018.44.

Carr, J. R., C. R. Stokes, and A. Vieli (2013a), Recent progress in understanding marine-terminating Arctic outlet glacier response to climatic and oceanic forcing:Twenty years of rapid change, *Progress in Physical Geography: Earth and Environment*, *37*(4), 436-467, https://doi.org/10.1177/0309133313483163.

Carr, J. R., A. Vieli, and C. Stokes (2013b), Influence of sea ice decline, atmospheric warming, and glacier width on marine-terminating outlet glacier behavior in northwest Greenland at seasonal to interannual timescales, *Journal of Geophysical Research: Earth Surface*, *118*(3), 1210-1226, https://doi.org/10.1002/jgrf.20088.

Catania, G. A., L. A. Stearns, T. A. Moon, E. M. Enderlin, and R. H. Jackson (2020), Future Evolution of Greenland's Marine-Terminating Outlet Glaciers, *Journal of Geophysical Research: Earth Surface*, *125*(2), e2018JF004873, https://doi.org/10.1029/2018jf004873.

Chan, J. C.-W., and D. Paelinckx (2008), Evaluation of Random Forest and Adaboost tree-based ensemble classification and spectral band selection for ecotope mapping using airborne hyperspectral imagery, *Remote Sensing of Environment*, *112*(6), 2999-3011, https://doi.org/10.1016/j.rse.2008.02.011.

Choi, Y., M. Morlighem, E. Rignot, and M. Wood (2021), Ice dynamics will remain a primary driver of Greenland ice sheet mass loss over the next century, *Communications Earth & Environment*, *2*(1), 26, http://doi.org/10.1038/s43247-021-00092-z.

Christoffersen, P., M. Bougamont, A. Hubbard, S. H. Doyle, S. Grigsby, and R. Pettersson

(2018), Cascading lake drainage on the Greenland Ice Sheet triggered by tensile shock and fracture, *Nature Communications*, *9*(1), 1064, http://doi.org/10.1038/s41467-018-03420-8.

Chu, V. W. (2014), Greenland ice sheet hydrology:A review, *Progress in Physical Geography: Earth and Environment*, *38*(1), 19-54, http://doi.org/10.1177/0309133313507075.

Chudley, T. R., P. Christoffersen, S. H. Doyle, M. Bougamont, C. M. Schoonman, B. Hubbard, and M. R. James (2019), Supraglacial lake drainage at a fast-flowing Greenlandic outlet glacier, *116*(51), 25468-25477, http://doi.org/10.1073/pnas.1913685116.

Cogley, J. G., A. Arendt, A. Bauder, R. Braithwaite, R. Hock, P. Jansson, G. Kaser, M. Moller, L. Nicholson, and L. Rasmussen (2010), Glossary of glacier mass balance and related terms, *(IHP-VII Technical Documents in Hydrology No. 86, IACS Contribution No. 2) UNESCO–International Hydrological Programme*.

Colgan, W., H. Rajaram, W. Abdalati, C. McCutchan, R. Mottram, M. S. Moussavi, and S. Grigsby (2016), Glacier crevasses: Observations, models, and mass balance implications, *54*(1), 119-161, https://doi.org/10.1002/2015RG000504.

Cook, A. J., L. Copland, B. P. Y. Noël, C. R. Stokes, M. J. Bentley, M. J. Sharp, R. G. Bingham, and M. R. van den Broeke (2019), Atmospheric forcing of rapid marine-terminating glacier retreat in the Canadian Arctic Archipelago, *Science Advances*, *5*(3), eaau8507, https://doi.org/10.1126/sciadv.aau8507.

Crist, E. P., and R. C. Cicone (1984), A Physically-Based Transformation of Thematic Mapper Data---The TM Tasseled Cap, *IEEE Transactions on Geoscience and Remote Sensing*, *GE-22*(3), 256-263, http://doi.org/10.1109/TGRS.1984.350619.

Csatho, B. M., A. F. Schenk, C. J. van der Veen, G. Babonis, K. Duncan, S. Rezvanbehbahani, M. R. van den Broeke, S. B. Simonsen, S. Nagarajan, and J. H. van Angelen (2014), Laser altimetry reveals complex pattern of Greenland Ice Sheet dynamics, *Proceedings of the National Academy of Sciences*, *111*(52), 18478-18483, https://doi.org/10.1073/pnas.1411680112.

Cuffey, K. M., and W. S. B. Paterson (2010), *The physics of glaciers*, Academic Press.

Das, S. B., I. Joughin, M. D. Behn, I. M. Howat, M. A. King, D. Lizarralde, and M. P. Bhatia (2008), Fracture Propagation to the Base of the Greenland Ice Sheet During Supraglacial Lake Drainage, *320*(5877), 778-781, https://doi.org/10.1126/science.1153360.

Dawes, P. R., and D. van As (2010), An advancing glacier in a recessive ice regime: Berlingske Bræ, North-West Greenland, *Geol. Surv. Den. Greenl. Bull*, *20*, 79-82, https://doi.org/10.34194/geusb.v20.4986.

Dell, R., N. Arnold, I. Willis, A. Banwell, A. Williamson, H. Pritchard, and A. Orr (2020), Lateral meltwater transfer across an Antarctic ice shelf, *The Cryosphere*, *14*(7), 2313-2330, http://doi.org/10.5194/tc-14-2313-2020.

Dell, R. L., A. F. Banwell, I. C. Willis, N. S. Arnold, A. R. W. Halberstadt, T. R. Chudley, and H. D. Pritchard (2021), Supervised classification of slush and ponded water on

Antarctic ice shelves using Landsat 8 imagery, *Journal of Glaciology*, 1-14, http://doi.org/10.1017/jog.2021.114.

Denisko, D., and M. M. Hoffman (2018), Classification and interaction in random forests, *Proceedings of the National Academy of Sciences*, *115*(8), 1690-1692, http://doi.org/10.1073/pnas.1800256115.

Dirscherl, M., A. J. Dietz, C. Kneisel, and C. Kuenzer (2020), Automated Mapping of Antarctic Supraglacial Lakes Using a Machine Learning Approach, *Remote Sensing*, *12*(7), 1203.

Dirscherl, M. C., A. J. Dietz, and C. Kuenzer (2021), Seasonal evolution of Antarctic supraglacial lakes in 2015–2021 and links to environmental controls, *The Cryosphere*, *15*(11), 5205-5226, http://doi.org/10.5194/tc-15-5205-2021.

Doyle, S. H., A. L. Hubbard, C. F. Dow, G. A. Jones, A. Fitzpatrick, A. Gusmeroli, B. Kulessa, K. Lindback, R. Pettersson, and J. E. Box (2013), Ice tectonic deformation during the rapid in situ drainage of a supraglacial lake on the Greenland Ice Sheet, *The Cryosphere*, *7*(1), 129-140, http://doi.org/10.5194/tc-7-129-2013.

Dozier, J. (1989), Spectral signature of alpine snow cover from the landsat thematic mapper, *Remote Sensing of Environment*, *28*, 9-22, https://doi.org/10.1016/0034-4257(89)90101-6.

Echelmeyer, K., T. S. Clarke, and W. D. Harrison (1991), Surficial glaciology of Jakobshavns Isbræ, West Greenland: Part I. Surface morphology, *Journal of Glaciology*, *37*(127), 368-382, http://doi.org/10.3189/S0022143000005803.

Enderlin, E. M., I. M. Howat, S. Jeong, M.-J. Noh, J. H. van Angelen, and M. R. van den Broeke (2014), An improved mass budget for the Greenland ice sheet, *Geophysical Research Letters*, *41*(3), 866-872, https://doi.org/10.1002/2013gl059010.

Enderlin, E. M., I. M. Howat, and A. Vieli (2013), High sensitivity of tidewater outlet glacier dynamics to shape, *The Cryosphere*, *7*(3), 1007-1015, https://doi.org/10.5194/tc-7-1007-2013.

Fahrner, D., J. M. Lea, S. Brough, D. W. F. Mair, and J. Abermann (2021), Linear response of the Greenland ice sheet's tidewater glacier terminus positions to climate, *Journal of Glaciology*, *67*(262), 193-203, http://doi.org/10.1017/jog.2021.13.

Felikson, D., et al. (2017), Inland thinning on the Greenland ice sheet controlled by outlet glacier geometry, *Nature Geoscience*, *10*(5), 366-369, http://doi.org/10.1038/ngeo2934.

Feng, D. (2012), A New Method for Fast Information Extraction of Water Bodies Using Remotely Sensed Data, *Remote Sensing Technology and Application*, *24*, 167-171.

Feyisa, G. L., H. Meilby, R. Fensholt, and S. R. Proud (2014), Automated Water Extraction Index: A new technique for surface water mapping using Landsat imagery, *Remote Sensing of Environment*, *140*, 23-35, https://doi.org/10.1016/j.rse.2013.08.029.

Fischer, M. P., and R. D. Powell (1998), A simple model for the influence of push-morainal banks on the calving and stability of glacial tidewater termini, *Journal of Glaciology*, *44*(146), 31-41, http://doi.org/10.3189/S002214300000232X.

Fitzpatrick, A. A. W., A. L. Hubbard, J. E. Box, D. J. Quincey, D. van As, A. P. B. Mikkelsen, S. H. Doyle, C. F. Dow, B. Hasholt, and G. A. Jones (2014), A decade

(2002–2012) of supraglacial lake volume estimates across Russell Glacier, West Greenland, *The Cryosphere*, *8*(1), 107-121, http://doi.org/10.5194/tc-8-107-2014.

Fujisada, H., G. B. Bailey, G. G. Kelly, S. Hara, and M. J. Abrams (2005), ASTER DEM performance, *IEEE Transactions on Geoscience and Remote Sensing*, *43*(12), 2707-2714, https://doi.org/10.1109/TGRS.2005.847924.

Gardelle, J., E. Berthier, Y. Arnaud, and A. Kääb (2013), Region-wide glacier mass balances over the Pamir-Karakoram-Himalaya during 1999–2011, *The Cryosphere*, *7*(4), 1263-1286, https://doi.org/10.5194/tc-7-1263-2013.

Gardner, A. S., et al. (2013), A Reconciled Estimate of Glacier Contributions to Sea Level Rise: 2003 to 2009, *Science*, *340*(6134), 852-857, https://doi.org/10.1126/science.1234532.

Gardner, A. S., G. Moholdt, B. Wouters, G. J. Wolken, D. O. Burgess, M. J. Sharp, J. G. Cogley, C. Braun, and C. Labine (2011), Sharply increased mass loss from glaciers and ice caps in the Canadian Arctic Archipelago, *Nature*, *473*(7347), 357-360, http://doi.org/10.1038/nature10089.

Girod, L., C. Nuth, A. Kääb, R. McNabb, and O. Galland (2017), MMASTER: improved ASTER DEMs for elevation change monitoring, *Remote Sensing*, *9*(7), 704, https://doi.org/10.3390/rs9070704.

Gledhill, L. A., and A. G. Williamson (2018), Inland advance of supraglacial lakes in north-west Greenland under recent climatic warming, *Annals of Glaciology*, *59*(76pt1), 66-82.

Grotzinger, J., and T. H. Jordan (2014), *Understanding Earth: Seventh Edition*, Macmillan Learning.

Halberstadt, A. R. W., C. J. Gleason, M. S. Moussavi, A. Pope, L. D. Trusel, and R. M. DeConto (2020), Antarctic Supraglacial Lake Identification Using Landsat-8 Image Classification, *Remote Sensing*, *12*(8), 1327.

Hall, D. K., G. A. Riggs, and V. V. Salomonson (1995), Development of methods for mapping global snow cover using moderate resolution imaging spectroradiometer data, *Remote Sensing of Environment*, *54*(2), 127-140, https://doi.org/10.1016/0034-4257(95)00137-P.

Hanna, E., X. Fettweis, S. H. Mernild, J. Cappelen, M. H. Ribergaard, C. A. Shuman, K. Steffen, L. Wood, and T. L. Mote (2014), Atmospheric and oceanic climate forcing of the exceptional Greenland ice sheet surface melt in summer 2012, *International Journal of Climatology*, *34*(4), 1022-1037, https://doi.org/10.1002/joc.3743.

Hanna, E., et al. (2020), Mass balance of the ice sheets and glaciers – Progress since AR5 and challenges, *Earth-Science Reviews*, *201*, 102976, https://doi.org/10.1016/j.earscirev.2019.102976.

Hill, E. A., J. R. Carr, and C. R. Stokes (2017), A Review of Recent Changes in Major Marine-Terminating Outlet Glaciers in Northern Greenland, *Frontiers in Earth Science*, *4*(111), https://doi.org/10.3389/feart.2016.00111.

Hill, E. A., J. R. Carr, C. R. Stokes, and G. H. Gudmundsson (2018), Dynamic changes in outlet glaciers in northern Greenland from 1948 to 2015, *The Cryosphere*, *12*(10), 3243-

3263, http://doi.org/10.5194/tc-12-3243-2018.

Hirano, A., R. Welch, and H. Lang (2003), Mapping from ASTER stereo image data: DEM validation and accuracy assessment, *ISPRS Journal of Photogrammetry and Remote Sensing*, *57*(5), 356-370, https://doi.org/10.1016/S0924-2716(02)00164-8.

Holland, D. M., R. H. Thomas, B. de Young, M. H. Ribergaard, and B. Lyberth (2008), Acceleration of Jakobshavn Isbræ triggered by warm subsurface ocean waters, *Nature Geoscience*, *1*(10), 659-664, https://doi.org/10.1038/ngeo316.

Howat, I., S. De la Pena, J. Van Angelen, J. Lenaerts, and M. J. T. C. Van den Broeke (2013), Brief Communication" Expansion of meltwater lakes on the Greenland ice sheet", *7*(1), 201-204.

Howat, I. M., I. Joughin, M. Fahnestock, B. E. Smith, and T. A. Scambos (2008), Synchronous retreat and acceleration of southeast Greenland outlet glaciers 2000–06: ice dynamics and coupling to climate, *Journal of Glaciology*, *54*(187), 646-660, http://doi.org/10.3189/002214308786570908.

Howat, I. M., I. Joughin, S. Tulaczyk, and S. Gogineni (2005), Rapid retreat and acceleration of Helheim Glacier, east Greenland, *Geophysical Research Letters*, *32*(22), https://doi.org/10.1029/2005GL024737.

Howat, I. M., A. Negrete, and B. E. Smith (2014), The Greenland Ice Mapping Project (GIMP) land classification and surface elevation data sets, *The Cryosphere*, *8*(4), 1509-1518, https://doi.org/10.5194/tc-8-1509-2014.

Huber, J., R. McNabb, and M. Zemp (2020), Elevation Changes of West-Central Greenland Glaciers From 1985 to 2012 From Remote Sensing, *Frontiers in Earth Science*, *8*(35), https://doi.org/10.3389/feart.2020.00035.

Huete, A. R. (1988), A soil-adjusted vegetation index (SAVI), *Remote Sensing of Environment*, *25*(3), 295-309, https://doi.org/10.1016/0034-4257(88)90106-X.

Ignéczi, Á., A. J. Sole, S. J. Livingstone, A. A. Leeson, X. Fettweis, N. Selmes, N. Gourmelen, and K. Briggs (2016), Northeast sector of the Greenland Ice Sheet to undergo the greatest inland expansion of supraglacial lakes during the 21st century, *43*(18), 9729-9738, https://doi.org/10.1002/2016GL070338.

Johansson, A. M., P. Jansson, and I. A. Brown (2013), Spatial and temporal variations in lakes on the Greenland Ice Sheet, *Journal of hydrology*, *476*, 314-320.

Joughin, I., W. Abdalati, and M. Fahnestock (2004), Large fluctuations in speed on Greenland's Jakobshavn Isbræ glacier, *Nature*, *432*(7017), 608-610, http://doi.org/10.1038/nature03130.

Kanna, N., S. Sugiyama, Y. Ohashi, D. Sakakibara, Y. Fukamachi, and D. Nomura (2018), Upwelling of Macronutrients and Dissolved Inorganic Carbon by a Subglacial Freshwater Driven Plume in Bowdoin Fjord, Northwestern Greenland, *Journal of Geophysical Research: Biogeosciences*, *123*(5), 1666-1682, https://doi.org/10.1029/2017jg004248.

Khan, S. A., et al. (2014), Sustained mass loss of the northeast Greenland ice sheet triggered by regional warming, *Nature Climate Change*, *4*(4), 292-299, https://doi.org/10.1038/nclimate2161.

Khan, S. A., J. Wahr, M. Bevis, I. Velicogna, and E. Kendrick (2010), Spread of ice mass loss into northwest Greenland observed by GRACE and GPS, *Geophysical Research Letters*, *37*(6), https://doi.org/10.1029/2010gl042460.

King, M. D., I. M. Howat, S. G. Candela, M. J. Noh, S. Jeong, B. P. Y. Noël, M. R. van den Broeke, B. Wouters, and A. Negrete (2020), Dynamic ice loss from the Greenland Ice Sheet driven by sustained glacier retreat, *Communications Earth & Environment*, *1*(1), 1, http://doi.org/10.1038/s43247-020-0001-2.

Kirkbride, M. P., and C. R. Warren (1999), Tasman Glacier, New Zealand: 20th-century thinning and predicted calving retreat, *Global and Planetary Change*, *22*(1), 11-28, https://doi.org/10.1016/S0921-8181(99)00021-1.

Kjær, K. H., et al. (2012), Aerial Photographs Reveal Late–20th-Century Dynamic Ice Loss in Northwestern Greenland, *Science*, *337*(6094), 569-573, https://doi.org/10.1126/science.1220614.

Kjeldsen, K. K., et al. (2015), Spatial and temporal distribution of mass loss from the Greenland Ice Sheet since AD 1900, *Nature*, *528*(7582), 396-400, https://doi.org/10.1038/nature16183.

Koenig, L. S., et al. (2015), Wintertime storage of water in buried supraglacial lakes across the Greenland Ice Sheet, *The Cryosphere*, *9*(4), 1333-1342, http://doi.org/10.5194/tc-9-1333-2015.

Korsgaard, N. J., C. Nuth, S. A. Khan, K. K. Kjeldsen, A. A. Bjørk, A. Schomacker, and K. H. Kjær (2016), Digital elevation model and orthophotographs of Greenland based on aerial photographs from 1978–1987, *Scientific Data*, *3*(1), 160032, https://doi.org/10.1038/sdata.2016.32.

Krabill, W., W. Abdalati, E. Frederick, S. Manizade, C. Martin, J. Sonntag, R. Swift, R. Thomas, W. Wright, and J. Yungel (2000), Greenland Ice Sheet: High-Elevation Balance and Peripheral Thinning, *Science*, *289*(5478), 428-430, https://doi.org/10.1126/science.289.5478.428.

Krabill, W., et al. (2004), Greenland Ice Sheet: Increased coastal thinning, *Geophysical Research Letters*, *31*(24), https://doi.org/10.1029/2004gl021533.

Landis, J. R., and G. G. Koch (1977), The Measurement of Observer Agreement for Categorical Data, *Biometrics*, *33*(1), 159-174, http://doi.org/10.2307/2529310.

Leeson, A. A., A. Shepherd, K. Briggs, I. Howat, X. Fettweis, M. Morlighem, and E. Rignot (2015), Supraglacial lakes on the Greenland ice sheet advance inland under warming climate, *Nature Climate Change*, *5*(1), 51-55, http://doi.org/10.1038/nclimate2463.

Lenaerts, J. T. M., B. Medley, M. R. van den Broeke, and B. Wouters (2019), Observing and Modeling Ice Sheet Surface Mass Balance, *Reviews of Geophysics*, *57*(2), 376-420, https://doi.org/10.1029/2018RG000622.

Li, H., L. Xu, H. Shen, and L. Zhang (2016), A general variational framework considering cast shadows for the topographic correction of remote sensing imagery, *ISPRS Journal of Photogrammetry and Remote Sensing*, *117*, 161-171, https://doi.org/10.1016/j.isprsjprs.2016.03.021.

Lüthje, M., L. Pedersen, N. Reeh, and W. Greuell (2006), Modelling the evolution of

supraglacial lakes on the West Greenland ice-sheet margin, *Journal of Glaciology*, *52*(179), 608-618.

Macdonald, G., Banwell, A., & MacAyeal, D. (2018). Seasonal evolution of supraglacial lakes on a floating ice tongue, Petermann Glacier, Greenland. *Annals of Glaciology*, 59(76pt1), 56-65. http://doi.org/10.1017/aog.2018.9

Mankoff, K. D., et al. (2019), Greenland Ice Sheet solid ice discharge from 1986 through 2017, *Earth Syst. Sci. Data*, *11*(2), 769-786, http://doi.org/10.5194/essd-11-769-2019.

Marcer, M., P. A. Stentoft, E. Bjerre, E. Cimoli, A. Bjørk, L. Stenseng, and H. Machguth (2017), Three Decades of Volume Change of a Small Greenlandic Glacier Using Ground Penetrating Radar, Structure from Motion, and Aerial Photogrammetry, *Arctic, Antarctic, and Alpine Research*, *49*(3), 411-425, https://doi.org/10.1657/AAAR0016-049.

McFadden, E. M., I. M. Howat, I. Joughin, B. E. Smith, and Y. Ahn (2011), Changes in the dynamics of marine terminating outlet glaciers in west Greenland (2000–2009), *116*(F2), https://doi.org/10.1029/2010JF001757.

Meier, M. F., and A. Post (1987), Fast tidewater glaciers, *Journal of Geophysical Research: Solid Earth*, *92*(B9), 9051-9058, https://doi.org/10.1029/JB092iB09p09051.

Mernild, S. H., T. L. Mote, and G. E. Liston (2011), Greenland ice sheet surface melt extent and trends: 1960–2010, *Journal of Glaciology*, *57*(204), 621-628, https://doi.org/10.3189/002214311797409712.

Moon, T., I. Joughin, B. Smith, and I. Howat (2012), 21st-Century Evolution of Greenland Outlet Glacier Velocities, *Science*, *336*(6081), 576-578, https://doi.org/10.1126/science.1219985.

Moon, T., I. Joughin, B. Smith, M. R. van den Broeke, W. J. van de Berg, B. Noël, and M. Usher (2014), Distinct patterns of seasonal Greenland glacier velocity, *Geophysical research letters*, *41*(20), 7209-7216, https://doi.org/10.1002/2014GL061836.

Morlighem, M., et al. (2017), BedMachine v3: Complete Bed Topography and Ocean Bathymetry Mapping of Greenland From Multibeam Echo Sounding Combined With Mass Conservation, *Geophysical Research Letters*, *44*(21), 11,051-011,061, https://doi.org/10.1002/2017gl074954.

Mortimer, C. A., M. Sharp, and W. Van Wychen (2018), Influence of recent warming and ice dynamics on glacier surface elevations in the Canadian High Arctic, 1995–2014, *Journal of Glaciology*, *64*(245), 450-464, https://doi.org/10.1017/jog.2018.37.

Motyka, R. J., W. P. Dryer, J. Amundson, M. Truffer, and M. Fahnestock (2013), Rapid submarine melting driven by subglacial discharge, LeConte Glacier, Alaska, *Geophysical Research Letters*, *40*(19), 5153-5158, https://doi.org/10.1002/grl.51011.

Motyka, R. J., S. O'Neel, C. L. Connor, and K. A. Echelmeyer (2003), Twentieth century thinning of Mendenhall Glacier, Alaska, and its relationship to climate, lake calving, and glacier run-off, *Global and Planetary Change*, *35*(1), 93-112, https://doi.org/10.1016/S0921-8181(02)00138-8.

Mouginot, J., A. A. Bjørk, R. Millan, B. Scheuchl, and E. Rignot (2018), Insights on the Surge Behavior of Storstrømmen and L. Bistrup Bræ, Northeast Greenland, Over the

Last Century, *Geophysical Research Letters*, *45*(20), 11,197-111,205, https://doi.org/10.1029/2018GL079052.

Mouginot, J., and E. Rignot (2019), Glacier catchments/basins for the Greenland Ice Sheet, *UC Irvine Dash: Irvine, CA, USA*.

Mouginot, J., E. Rignot, A. A. Bjørk, M. van den Broeke, R. Millan, M. Morlighem, B. Noël, B. Scheuchl, and M. Wood (2019), Forty-six years of Greenland Ice Sheet mass balance from 1972 to 2018, *Proceedings of the National Academy of Sciences*, *116*(19), 9239-9244, https://doi.org/10.1073/pnas.1904242116.

Moussavi, M., A. Pope, A. R. W. Halberstadt, L. D. Trusel, L. Cioffi, and W. Abdalati (2020), Antarctic Supraglacial Lake Detection Using Landsat 8 and Sentinel-2 Imagery: Towards Continental Generation of Lake Volumes, *Remote Sensing*, *12*(1), 134.

Nghiem, S. V., D. K. Hall, T. L. Mote, M. Tedesco, M. R. Albert, K. Keegan, C. A. Shuman, N. E. DiGirolamo, and G. Neumann (2012), The extreme melt across the Greenland ice sheet in 2012, *Geophysical Research Letters*, *39*(20), https://doi.org/10.1029/2012gl053611.

Noël, B., W. J. v. d. Berg, S. Lhermitte, and M. R. v. d. Broeke (2019), Rapid ablation zone expansion amplifies north Greenland mass loss, *Science Advances*, *5*(9), eaaw0123, http://doi.org/10.1126/sciadv.aaw0123.

Noël, B., et al. (2018), Modelling the climate and surface mass balance of polar ice sheets using RACMO2 – Part 1: Greenland (1958–2016), *The Cryosphere*, *12*(3), 811-831, http://doi.org/10.5194/tc-12-811-2018.

Nuth, C., and A. Kääb (2011), Co-registration and bias corrections of satellite elevation data sets for quantifying glacier thickness change, *The Cryosphere*, *5*(1), 271-290, https://doi.org/10.5194/tc-5-271-2011.

Ohashi, Y., S. Aoki, Y. Matsumura, S. Sugiyama, N. Kanna, and D. Sakakibara (2020), Vertical distribution of water mass properties under the influence of subglacial discharge in Bowdoin Fjord, northwestern Greenland, *Ocean Sci.*, *16*(3), 545-564, https://doi.org/10.5194/os-16-545-2020.

Pal, M. (2005), Random forest classifier for remote sensing classification, *International Journal of Remote Sensing*, *26*(1), 217-222, http://doi.org/10.1080/01431160412331269698.

Palmer, S., A. Shepherd, P. Nienow, and I. Joughin (2011), Seasonal speedup of the Greenland Ice Sheet linked to routing of surface water, *Earth and Planetary Science Letters*, *302*(3), 423-428, https://doi.org/10.1016/j.epsl.2010.12.037.

Pope, A., T. A. Scambos, M. Moussavi, M. Tedesco, M. Willis, D. Shean, and S. Grigsby (2016), Estimating supraglacial lake depth in West Greenland using Landsat 8 and comparison with other multispectral methods, *The Cryosphere*, *10*(1), 15-27, http://doi.org/10.5194/tc-10-15-2016.

Porter, D. F., K. J. Tinto, A. Boghosian, J. R. Cochran, R. E. Bell, S. S. Manizade, and J. G. Sonntag (2014), Bathymetric control of tidewater glacier mass loss in northwest Greenland, *Earth and Planetary Science Letters*, *401*, 40-46, https://doi.org/10.1016/j.epsl.2014.05.058.

Porter, D. F., K. J. Tinto, A. L. Boghosian, B. M. Csatho, R. E. Bell, and J. R. Cochran (2018), Identifying Spatial Variability in Greenland's Outlet Glacier Response to Ocean Heat, *Frontiers in Earth Science*, *6*(90), https://doi.org/10.3389/feart.2018.00090.

Pritchard, H. D., R. J. Arthern, D. G. Vaughan, and L. A. Edwards (2009), Extensive dynamic thinning on the margins of the Greenland and Antarctic ice sheets, *Nature*, *461*(7266), 971-975, https://doi.org/10.1038/nature08471.

Rignot, E., et al. (2021), Retreat of Humboldt Gletscher, North Greenland, Driven by Undercutting From a Warmer Ocean, *Geophysical Research Letters*, *48*(6), e2020GL091342, https://doi.org/10.1029/2020GL091342.

Rignot, E., and P. Kanagaratnam (2006), Changes in the Velocity Structure of the Greenland Ice Sheet, *Science*, *311*(5763), 986-990, https://doi.org/10.1126/science.1121381.

Rignot, E., M. Koppes, and I. Velicogna (2010), Rapid submarine melting of the calving faces of West Greenland glaciers, *Nature Geoscience*, *3*(3), 187-191, https://doi.org/10.1038/ngeo765.

Rolstad, C., T. Haug, and B. Denby (2009), Spatially integrated geodetic glacier mass balance and its uncertainty based on geostatistical analysis: application to the western Svartisen ice cap, Norway, *Journal of Glaciology*, *55*(192), 666-680, https://doi.org/10.3189/002214309789470950.

Saito, J., S. Sugiyama, S. Tsutaki, and T. Sawagaki (2016), Surface elevation change on ice caps in the Qaanaaq region, northwestern Greenland, *Polar Science*, *10*(3), 239-248, https://doi.org/10.1016/j.polar.2016.05.002.

Sakakibara, D., and S. Sugiyama (2018), Ice front and flow speed variations of marine-terminating outlet glaciers along the coast of Prudhoe Land, northwestern Greenland, *Journal of glaciology*, *64*(244), 300-310, https://doi.org/10.1017/jog.2018.20.

Sakakibara, D., and S. Sugiyama (2020), Seasonal ice-speed variations in 10 marine-terminating outlet glaciers along the coast of Prudhoe Land, northwestern Greenland, *Journal of Glaciology*, *66*(255), 25-34, http://doi.org/10.1017/jog.2019.81.

Sakov, P., F. Counillon, L. Bertino, K. A. Lisæter, P. R. Oke, and A. Korablev (2012), TOPAZ4: an ocean-sea ice data assimilation system for the North Atlantic and Arctic, *Ocean Sci.*, *8*(4), 633-656, https://doi.org/10.5194/os-8-633-2012.

Sasgen, I., B. Wouters, A. S. Gardner, M. D. King, M. Tedesco, F. W. Landerer, C. Dahle, H. Save, and X. Fettweis (2020), Return to rapid ice loss in Greenland and record loss in 2019 detected by the GRACE-FO satellites, *Communications Earth & Environment*, *1*(1), 8, http://doi.org/10.1038/s43247-020-0010-1.

Schwanghart, W., and D. Scherler (2014), Short Communication: TopoToolbox 2 – MATLAB-based software for topographic analysis and modeling in Earth surface sciences, *Earth Surf. Dynam.*, *2*(1), 1-7, http://doi.org/10.5194/esurf-2-1-2014.

Selmes, N., T. Murray, and T. James (2011), Fast draining lakes on the Greenland Ice Sheet, *Geophysical Research Letters*, *38*(15).

Sergienko, O. V. (2013), Glaciological twins: basally controlled subglacial and supraglacial lakes, *Journal of Glaciology*, *59*(213), 3-8, http://doi.org/10.3189/2013JoG12J040.

Shepherd, A., et al. (2020), Mass balance of the Greenland Ice Sheet from 1992 to 2018,

Nature, *579*(7798), 233-239, https://doi.org/10.1038/s41586-019-1855-2.

Slater, T., et al. (2021), Increased variability in Greenland Ice Sheet runoff from satellite observations, *Nature Communications*, *12*(1), 6069, http://doi.org/10.1038/s41467-021-26229-4.

Smith, B., et al. (2020), Pervasive ice sheet mass loss reflects competing ocean and atmosphere processes, *Science*, *368*(6496), 1239-1242, https://doi.org/10.1126/science.aaz5845.

Solgaard, A. M., S. B. Simonsen, A. Grinsted, R. Mottram, N. B. Karlsson, K. Hansen, A. Kusk, and L. S. Sørensen (2020), Hagen Bræ: A Surging Glacier in North Greenland—35 Years of Observations, *Geophysical Research Letters*, *47*(6), e2019GL085802, https://doi.org/10.1029/2019gl085802.

Stehman, S. V. (1997), Selecting and interpreting measures of thematic classification accuracy, *Remote Sensing of Environment*, *62*(1), 77-89, https://doi.org/10.1016/S0034-4257(97)00083-7.

Stevens, L. A., M. D. Behn, J. J. McGuire, S. B. Das, I. Joughin, T. Herring, D. E. Shean, and M. A. King (2015), Greenland supraglacial lake drainages triggered by hydrologically induced basal slip, *Nature*, *522*(7554), 73.

Straneo, F., and C. Cenedese (2015), The Dynamics of Greenland's Glacial Fjords and Their Role in Climate, *Annual Review of Marine Science*, *7*(1), 89-112, http://doi.org/10.1146/annurev-marine-010213-135133.

Straneo, F., G. S. Hamilton, D. A. Sutherland, L. A. Stearns, F. Davidson, M. O. Hammill, G. B. Stenson, and A. Rosing-Asvid (2010), Rapid circulation of warm subtropical waters in a major glacial fjord in East Greenland, *Nature Geoscience*, *3*(3), 182-186, https://doi.org/10.1038/ngeo764.

Straneo, F., and P. Heimbach (2013), North Atlantic warming and the retreat of Greenland's outlet glaciers, *Nature*, *504*(7478), 36-43, https://doi.org/10.1038/nature12854.

Straneo, F., P. Heimbach, O. Sergienko, G. Hamilton, G. Catania, S. Griffies, R. Hallberg, A. Jenkins, I. Joughin, and R. Motyka (2013), Challenges to understanding the dynamic response of Greenland's marine terminating glaciers to oceanic and atmospheric forcing, *Bulletin of the American Meteorological Society*, *94*(8), 1131-1144.

Sugiyama, S., D. Sakakibara, S. Matsuno, S. Yamaguchi, S. Matoba, and T. Aoki (2014), Initial field observations on Qaanaaq ice cap, northwestern Greenland, *Annals of Glaciology*, *55*(66), 25-33, http://doi.org/10.3189/2014AoG66A102.

Sugiyama, S., D. Sakakibara, S. Tsutaki, M. Maruyama, and T. Sawagaki (2015), Glacier dynamics near the calving front of Bowdoin Glacier, northwestern Greenland, *Journal of glaciology*, *61*(226), 223-232, https://doi.org/10.3189/2015JoG14J127.

Sundal, A. V., A. Shepherd, P. Nienow, E. Hanna, S. Palmer, and P. Huybrechts (2009), Evolution of supra-glacial lakes across the Greenland Ice Sheet, *Remote Sensing of Environment*, *113*(10), 2164-2171, https://doi.org/10.1016/j.rse.2009.05.018.

Sundal, A. V., A. Shepherd, P. Nienow, E. Hanna, S. Palmer, and P. Huybrechts (2011), Melt-induced speed-up of Greenland ice sheet offset by efficient subglacial drainage, *Nature*, *469*(7331), 521-524, http://doi.org/10.1038/nature09740.

Tedesco, M., and X. Fettweis (2020), Unprecedented atmospheric conditions (1948–2019) drive the 2019 exceptional melting season over the Greenland ice sheet, *The Cryosphere*, *14*(4), 1209-1223, http://doi.org/10.5194/tc-14-1209-2020.

Tedesco, M., M. Lüthje, K. Steffen, N. Steiner, X. Fettweis, I. Willis, N. Bayou, and A. Banwell (2012), Measurement and modeling of ablation of the bottom of supraglacial lakes in western Greenland, *Geophysical Research Letters*, *39*(2), https://doi.org/10.1029/2011GL049882.

Teluguntla, P., P. S. Thenkabail, A. Oliphant, J. Xiong, M. K. Gumma, R. G. Congalton, K. Yadav, and A. Huete (2018), A 30-m landsat-derived cropland extent product of Australia and China using random forest machine learning algorithm on Google Earth Engine cloud computing platform, *ISPRS Journal of Photogrammetry and Remote Sensing*, *144*, 325-340, https://doi.org/10.1016/j.isprsjprs.2018.07.017.

Thomas, R. H., W. Abdalati, E. Frederick, W. B. Krabill, S. Manizade, and K. Steffen (2003), Investigation of surface melting and dynamic thinning on Jakobshavn Isbræ, Greenland, *Journal of Glaciology*, *49*(165), 231-239, http://doi.org/10.3189/172756503781830764.

Toutin, T. (2002), Three-dimensional topographic mapping with ASTER stereo data in rugged topography, *IEEE Transactions on Geoscience and Remote Sensing*, *40*(10), 2241-2247, https://doi.org/10.1109/TGRS.2002.802878.

Tsutaki, S., S. Sugiyama, D. Sakakibara, and T. Sawagaki (2016), Surface elevation changes during 2007–13 on Bowdoin and Tugto Glaciers, northwestern Greenland, *Journal of glaciology*, *62*(236), 1083-1092, https://doi.org/10.1017/jog.2016.106.

Tuckett, P. A., J. C. Ely, A. J. Sole, J. M. Lea, S. J. Livingstone, J. M. Jones, and J. M. van Wessem (2021), Automated mapping of the seasonal evolution of surface meltwater and its links to climate on the Amery Ice Shelf, Antarctica, *The Cryosphere*, *15*(12), 5785-5804, http://doi.org/10.5194/tc-15-5785-2021.

Turton, J. V., P. Hochreuther, N. Reimann, and M. T. Blau (2021), The distribution and evolution of supraglacial lakes on 79° N Glacier (north-eastern Greenland) and interannual climatic controls, *The Cryosphere*, *15*(8), 3877-3896, http://doi.org/10.5194/tc-15-3877-2021.

van den Broeke, M., J. Bamber, J. Ettema, E. Rignot, E. Schrama, W. J. van de Berg, E. van Meijgaard, I. Velicogna, and B. Wouters (2009), Partitioning Recent Greenland Mass Loss, *Science*, *326*(5955), 984-986, https://doi.org/10.1126/science.1178176.

van den Broeke, M. R., E. M. Enderlin, I. M. Howat, P. Kuipers Munneke, B. P. Y. Noël, W. J. van de Berg, E. van Meijgaard, and B. Wouters (2016), On the recent contribution of the Greenland ice sheet to sea level change, *The Cryosphere*, *10*(5), 1933-1946, https://doi.org/10.5194/tc-10-1933-2016.

van der Veen, C. J. (2002), Calving glaciers, *Progress in Physical Geography*, *26*(1), 96-122, http://doi.org/10.1191/0309133302pp327ra.

Van Der Veen, C. J. (1996), Tidewater calving, *Journal of Glaciology*, *42*(141), 375-385, http://doi.org/10.3189/S0022143000004226.

Veitch, S. A., and M. Nettles (2012), Spatial and temporal variations in Greenland glacial-earthquake activity, 1993–2010, *Journal of Geophysical Research: Earth Surface*,

117(F4), https://doi.org/10.1029/2012JF002412.

von Albedyll, L., H. Machguth, S. U. Nussbaumer, and M. Zemp (2018), Elevation changes of the Holm Land Ice Cap, northeast Greenland, from 1978 to 2012–2015, derived from high-resolution digital elevation models, *Arctic, Antarctic, and Alpine Research*, *50*(1), e1523638, https://doi.org/10.1080/15230430.2018.1523638.

Walsh, K. M., I. M. Howat, Y. Ahn, and E. M. Enderlin (2012), Changes in the marine-terminating glaciers of central east Greenland, 2000–2010, *The Cryosphere*, *6*(1), 211-220, https://doi.org/10.5194/tc-6-211-2012.

Wang, Y., S. Sugiyama, and A. A. Bjørk (2021), Surface Elevation Change of Glaciers Along the Coast of Prudhoe Land, Northwestern Greenland From 1985 to 2018, *Journal of Geophysical Research: Earth Surface*, *126*(11), e2020JF006038, https://doi.org/10.1029/2020JF006038.

Watson, C. S., N. J. White, J. A. Church, M. A. King, R. J. Burgette, and B. Legresy (2015), Unabated global mean sea-level rise over the satellite altimeter era, *Nature Climate Change*, *5*(6), 565-568, https://doi.org/10.1038/nclimate2635.

Williamson, A. G., A. F. Banwell, I. C. Willis, and N. S. Arnold (2018a), Dual-satellite (Sentinel-2 and Landsat 8) remote sensing of supraglacial lakes in Greenland, *Cryosphere*, *12*(9).

Williamson, A. G., I. C. Willis, N. S. Arnold, and A. F. Banwell (2018b), Controls on rapid supraglacial lake drainage in West Greenland: an Exploratory Data Analysis approach, *Journal of Glaciology*, *64*(244), 208-226, http://doi.org/10.1017/jog.2018.8.

Willis, J. K., D. Carroll, I. Fenty, G. Kohli, A. Khazendar, M. Rutherford, N. Trenholm, and M. Morlighem (2018), Ocean-ice interactions in Inglefield Gulf: Early results from NASA's Oceans Melting Greenland mission, *Oceanography*, *31*(2), 100-108, https://doi.org/10.5670/oceanog.2018.211.

Wood, M., et al. (2021), Ocean forcing drives glacier retreat in Greenland, *Science Advances*, *7*(1), eaba7282, http://doi.org/10.1126/sciadv.aba7282.

Wood, M., E. Rignot, I. Fenty, D. Menemenlis, R. Millan, M. Morlighem, J. Mouginot, and H. Seroussi (2018), Ocean-Induced Melt Triggers Glacier Retreat in Northwest Greenland, *Geophysical Research Letters*, *45*(16), 8334-8342, https://doi.org/10.1029/2018GL078024.

Woul, M. D., and R. Hock (2005), Static mass-balance sensitivity of Arctic glaciers and ice caps using a degree-day approach, *Annals of Glaciology*, *42*, 217-224, http://doi.org/10.3189/172756405781813096.

Yang, K., and L. C. Smith (2013), Supraglacial Streams on the Greenland Ice Sheet Delineated From Combined Spectral–Shape Information in High-Resolution Satellite Imagery, *IEEE Geoscience and Remote Sensing Letters*, *10*(4), 801-805, http://doi.org/10.1109/LGRS.2012.2224316.

Zwally, H. J., W. Abdalati, T. Herring, K. Larson, J. Saba, and K. Steffen (2002), Surface Melt-Induced Acceleration of Greenland Ice-Sheet Flow, *Science*, *297*(5579), 218-222, http://doi.org/10.1126/science.1072708.

Acknowledgements

First and foremost, I would like to thank my supervisor, Prof. Shin Sugiyama, also the chair of my doctoral degree supervisory committee. His continual guidance, encouragement, and support throughout my time at Hokkaido University have been invaluable and I feel privileged to have had the opportunity to study and research with him. Not only in the research, but he also gave me a lot of help and care in daily life, which made me feel very warm in a foreign country.

I would also like to thank to the committee members of my PhD thesis: Prof. Ralf Greve, Prof. Yoshinori Iizuka, Prof. Shigeru Aoki, and Prof. Masato Furuya, for their insightful comments and encouragement to my study.

My special thanks to Dr. Anders Bjørk, Department of Geosciences and Natural Resource Management, University of Copenhagen. Thank you for sharing me the valuable historical data and constructive comments on my research. I would also like to express my gratitude to Dr. Shun Tsutaki and Dr. Daiki Sakakibara. It was your initial work that inspired my current research.

Thank you Dr. Naoya Kanna, Dr. Takuto Ando, and Ms. Izumi Asaji, for caring about me a lot in the field campaign in northwestern Greenland in 2019. Although we were very tired, we had a great and happy time there. Meanwhile, I want to express my thanks to Mr. Shuntaro Hata and Mr. Ken Kondo, I enjoyed the time we spent together discussing our studies and life. Also, I want to say thank you to all the members of the Glacier and Ice Sheet Research Group in the Institute of Low Temperature Science, Hokkaido University for their kind support and pleasant atmosphere during my study, you make me feel at home. I am grateful to all my friends, we share our happiness and sadness, and having you all make me feel not alone.

Finally, I would like to thank my parents, for their endless and unwavering patience, support, and encouragement.

This research was funded by the Japanese Ministry of Education, Culture, Sports, Science and Technology (MEXT) through the projects ArCS (Arctic Challenge for

Sustainability) (JPMXD1300000000) and ArCS II (JPMXD1420318865). And the study for me study in Japan was funded by Japanese Government (MEXT) Scholarship.